Electronic Thesis and Dissertation Repository

10-15-2021 10:00 AM

Phase imaging for reducing macrovascular signal contributions in high-resolution fMRI

Olivia W. Stanley, *The University of Western Ontario*

Supervisor: Menon, Ravi S, *The University of Western Ontario*
A thesis submitted in partial fulfillment of the requirements for the Doctor of Philosophy degree in Medical Biophysics
© Olivia W. Stanley 2021

Abstract

High resolution functional MRI allows for the investigation of neural activity within the cortical sheet. One consideration in high resolution fMRI is the choice of which sequence to use during imaging, as all methods come with sensitivity and specificity tradeoffs. The most used fMRI sequence is gradient-echo echo planar imaging (GE-EPI) which has the highest sensitivity but is not specific to microvasculature. GE-EPI results in a signal with pial vessel bias which increases complexity of performing studies targeted at structures within the cortex. This work seeks to explore the use of MRI phase signal as a macrovascular filter to correct this bias.

First, an in-house phase combination method was designed and tested on the 7T MRI system. This method, the fitted SVD method, uses a low-resolution singular value decomposition and fitting to a polynomial basis to provide computationally efficient, phase sensitive, coil combination that is insensitive to motion. Second, a direct comparison of GE-EPI, GE-EPI with phase regression (GE-EPI-PR), and spin echo EPI (SE-EPI) was performed in humans completing a visual task. The GE-EPI-PR activation showed higher spatial similarity with SE-EPI than GE-EPI across the cortical surface. GE-EPI-PR produced a similar laminar profile to SE-EPI while maintaining a higher contrast-to-noise ratio across layers, making it a useful method in low SNR studies such as high-resolution fMRI. The final study extended this work to a resting state macaque experiment. Macaques are a common model for laminar fMRI as they allow for simultaneous imaging and electrophysiology. We hypothesized that phase regression could improve spatial specificity of the resting state data. Further analysis showed the phase data contained both system and respiratory artifacts which prevented the technique performing as expected under two physiological cleaning strategies. Future work will have to examine on-scanner physiology correction to obtain a phase timeseries without artifacts to allow for the phase regression technique to be used in macaques.

This work demonstrates that phase regression reduces signal contributions from pial vessels and will improve specificity in human layer fMRI studies. This method can be completed easily with complex fMRI data which can be created using our fitted SVD method.

Summary for Lay Audience

Functional MRI investigates brain function using the changing concentration of blood oxygen in the brain. This process has several pitfalls, one of which is inaccurate signals in large vessels far from the activating region caused by the pooling together of changing blood oxygen signals from many small vessels. One possible solution to these spurious signals is using a secondary imaging contrast from the MRI machine, the phase, to estimate these pooled signals and remove them. This technique has previously shown success in resting state and task based human studies. This thesis extends upon this work by investigating this technique at high resolution.

The first chapter of this thesis describes a method for the combination of phase data from a multi-coil radio-frequency array. High resolution fMRI requires a multi-coil radio-frequency array to acquire a high signal-to-noise image. These arrays require additional steps to create a high-quality phase image. This method estimates and corrects offsets for these arrays using data routinely acquired throughout the imaging session.

The second chapter of this thesis goes on to investigate phase regression at high resolution in a visual task. This chapter compares images collected with and without phase regression as well as a control image technique sensitive to small vessels. The findings show that fMRI with phase regression resulted in less pooled signal in the observed activation while retaining a higher contrast-to-noise ratio than the control condition.

The third chapter of this thesis details the study of phase regression in macaques during resting state. Macaque fMRI also contains pooled signal and is a common model for high resolution imaging studies. Phase regression did not perform well due to the presence of system and breathing noise in the acquired images. Several recommendations pertaining to quality determination are discussed to improve this experiment and phase regression studies generally.

Overall, this thesis extends the use of phase regression to high-resolution human fMRI and designed a multi-coil combination method for this application. A pilot of this procedure in animals was completed but requires further correction for phase artifacts, like system and breathing noise.

Keywords

Functional MRI, High resolution fMRI, Gradient echo, Spin Echo, Phase, Coil Combination, Coil Sensitivities, Phase regression, Macrovasculature, Singular Value Decomposition

Abbreviations

AFI	Actual Flip-angle Imaging
ATP	Adenosine Triphosphate
B_0	Main Magnetic Field
B_1^-	RF Receive Magnetic Field
B_1^+	RF Transmit Magnetic Field
BCC	Block Coil Compression
BIDS	Brain Imaging Data Structure
BOLD	Blood Oxygen Level Dependent
bSSFP	Balanced Steady State Free Procession
BW	Bandwidth
CompCor	Component Based Noise Correction
COMPOSER	Combining Phase Images from Array Coils Using a Short Echo Time Reference Scan
CBF	Cerebral Blood Flow
CBV	Cerebral Blood Volume
CNR	Contrast to Noise Ratio
DORK	Dynamic Off-Resonance in k-Space
EPI	Echo Planar Imaging
ESPIRiT	iTerative Self-consistent Parallel Imaging Reconstruction Using Eigenvector Maps
FA	Flip Angle

fMRI	Functional Magnetic Resonance Imaging
FWHM	Full Width Half Maximum
G	Gradient Magnetic Field
GE	Gradient Echo
GE-EPI	Gradient-Echo Echo Planar Imaging
GE-EPI-PR	Gradient-Echo Echo Planar Imaging with Phase Regression
GRE	Gradient Recalled Echo
GLM	General Linear Model
GRAPPA	Generalized Auto Calibrating Partial Parallel Acquisition
GRASE	Gradient and Spin-Echo
HRF	Hemodynamic Response Function
ICA	Independent Component Analysis
M_0	Net Magnetization
MP2RAGE	Magnetization Prepared 2 Rapid Acquisition Gradient Echoes
MRI	Magnetic Resonance Imaging
NMR	Nuclear Magnetic Resonance
ODR	Orthogonal Distance Regression
PET	Positron Emission Tomography
PR	Phase Regression
PSF	Point Spread Function
pTx	Parallel Transmit
QSM	Quantitative Susceptibility Mapping
fQSM	Functional Quantitative Susceptibility Mapping
R_2^*	Apparent Transverse Relaxation Rate

RETROICOR	Retrospective Image-space Correction
RF	Radio Frequency
Rx	Receive
SAR	Specific Absorption Rate
SE	Spin Echo
SE-EPI	Spin-Echo Echo Planar Imaging
SENSE	Sensitivity Encoding
SNR	Signal to Noise Ratio
T	Tesla
T_1	Longitudinal Relaxation Constant
T_2	Transverse Relaxation Constant
T_2^*	Apparent Transverse Relaxation Constant
TE	Echo Time
TI	Inversion Time
TR	Repetition Time
Tx	Transmit
SVD	Singular Value Decomposition
V1	Primary Visual Cortex
V2	Secondary Visual Cortex
VASO	Vascular Space Occupancy
VBC	Virtual Body Coil
VRC	Virtual Reference Coil

Co-Authorship Statement

The following thesis is presented in Integrated Article format and contains two manuscripts that have been accepted in scientific journals and one unpublished manuscript.

Chapter 2: Stanley OW, Menon RS, Klassen LM. Receiver phase alignment using fitted SVD derived sensitivities from routine prescans. PLoS One. 2021; 16(8): e0256700. doi:10.1371/journal.pone.0256700

My contribution to this work included study design, participant recruitment, data acquisition, analysis, interpretations, drafting, and revising the manuscript. Ravi Menon provided supervision and support on analysis, interpretations, and manuscript revision. Martyn Klassen conceptualized the study and provided the initial codebase for the fitted SVD method. He also provided guidance and support on study design, data acquisition, analysis, interpretations, and manuscript revision.

Chapter 3: Stanley OW, Kuurstra AB, Klassen LM, Menon RS, Gati JS. Effects of phase regression on high-resolution functional MRI of the primary visual cortex. NeuroImage. 2021;227: 117631. doi:10.1016/j.neuroimage.2020.117631

My contribution to this work included study design, participant recruitment, data acquisition, analysis, interpretations, drafting, and revising the manuscript. Alan Kuurstra provided software for the multi-echo data analysis as well as manuscript revisions. Martyn Klassen provided support on analysis, interpretations, and manuscript revision. Ravi Menon provided supervision and support on analysis, interpretations, and manuscript revision. Joseph Gati conceptualized the study and provided guidance and support on data acquisition, analysis, interpretations, and manuscript revision.

Chapter 4: Stanley OW, Ngo GN, and Menon RS. Phase Regression in Macaques: An investigation of physiological confounds. In preparation.

My contribution to this work included study design, MRI protocol optimization, data acquisition, analysis, interpretations, drafting, and revising the manuscript. Geoffrey Ngo provided support in performing the resting state analysis as well as providing manuscript

revisions. Ravi Menon conceptualized the study and provided supervision and support on analysis, interpretations, and manuscript revision.

Acknowledgments

I would like to begin by thanking my supervisor, Ravi Menon for the opportunity to grow and learn as a scientist as well as give me access to resources and equipment I would never have had outside his laboratory. I would like to thank Joe Gati and Martyn Klassen for providing me with unending amounts of patience and feedback as I collaborated with them to complete this work. Without these three people this thesis would not have been possible. I would like to thank my committee members: Rhodri Cusack, Jörn Diedrichsen, Stefan Everling, and Andrew Pruszynski, for their support and advice throughout my degree. I would like to emphasize my gratitude towards Maria Drangova and Charlie McKenzie for the endless administrative support and advice throughout my degree.

I would like to thank Trevor Szekeres for his help with MRI acquisition. Thanks also to Whitney Froese and Cheryl Vander Tuin for the animal handling assistance. To the entire staff of the Centre for Functional and Metabolic Mapping, thank you for your support, your baked goods, your stories, and your lessons. Be it learning how to scan on the 7T, build a phantom, or solve a hard problem you were always available. To the students of CFMM and the larger Robarts community, thank you for your friendship and support through good times and bad.

I would like to thank my families, of which I am blessed with many. To my parents, Sonya and Cliff and my siblings Nate and George, thank you for turning me into the person I am today. To my partner Scott, I have nothing to say but thank you, let's go live our lives together! To my "Ontario family", Lynda and Kris, thank you for welcoming me into your lives, I promise more cookies and bread to come.

I would like to dedicate this thesis to Larry Fortune. I didn't know I needed another dad till you showed up, turns out there are always more chairs at the table. I'm glad for all the time we got to spend together, and I am eternally grateful you and Lynda raised such an amazing son.

Table of Contents

List of Tables

List of Figures

List of Appendices

Chapter 1

1 Introduction

1.1 Background for high resolution study of the human brain

Studying the healthy brain allows us to better understand human behaviour, development, and physiology. This progresses our understanding of psychology, neuroscience, and medicine. In addition to advancing science, understanding the neurophysiology of a healthy human allows us to better understand diseased brains as we can compare them to these healthy studies.

One ongoing area of research in healthy humans aims to improve non-invasive imaging of human brain function. Prior to the invention of positron emission tomography (PET), human studies of neuroscience were limited to studies of external behaviour, post-mortem examination, and presurgical patients [1]. Anatomical data was used to develop hypotheses of brain function and it was understood that blood flow and brain function were linked through surgical observation [1]. Development of PET further improved imaging of brain function, though it required the use of exogenous radioactive tracers. Finally, in the early 1990s, the breakthrough development of functional MRI (fMRI) provided an endogenous contrast sensitive to changes in blood oxygen concentration that changed the landscape of functional imaging of the brain [2].

Functional MRI provided a method to image healthy humans non-invasively, repeatedly, and with no radiation exposure or other long-term side effects. This allowed for detailed investigations into novel experimental paradigms involving complex tasks, as well as repeated experiments important for studying long processes such as the development of motor skills [3]. Many physics developments in fMRI have led to improved resolutions, acquisition times and image quality since its inception [4–6]. Functional MRI has also been supported by parallel development of higher field magnets which drive

improvements in resolution and image quality [7]. In combination, these developments have allowed for state-of-the-art non-invasive imaging of the human brain.

This higher resolution and improved SNR enable imaging of cortical layers and columns, structures that have been shown to provide information as to whether a signal is an input or an output as well as revealing how the cortex is internally organized [8]. Studying inputs and outputs of cortex gives us knowledge of information flow within the brain and this can be applied to investigate hypotheses developed in invasive electrophysiology work where the condition could be affected by the experiment [9] as well as study how information transfer is different in disease models [10]. This thesis contributes to a constantly advancing field of high-resolution fMRI by (1) outlining a method that can be used for the acquisition of high-resolution EPI phase data, (2) examining the effects phase regression has on a task based BOLD response at high resolution, and (3) piloting phase regression in a macaque model, a common target for high resolution fMRI work [11,12].

1.2 The structure of the human cortex

The mammalian brain is organized into three major structures: the cerebrum, the brainstem, and the cerebellum. The cerebrum is primarily responsible for processing many unique human cognitive abilities and is made up of two tissue types: white matter, which primarily contains axons connecting neural bodies to their synapses; and grey matter, where neurons reside, and the cognitive processes of the cerebrum occur [13]. Grey matter resides on the surface of the white matter and displays laminar structure with neuronal and vascular layers that run parallel to the grey matter surface [14]. In some areas of the cortex, grey matter also exhibits functionally organizing columns that show tuning to different stimuli such as visual stimulus orientation [15].

The laminar structure of the cortex was determined through examination of the different neuronal and glial cell types as well as their physical connectivity as a function of cortical depth. The majority of cortical areas exhibit a common six-layer structure, and the input and output structure has been simplified into the canonical microcircuit, however

this may not be consistent across the whole brain [16]. In the canonical microcircuit the inputs to a cortical area terminate in layer IV, whereas the cortical outputs originate in layers I-III, and layers V-VI project neurons into subcortical structures. For example, the laminar structure of the primary visual cortex is displayed in Figure 1.1.
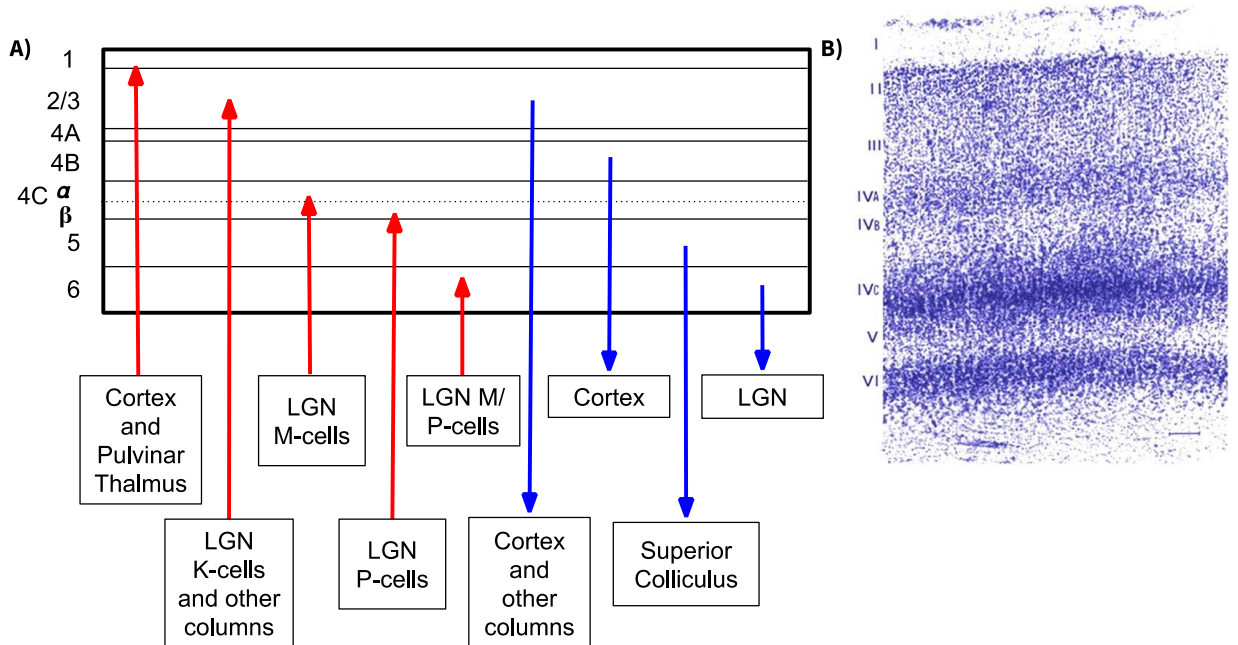
Figure 1.1: Laminar Structure of Visual Cortex. a) Review of the inputs and outputs of the laminar structure of the primary visual cortex. LGN is the lateral geniculate nucleus which contains parvocellular (P-cells), magnocellular (M-cells), koniocellular (K-cells) cells. These cells process information from rods, cones, and short-wavelength cones respectively. b) Nissl stain of the primary visual cortex to show different neuronal patterning as a function of layer, image sourced from Webvision: The Organization of the Retina and Visual System [17] © Webvision and reproduced under the CC BY-NC 4.0 license.

In addition to cortical layers, some brain areas, such as the visual cortex, display task specific cortical columns [15]. These functional projections outline areas specialized to a certain kind of input. For example, the primary visual cortex (V1) displays columnar sensitivity to orientation and ocular dominance [18], and the secondary visual cortex (V2) displays columnar sensitivity to colour [19]. These cortical substructures provide a way of examining the processing within the visual cortex to determine sources of communication as well as the content of the communicated information. For example, the distribution of

ocular dominance across layers provides clues as to how information from both eyes is merged into a single representation of the visual field [15].

This complex neuronal structure is supported by an extensive vascular network that delivers oxygen and other materials to the brain. At any given time 20% of the total blood supply is in the brain [20]. The vascular organization of the cortex begins with the major arteries of the brain which feed pial arteries running along the surface of the cortex. Pial arteries are made up of smooth muscle cells and endothelium. These pial arteries subdivide and feed penetrating arterioles which penetrate the cortical sheet perpendicular to the pial vessels. Penetrating arterioles feed the capillary network surrounding and directly supply the cortical neurons with oxygenated blood. Capillaries, 5-10 µm in diameter, lack smooth muscle cells, and this allows for gas and ion exchange through their endothelium. These capillaries drain into ascending venules (80-170 μm, no smooth muscle) and pial draining veins (>280 µm, smooth muscle present) and out to the sinuses of the brain [21]. The vessels with the highest importance to fMRI are the pial veins, penetrating veins, and capillaries which can be seen in Figure 1.2. This is because these vessels undergo changes in blood oxygenation in response to neural activity and are the source of the blood oxygenation level contrast in the brain.
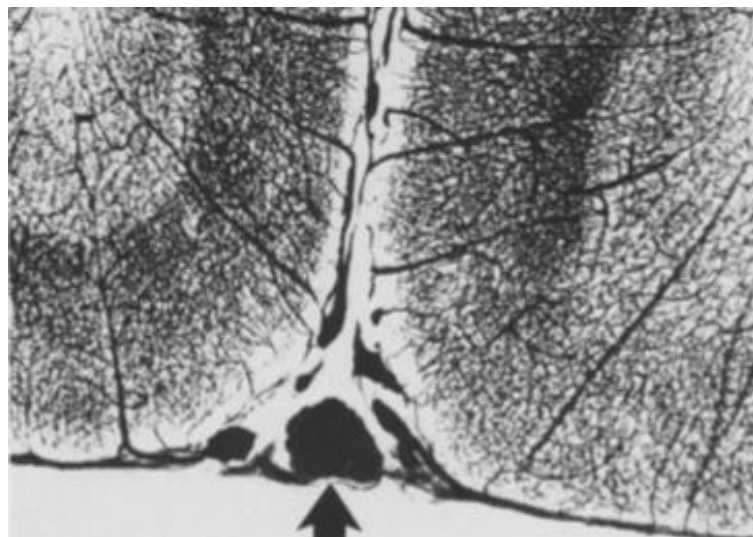
Figure 1.2: Example cortical vessel distribution of the visual cortex. Arrow points to the calcarine sulcus. Image sourced from Cortical Blood Vessels of the Human Brain, Duvernoy et al. [21] © Wiley and reproduced with permission of the copyright holder.

1.3   MRI Physics

The MRI system relies on three magnetic fields: B_0, the main magnetic field; $B_1^{+/-}$, the excitatory and receive fields from an RF coil; and G, the gradient fields used to form an image. These three fields work in tandem to produce an image, but the fundamentals of nuclear magnetic resonance can be applied using only B_0 and $B_1^{+/-}$. These two fields allow for information about the properties of matter being imaged to be acquired and when paired with gradients can be used to produce an image [22].

1.3.1   Nuclear magnetic resonance

Spin is a fundamental property of matter that takes values of ½ integer multiples. A nucleus' spin number is based on the number of charged particles in it. Spin gives rise to a nucleus' angular momentum and as a result all nuclei with a nonzero spin have a magnetic moment. This follows the following equation:

$$\vec{\mu} = \gamma \vec{J}$$
(1.3.1)

where $\vec{\mu}$ is the magnetic moment, $\vec{J}$ is the angular momentum and γ is the gyromagnetic ratio which varies depending on the nucleus. When a nucleus with a non-zero spin is placed in a magnetic field, its magnetic moment begins to precess parallel (low energy state) or anti-parallel (high energy state) to that field. Multiple nuclei placed in the field have their magnetic moments sum to form a net magnetization which precesses according to the Bloch equation:

$$\frac{d\vec{M}}{dt} = \gamma \vec{M} \times \vec{B}$$
(1.3.2)

where $\vec{M}$ is the net magnetization of the nuclei, and $\vec{B}$ is the applied magnetic field. The frequency of this precession, ω, is determined by that nucleus' gyromagnetic ratio.

$$\omega = \gamma B$$
(1.3.3)

When many precessing nuclei are considered across a whole system there is a measurable difference in the number of nuclei in the higher versus lower energy state as determined by the Boltzmann distribution shown below:

$$\frac{\Delta N}{N_0} = \frac{\hbar \gamma B_0}{2kT} \tag{1.3.4}$$

where ΔN is the number of excess nuclei in the low energy state, N_0 is the number of nuclei in the system, $\hbar$ is the reduced Plank's constant, B_0 is the strength of the magnetic field of the main magnet, k is Boltzmann's constant, and T is the temperature of the system. This fraction of excess nuclei is small, for example at 7T water has a $\frac{\Delta N}{N_0} = 2.3x10^{-5}$. These excess nuclei will lead to a net magnetization according to Curie's law (shown here for a spin ½ system).

$$M_0 = N_0 \frac{\hbar^2 \gamma^2 B_0}{4kT} \tag{1.3.5}$$

At equilibrium, the magnetization will point in the direction of the main magnetic field, as depicted by $\vec{M} = M_0 \hat{z}$. In order to obtain a signal from the system it is necessary to perturb it. To do this, excitatory coils are placed close to the system and an oscillatory current with frequency ω is applied, B_1^+. The frequency ω is in the radio frequency range. This current is applied in a perpendicular direction to B_0 which changes the direction of the overall field experienced by the net magnetization, $\vec{M}$, and causes it to precess around B_1^+. This current, commonly referred to as a pulse, is applied only briefly in order to move the magnetization to a desired offset angle from $\hat{z}$, called a flip angle. One example of this is a 90° pulse which moves the magnetization to a maximum in the x-y plane transverse to B_0. When the current is turned off, $\vec{M}$ relaxes back to its equilibrium direction of $\hat{z}$ and, as result of $\vec{M}$ moving in a magnetic field, produces an electromotive force detectable by receiver coils, B_1^-, in the form of a measurable current.

Three constants govern the relaxation of $\vec{M}$ back to equilibrium. These constants are longitudinal relaxation, reversible transverse relaxation, and irreversible transverse relaxation. The longitudinal relaxation constant, T_1, is the recovery of the longitudinal

component of the magnetization back to its equilibrium value along $\hat{z}$ and is the longest of the three constants. This relaxation is caused by the interaction of the precessing spins and their surrounding lattice and cannot be reversed with RF pulses. The reversible transverse relaxation constant, T_2', is caused by static magnetic field inhomogeneities and represents the amount of $\hat{x}$-$\hat{y}$ dephasing that can be reversed with 180° radio frequency refocusing pulses. The reversal occurs due to the rotation of the spins around the $\hat{x}$-$\hat{y}$ plane causing them to rephase together to a maximum signal, called an echo. The irreversible transverse relaxation constant, T_2, is due to spin-spin interactions causing irreversible dephasing in the $\hat{x}$-$\hat{y}$ plane. Together T_2 and T_2' combine to become T_2^*, the apparent transverse relaxation constant, which is the dominant constant for decay in accelerated imaging such as gradient-echo echo planar imaging (GE-EPI).

$$\frac{1}{T_2^*} = \frac{1}{T_2} + \frac{1}{T_2'} \tag{1.3.6}$$

These constants can be added to the Bloch equation as follows:

$$\frac{d\vec{M}}{dt} = \gamma \vec{M} \times \vec{B} - \frac{1}{T_1}(M_0 - M_z)\hat{z} - \frac{1}{T_2}\vec{M_\perp} \tag{1.3.7}$$

1.3.2   NMR and Phase

The net magnetization, $\vec{M}$, is often represented as a complex signal as it is attempting to represent the position of a vector on a plane (the transverse plane). This is shown in the following equation:

$$\vec{M} = M_x\hat{x} + iM_y\hat{y} = Me^{-i\varphi} \tag{1.3.8}$$

Here the phase, φ, represents the position on the transverse plane. Phase is a function of frequency shown below:

$$\varphi = \int dt \, \omega(t) \tag{1.3.9}$$

where ω is frequency of precession and t is time. The frequency of precession is affected by any local field inhomogeneities which can arise from the system itself or local characteristics of the tissue being imaged. In tissue, phase is affected by local field perturbing compounds such as iron [23] or myelin [24], in addition to factors that cause large changes in susceptibility, such as air tissue interfaces or effects caused by B_0 or B_1^+ inhomogeneities. These effects may lead to complications when measuring phase data, and therefore must be corrected prior to downstream analysis [25].

1.3.3   Magnetic Resonance Imaging

MR imaging cannot be completed using a homogeneous magnetic field and homogeneous RF coils alone because there is no spatial discrimination, only one spatially indistinct signal is generated for each excitation and no image is formed. The gradient field, G, allows for spatial encoding of the MR signal. To achieve this, gradient coils apply a selection of spatially varying magnetic fields $(\frac{d\overrightarrow{B_z}}{d\vec{x}}, \frac{d\overrightarrow{B_z}}{d\vec{y}}, \frac{d\overrightarrow{B_z}}{d\vec{z}})$ in combination with the RF excitation in order to perturb the frequency of the precessing magnetization as a function of space. This causes the spins to accrue phase as a function of their spatial position. This phase accrual takes the following form:

$$\phi(\vec{r}, t) = \gamma \int_0^t G(t')\vec{r}dt' \qquad (1.3.10)$$

where ϕ is the accrued phase, G is an example gradient, $\vec{r}$ is a spatial position and t is the moment in time the phase is calculated. Magnetic resonance imaging data is collected in k-space which is a spatial frequency space that is defined as follows:

$$k(t) = \frac{\gamma}{2\pi} \int_0^t G(t')dt' \qquad (1.3.11)$$

where $k(t)$ is the signal for a given spatial frequency at time t. This means the phase accrued from gradients can be represented as follows:

$$\phi(\vec{r}, t) = 2\pi k(t)\vec{r} \qquad (1.3.12)$$

8

This phase definition can be used to form the MRI signal equation:

$$s(k, t, T_2^*, T_1) = \int d\vec{r}\, \vec{M}(\vec{r}, t, T_2^*, T_1) e^{-i\phi(\vec{r}, t)t} = \int d\vec{r}\, \vec{M}(\vec{r}, t, T_2^*, T_1) e^{-i2\pi k(t)\vec{r}t} \quad (1.3.13)$$

where $\vec{M}$ is the magnetization at a location $\vec{r}$ which will include the history of the magnetization (aka the Bloch equation solution). Equation 1.3.13 is a Fourier transform of $\vec{M}$ and an inverse Fourier transform can be applied to produce an image of M. Using the gradients to manipulate the signal's position in k-space allows for acquisition of different spatial frequencies of the spin distribution. This eventually leads to collection of an entire spatial frequency and density map in k-space which can be transformed using the inverse Fourier transform to get an image in real-world space.

1.3.4   Echo formation

As nuclei relax, they can be manipulated through the application of RF excitatory signal or gradients to form a maximum magnetization called an echo. These echoes can be produced two ways, gradient-echo, and spin-echo. Gradient-echo applies a dephasing gradient after RF excitation and then applies a rephasing gradient to produce an echo in the middle of the signal acquisition. This echo reforms with a decay constant of T_2^* . Spin-echo uses an RF refocusing pulse between the dephasing and rephasing gradients which rotates $\vec{M}$ around the transverse plane and reverses the T_2' effects leaving a signal contribution that is weighted by T_2. A pictorial representation of these two echoes as played out in k-space is shown in Figure 1.3a and b. Echoes are usually designed to rephase the magnetization to a maximum at $k_x=0$, obtaining an entire line of k-space by acquiring data during both signal rephasing and dephasing. This linear gradient application during an echo is called frequency encoding and is used to fill the k_x direction of k-space. Phase encoding applies a gradient to prior to the application of the frequency encoding gradient in order to change the signal's position along k_y. By combining application of frequency encoding and phase encoding gradients a k-space image can be acquired one line at a time and then performing an inverse Fourier transform will result in an acquired image.
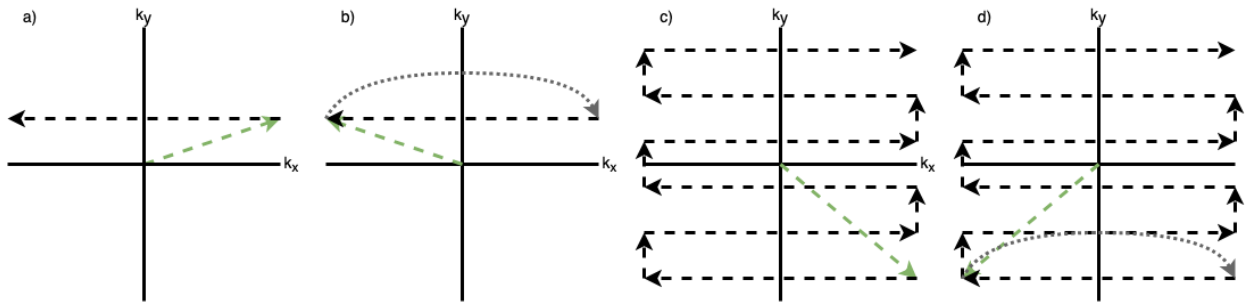
Figure 1.3: Example k-space trajectories. a) Gradient echo trajectory, a dephasing gradient is applied (green) to move to the start of a line and then a rephasing gradient is applied (black) with the echo centered on k_x=0. b) Spin echo trajectory, a dephasing gradient is applied (green) to move to the start of a line and then a refocusing pulse (grey) is applied to flip the magnetization to the opposite end of k-space as well as refocus T_2' dephasing, finally a rephasing gradient is applied (black) with the echo centered on k_x=0. c) Example GE-EPI trajectory, opposed to one line of acquisition per excitation many lines are acquired. After the initial phase encoding gradient (green), small gradient blips are applied in the y direction to allow for successive line collection from a single RF pulse, collecting the whole plane of k-space from a single excitation. d) Example SE-EPI trajectory where a refocusing echo is applied prior to image acquisition. Figures modified from [22] ©Wiley and reproduced with permission of the copyright holder.

1.3.5   Echo Planar Imaging

When completed a single k-space line at a time MR imaging is too slow to be used for the whole brain at the temporal resolution required for functional imaging as it takes on the order of minutes to form a single image. The most common imaging method for fMRI is the use of echo planar imaging (EPI), a pulse sequence that typically reads out an entire $\hat{x}$-$\hat{y}$ plane of k-space from a single excitation opposed to a single line per excitation (Figure 1.3c and d). This is accomplished by using a small phase encoding gradient pulse offset prior to the collection of each frequency encoding line in order to alter the spatial frequency sampled in the $\hat{y}$ direction for each line acquired. This method aims to center the echo on k_x=0 and k_y=0. This results in one direction of k-space being acquired much slower than the other direction which can result in blurring but lowers acquisition time to well under a second.

1.3.6   Multiple coil arrays

Further improvement in fMRI speed and signal-to-noise are achieved by use of the multi-element RF coil receive array. Radio frequency receive coil arrays benefit from higher SNR, compared to a single bird cage coil positioned around the head [6]. Each receive coil is typically a loop with a complex sensitivity profile that is proportional to loop radius [6]. Although these loops are not sensitive to the whole brain independently, they can be combined to form a high SNR image. This is especially important at ultra-high field (7T and above) where traditionally built bird cage coils show interference or dark spots in the images due to the shorter wavelength of the RF at higher frequencies [7]. Use of data acquired through an array of coils with a selection of coil sensitivity profiles allows for these wavelength effects to be reduced resulting in higher SNR and more uniform images.

Leveraging multiple coil data relies on knowing the complex coil sensitivity profiles to allow for combination without signal interference [26]. This combination is well defined for a magnitude image where sum-of-squares combination uses the magnitude of the signal itself as an estimate of the coil sensitivity [6]. This combination has the advantage of being simple and computationally efficient but can result in higher noise in regions with low coil sensitivity. Unlike magnitude combination, phase combination across multiple coil receivers requires special techniques. Sum-of-squares combination cannot be used as it results in an image with a phase of zero. Phase combination therefore requires an estimation of the coil sensitivity for each receive coil so it can be removed prior to a complex sum. These methods are reviewed in the introduction of Chapter 2.

One additional benefit of multiple coil arrays is they also allow for additional accelerations through parallel imaging or accelerated excitation. Two main forms of acceleration used in this thesis are generalized auto calibrating partial parallel acquisition (GRAPPA) [4] and multiband [5]. GRAPPA uses calibration lines collected over multiple coils to interpolate between under sampled high frequency lines of k-space. This is different than multiband which uses an multifrequency excitation pulse created to excite multiple slices and then separates this aliased signal using sensitivity encoding [27].

Multiband and GRAPPA are the two most common on the Siemens scanners in the Centre for Functional and Metabolic Mapping.

1.4 Blood Oxygen Level Dependent Contrast

Blood oxygenation level dependent contrast (BOLD) is an MRI measure of physiological vascular effect resulting from brain activity. Neuronal firing near an area of interest causes a metabolic cascade leading to vascular changes that result in a decrease in the deoxyhemoglobin concentration which, due to its difference in susceptibility from surrounding tissue, is ultimately detectable on an appropriately acquired MR image due to changes in relaxation times. Images with changing BOLD contrasts can be preprocessed and analyzed to answer questions discussed in section 1.1.

1.4.1 Metabolism and stimulus response

The physiological BOLD response is composed of the following components: stimulus to a brain area of interest, increases in neuronal firing, a metabolic response to neuronal firing, vasodilation causing an increase in cerebral blood volume (CBV), an increase in cerebral blood flow (CBF), and an increase in the concentration of oxygenated hemoglobin and decrease of deoxygenated hemoglobin [28]. When examining this cascade, it is important to understand the tremendous amount of energy that neural activity demands. Seventy four percent of the adenosine triphosphate (ATP) in the brain is used to create and recover from action potentials of neurons [20]. A constant and large supply of oxygen and glucose is required to allow for the aerobic production of ATP to sustain this energy demand. Cortical neural activity results in a cascade of vasoactive substances and electrical signals to the cortical vessels which triggers dilation in both the pial arteries and descending arterioles. This change was measured to be 33% in diameter [29]. This increase in CBV lowers vascular resistance and therefore there is an increase in CBF which results in a delivery of more oxygenated hemoglobin to the local area. There is significantly more oxyhemoglobin delivered to the area than is used by the active neurons [28]. These changes in the concentration of oxy-/deoxy-hemoglobin cause two effects detectable with MR imaging. First, a local shift in magnetic susceptibility that is detectable on MR images as

an increase in signal intensity to the local area [28]. Second, the T_2 of blood increases as the concentration of oxygenated hemoglobin increases causing additional signal brightening in T_2 or $T_2{}^{*}$ weighted images [30].

This BOLD response is characterized by three temporal phases: an initial dip, the main BOLD response, and a post stimulus undershoot. The initial dip is a smaller short onset negative response generally lasting 1-2 seconds thought to be due to the initial demand for oxygen that occurs before the CBF increases and compensates. The initial dip has been observed to have greater spatial specificity than the main BOLD response [20]. The main BOLD response is the inflow of oxygenated blood due to the changes in CBV and CBF described above and takes on the order of 6 seconds to reach its peak. After this response peaks there is a post-stimulus undershoot where the area slowly returns to baseline due to the slow recovery of CBV to baseline levels.

1.4.2   Frequency response to BOLD changes

Deoxyhemoglobin has a magnetic susceptibility difference of 0.18 ppm relative to surrounding tissue and oxyhemoglobin [31]. This susceptibility difference leads to a signal dephasing that is sensitive to the blood oxygenation fraction, or the BOLD effect. This BOLD signal change has two main effects on frequency: intravascular and extravascular [32]. The intravascular frequency is determined using this equation:

$$\omega_{iv} = 2\pi\gamma\Delta\chi B_0 Hct(1 - Y)\frac{3cos^2\theta - 1}{3} \qquad (1.4.1)$$

where γ is the gyromagnetic ratio for a proton, $\Delta\chi$ is the change in magnetic susceptibility from the BOLD effect (0.18 ppm), B_0 is the strength of the main magnetic field, Hct is the subject's hematocrit (percentage of red blood cells in the blood), Y is the fractional oxygen saturation of blood, and θ is the angle of the vessel orientation to B_0. Although the deoxyhemoglobin concentration is changing inside the vessel only, there is also an inverse squared frequency response outside the vessel. The equation below explains the extravascular frequency distribution:

$$\omega_{ev} = 2\pi\gamma\Delta\chi B_0(1-Y)\left(\frac{a}{r}\right)^2 sin^2\theta cos2\phi \qquad (1.4.2)$$

where a is the vessel radius, r is the cylindrical distance and ϕ is the angle of B_0 to r projected into the plane perpendicular to the vessel. These angles and radii are outlined on Figure 1.4. Importantly, both of these frequency responses have a dependence on the angle of the vessel to B_0, θ. This results in an orientation dependence of the BOLD signal being observed in GE-EPI imaging as most of the GE-EPI signal comes from pial vessels running along the surface of the cortex. There is high BOLD signal from cortical sections which are perpendicular to the main magnetic field and a lower BOLD signal when parallel due to the $sin^2\theta$ term in the extravascular equation. This effect has been shown to result in a signal difference across orientations of up to 40% [33].
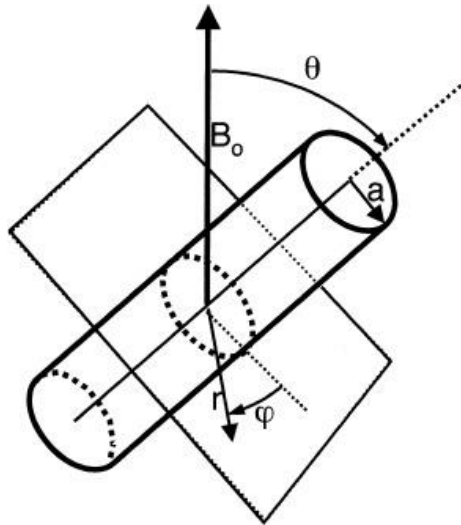
Figure 1.4: Angle definitions for a vessel in a magnetic field. Figure reproduced from Menon, MRM, 2002 [34] ©Wiley and reproduced with permission of the copyright holder.

1.4.3   Preprocessing of fMRI data

Analyzing the BOLD response requires acquisition of a series of susceptibility-weighted images which need preprocessing prior to further analysis. Functional MRI

preprocessing traditionally tries to correct for three main sources of noise in the image series: motion artifacts, physiological artifacts, and system artifacts.

1) Motion artifacts due to subject movement are usually corrected using tools that use image-based registration to align the fMRI series to a single reference image [35]. These tools generally correct for linear errors only and do not incorporate sheer or stretch. The registration parameters can be observed for spiking or high motion as a source of quality assurance. Another quality assurance method for motion correction is reviewing the timeseries for signal spikes post correction and examining the noise in the image both before and after correction. Noise at the edges should be reduced in the motion corrected case compared to the uncorrected case [36].

2) Physiological artifacts such as frequency changes due to breathing and cardiac pulsatility can interfere with BOLD analysis. This is especially true as subjects tend to change their breathing pattern in response to tasks with high cognitive loads. Physiological correction can be achieved by regressing out recorded or estimated physiological signals from the BOLD data. One example, RETROICOR, takes high temporal resolution traces of a cardiac signal (usually from a pulse oximeter) and a breathing signal (usually from a respiratory belt) and creates regressors with identical timing to the images for removal of these signals [37]. This is completed by identifying the peaks in the signal and creating sine waves matching those frequencies. This allows for the signal created to match the peaks with an arbitrary phase offset allowing for a delay which may compensate for signals occurring between the measurement location and the brain. Another method to conduct physiological correction is by estimating the physiological signal from the collected BOLD data. In general, these methods identify a mask of voxels that do not carry any neurological signals, such as the white matter or ventricles. Subsequently, these masks can be used to extract nuisance timeseries (i.e., by calculating the average or principal component time courses) which can then be used as an estimate of physiological noise. An example of this is CompCor which estimates noise regressors from a white matter mask or a mask of noisy voxels [38].

3) System noise most frequently comes in the shape of spikes across only a few volumes, frequency drift, or oscillatory noise. Spikes are detected by a de-spiking tool such as *fsl_motion_outliers* [35]. This creates a regressor of the problem volumes allowing them to be discounted from analysis. Frequency drift is usually removed using a low pass filter on the time series data and systematic frequencies can also be present and are usually detected and eliminated through corrections such as CompCor or ICA denoising [39].

1.4.4   Task based BOLD responses

Once preprocessing is completed, the data is ready to be fit to the expected hemodynamic response function (HRF). This HRF can be convolved with a stimulus waveform to estimate the expected voxel response to a stimulus design. This is possible because the HRF response has been shown to have linear characteristics, provided the space between new stimuli are at least two seconds in length for a one second event [40]. Studies have found that the HRF is somewhat inconsistent across subjects making it necessary to correct for these variations [41]. This can be corrected by allowing the convolved HRF and its derivative to both be used for signal fitting [35]. This convolved HRF, its derivative and physiological regressors are then fit to a general linear model. This fit results in estimations on a per voxel basis of the BOLD activity usually expressed as percent BOLD change or a t-statistic.

Voxel-wise estimates of the fit can be used to conduct inference on brain regions that are relevant to a specific task-based paradigm. Inference is usually completed using group statistics after multiple comparisons correction. This is done through different methods depending on the software package. For example, one such package FSL, utilizes gaussian random field theory of activated clusters to determine each cluster's significance or permutation testing to calculate a data driven threshold for significance [35]. Multiple comparison correction methods are an important step in fMRI analysis as analysis is performed across thousands of voxels in the brain.

1.4.5   Resting State BOLD responses

In addition to examining BOLD responses to a task there is an alternative paradigm aiming to measure BOLD effects in the absence of a stimulus, resting state fMRI. When the brain is not directly responding to an input, the neurons still fluctuate in activity and an activity-correlated BOLD fluctuation can still be measured, however its response shape cannot be well characterized as in the case of task based BOLD responses. Resting state fMRI is incredibly popular as a basic science and clinical research tool as it does not require additional input from subjects who may be unable to perform tasks in the scanner. Brain areas with high temporal correlation to each other define various resting state networks, that have been shown to correspond well with known functional task activation patterns, such as the motor or visual networks and more complex tasks with higher cognitive load have shown similar patterns to the salience and default mode networks [42]. Changes in these networks have been shown throughout development and in patient vs control populations [43,44].

There are two traditional methods for analysis of resting state BOLD data: seed-based analysis and spatial independent component analysis (ICA). Seed based analysis uses the signal from a specific region (the seed) and examines its correlation with the rest of the brain. When these correlations are higher it indicates the signal time courses from the two brain regions are synchronized which is inferred to mean these two regions are functionally connected [42]. Using a seed from a region known to associate with a specific network will result in high correlations with the areas of that network.

As an alternative to seed-based correlation, it is possible to perform spatial independent component analysis on the resting state data. Independent component analysis decomposes an image series into various independent spatial maps and associated time courses as well as their mixing matrix. These maps and time courses can be summed using the mixing matrix to create the original input. When applied to the resting state images from multiple runs ICA will produce a series of resting state networks and their associated patterns for an individual. This method can also be extended to find common spatial patterns across a group with can then be subdivided into specific populations (example

patient versus control) and determine if there are spatial network differences between groups [45].

A current limitation of resting-state analyses is the lack of clarity with regards to which region drives the synchronicity between two regions. High resolution fMRI may provide additional information which helps bridge this gap, to better understand the directionality of functional connectivity. For example, if the activity is in an output layer in region A and an input layer in region B, then it is probable region A is driving region B. An example of this has already been shown in the motor cortex [46].

1.4.6   High resolution BOLD analysis

Performing fMRI experiments aimed at discriminating layers and columns requires several extra considerations above the preprocessing and modelling described above. These include projecting functional data onto a surface at varying depths, sampling data across layers, registration and surface generation at high resolution and reducing pial surface bias from laminar profiles.

Surface projection is a common part of fMRI analysis at both high and low resolutions. By moving from a volume to a surface it is possible to reduce the geometrical complexity of the brain through inflation to smooth the sulci and gyri [47]. Surface projection is useful when examining features like retinotopic projections onto V1 [48] or correlating BOLD signal with cortical features like vessels and curvature [49]. At high resolution, this is made more complex by the addition of depth, as where to sample a surface in the cortical sheet is an open area of research. The easiest method is equi-distant sampling, where the amount projected along a surface normal is the same for every part of cortex. There is a competing model, the equi-volume model which shows more anatomical accuracy by preserving the volume of the cortical sheet between layers regardless of surface curvature. This has shown greater anatomical accuracy [50]. Laminar sampling is also done through projection of layers using either equi-distant or equi-volume projection and then sampling the voxels along those layers to create a profile of an area across cortical depth. This sampling is dependent on the number of layers used as well as the projection model [51].

High quality surface generation and registration is required for these surface analyses to be successful. Surface generation is an open area of research but is typically completed using a T_1 weighted image, with the software package Freesurfer and manually edited [52]. A T_2 weighted image can be included for refinement of the pial surface. Registration is also an ongoing field but at high resolutions has included the generation of an EPI space structural image [53], using registration of the surface boundaries [54] and using field map correction to prevent EPI distortions [35].

Finally, high resolution analysis that uses gradient echo or spin echo must contend with pial surface bias. This bias is a result of the pial vessel signal extending within the cortex through the extravascular bold effect. This is discussed in the next section.

1.4.7   Venous Correction of the BOLD Response

The BOLD response is constrained by vascular physiology. Due to the summation of oxyhemoglobin changes in many vessels, task based BOLD changes are observed not only in capillaries but also in draining venules and sinuses. This venous BOLD response is occurring as many capillaries drain into the same venous bed [55]. In order to obtain specificity to the capillary bed closest to the neurons of interest, it is required to correct for this large venous response. This is of upmost importance in laminar fMRI where you are trying to discriminate signal to layers <<1 mm in thickness.

The choice of MR sequences can help mitigate the effects of large pial vessel signals on the cortical surface. Varying the length of the echo train in an SE-EPI sequence will in turn, affect microvascular weighting of the image [12], however this technique comes at a cost of sensitivity. This effect results in a reduction in signal of in grey matter of 22% but reduces vessel signal by 81% [56]. Other sequences such as GRASE combine a gradient and spin echo train to help improve the resulting sensitivity [57]. By interleaving a refocusing spin echo pulse into a gradient echo readout the vascular weighting is reduced over the acquisition. VASO uses an inversion to null the blood prior to measurement and in this way can create a measure of CBV opposed to the BOLD contrast in order to measure neural activity. This has shown extreme efficacy at high resolution for layer-based studies [46,58]. However, GE-EPI remains the most popular and sensitive sequence for fMRI and

allows for wide uptake of laminar imaging across sites, and so solutions aimed at GE-EPI are the focus of this thesis.

In GE-EPI, this venous BOLD response is typically larger than the response of BOLD in tissue [56]. Several methods have attempted to reduce this bias after imaging such as temporal deconvolution [59], masking [60], modeling of the laminar PSF to reduce the effects of vascular drainage [61] and phase regression [34]. This bias can be suppressed to various degrees depending on the paradigm and is currently an ongoing field of research.

Venous correction for low resolution studies is often skipped as one typically applies spatial smoothing of the fMRI images and the voxel size already encompasses the entire cortical thickness. As a consequence, both veins and capillaries will exist within the large voxels of the resultant image and smoothing blurs these vessel populations further. This measures a population containing both venous and capillary BOLD effects but greatly increases your point spread function, potentially obscuring your activity of interest.

1.5   BOLD and Phase

Gradient echo EPI based fMRI has phase information which is usually discarded without coil combination. This phase information is collected as part of the sequence and once combined, can produce valuable insights into what is happening during the sequence and has been used several ways to refine BOLD techniques. Phase of EPI trains can be used to correct for field distortions [62], physiological noise [63], macrovascular filtering [34] or detection of fMRI signals using complex data or phase data [64].

The phase of GE-EPI images has been used for realignment and distortion removal due to local field changes from physiology like breathing. Phase images are spatially unwrapped and smoothed to determine the field perturbations across time and create a dynamic field map. This dynamic field map can be used with conventional EPI distortion correction techniques to remove GE-EPI distortions [62].

Phase data from EPI sequences contains significant signal from physiology which can be used to clean the data. Physiological signal cleaning can be performed by using

voxels with a high magnitude and phase correlation (assumed to be due to motion or breathing) and performing principal component analysis on those voxels to determine a set of regressors representative of these physiology changes [63]. This method, HighCor, is an extension of the CompCor methodology [38].

In addition to containing information about the physiology and distortions much work has been completed investigating whether phase contains meaningful BOLD signal. Recent work investigating using phase for resting state fMRI showed weak functional connectivity when compared to established magnitude networks [64]. The low functional connectivity could result from the known vessel orientation dependence of extravascular phase signal. This has also been investigated by the same group using phase to provide higher spatial specificity across a group when using complex ICA [65]. This method has shown greater sensitivity to spatial changes compared to magnitude only fMRI when comparing patients with schizophrenia and controls [66].

Functional quantitative susceptibility mapping (fQSM) has been investigated in order to evaluate the BOLD response's relationship to magnetic susceptibility [67]. Functional QSM deconvolves the phase images with the dipole kernel to produce maps of the change in magnetic susceptibility in response to a task. This change in magnetic susceptibility can be used to quantify the BOLD response.

Complex fMRI, using both the magnitude and phase data to create activation maps has shown maps with higher similarity to anatomy than the magnitude only model [68]. The motivation behind this is that the gaussian noise structures of complex data allows for stronger fits and higher power models. This technique has also been shown to perform better in low SNR regimes [69].

This thesis focuses on using phase data to remove venous signal from magnitude data prior to data analysis. This technique was proposed by Dr. Menon in 2002 [34] and has seen many extensions and studies since. Phase regression relies on the fact that voxels containing large vessels will provide a meaningful phase signal and voxels containing small vessels will not. In a voxel with many small vessels within it, such the capillary beds of the cortex, BOLD related frequency offset (Equation 1.4.1-2) will sum to zero due to

the varying orientations of these vessels. At the other extreme, in a voxel dominated by a single vessel the frequency offset due to the BOLD response will be detectable but scaled by the vessel orientation term. This effect of varying phase responses can be exploited to estimate the macrovascular content of each voxel.

This estimation, phase regression, was originally performed using chi squared minimization shown below:

$$\chi^2(\varphi, M) = \sum_{i=1}^{N} \frac{\left(M(i) - B - A\varphi(i)\right)^2}{\left(\sigma_M{}^2 + A^2 \sigma_\varphi{}^2\right)^2} \tag{1.5.1}$$

where M is the magnitude signal, φ is the phase signal, N is the number of volumes collected, and A and B are the fit coefficients. Subtraction of this estimated macrovascular signal results in the microvasculature signal:

$$M_{micro} = M - (A\varphi + B) \tag{1.5.2}$$

This technique has been expanded and investigated by several publications which are summarized in Table 1.1.

Table 1.1: Summary of Phase Regression Method Papers

Authors	Year	Title	Summary
AT Vu and JL Gallant	2015	Using a novel source-localized phase regressor technique for evaluation of the vascular contribution to semantic category area localization in BOLD fMRI [70]	Used the voxel with the highest correlation in a nearby area for phase regression. Attempted to reduce the effects of large extravascular signal in high resolution data.
RL. Barry, and JC Gore	2014	Enhanced phase regression with Savitzky-Golay filtering for high-resolution BOLD fMRI [71]	Applied a Savitsky-Golay filter (polynomial window) over phase timeseries prior to fitting. Filter order is data driven to allow for varying noise levels. Removed changes due to scanner jitter and high-frequency physiology changes.
AT Curtis, RM Hutchison, and RS Menon	2014	Phase based venous suppression in resting-state BOLD GE-fMRI [72]	Examined a band passed version of the original technique under resting state conditions. Demonstrated that resting state correlations show changes using phase regression and the macrovascular effects on resting state activation need consideration in future work.
RL Barry, SC Strother, and JC Gore	2012	Complex and magnitude-only preprocessing of 2D and 3D BOLD fMRI data at 7 T [73]	Investigated phase regression to determine the best physiology correction pipeline. Determined phase regression, Stockwell filtering and retrospective image correction led to more reproducible activation.
RL Barry, JM Williams, LM Klassen, JP Gallivan, JC Culham, and RS Menon.	2009	Evaluation of preprocessing steps to compensate for magnetic field distortions due to body movements in BOLD fMRI [74]	Investigated phase regression for the correction of motion-related field shifts generated by movement outside the imaging region. Demonstrated an improvement in statistical power when phase regression was used to correct for this effect.
RE Martin et al.	2004	Cerebral areas processing swallowing and tongue movement are overlapping but distinct: a functional magnetic resonance imaging study [75]	Applied phase regression to suppress erroneous signal due to motion from swallowing. Isolated swallowing regions of the brain without motion contamination.
DB Rowe, CP Meller, and RG Hoffmann	2007	Characterizing phase-only fMRI data with an angular regression model [76]	Compared the original technique to an angular regression. Angular regression reduced the low SNR effects present in phase timeseries with vessels close to the magic angle.
DG Tomasi, and EC Caparelli.	2007	Macrovascular contribution in activation patterns of working memory [77]	Performed phase regression using an HRF. Set all voxels above a certain statistical threshold to have no BOLD response. Demonstrated large BOLD suppression in occipital and parietal cortex in a working memory task.

1.6   Thesis Objectives

The high-level objective of this thesis was to examine the use of GE-EPI phase data in high resolution functional MRI. This first required development of a combination method that could combine coil signals to create a phase image of sufficient quality for this large, high-resolution data. This method was then used to investigate the effect of phase regression in humans and primates. We hypothesized that phase regression could be used for venous suppression in both task and resting state high-resolution fMRI. Evidence presented in this thesis supports that hypothesis and shows a marked reduction in pial vessel contamination in the human task study, although more work is required when extending this technique to macaque resting state data.

Chapter 2 outlines the coil combination method developed to combine GE-EPI phase data for the rest of this thesis. This method relies on a mixture of existing coil combination methods to estimate coil receiver sensitivities using prescans and then applies them to combine GE-EPI data. This method has low computational requirements in both memory and time. We hypothesized this combination method would provide sufficient quality phase images for further high-resolution fMRI studies.

Chapter 3 investigates the use of phase regression on high resolution GE-EPI human task-based data. To do this, we collected functional data from seven subjects on a neuro-optimized 7T system at 800 μm isotropic resolution with both GE-EPI and SE-EPI while observing an 8Hz contrast reversing checkerboard. We then directly compared GE-EPI, SE-EPI, and GE-EPI-PR across a surface and across the laminar profile. We hypothesized that GE-EPI-PR would show higher spatial similarity to SE-EPI than GE-EPI. We also hypothesized that the laminar profiles of GE-EPI-PR would approach SE-EPI and show less macrovascular bias than GE-EPI.

Chapter 4 investigates the utility of phase regression in a macaque model during resting state. Macaques are an important model for high resolution fMRI as they allow for simultaneous imaging and electrophysiology. Sources of noise were quantified and identified in both the magnitude and phase data. Two strategies for combining

physiological cleaning and phase regression were compared using seed-based resting state analysis. We hypothesized that phase regression could provide an increase in spatial specificity to resting state connectivity maps and remove any artifacts present in the magnitude and phase spectrum.

The final chapter of the thesis, Chapter 5, discusses and summarizes the findings of these three chapters. Limitations of this work are reviewed and used to develop recommendations for phase regression studies moving forward. These discussions help outline future research questions for high resolution phase regression work. Specifically, this conclusion proposes how to investigate the venous sizes affected by phase regression through a cortical orientation study.

1.7　References

1.　Raichle ME. A brief history of human brain mapping. Trends in Neurosciences. 2009;32: 118–126. doi:10.1016/j.tins.2008.11.001

2.　Ogawa S, Lee TM, Kay AR, Tank DW. Brain magnetic resonance imaging with contrast dependent on blood oxygenation. Proc Natl Acad Sci U S A. 1990;87: 9868–9872. doi:10.1073/pnas.87.24.9868

3.　Berlot E, Popp NJ, Diedrichsen J. A critical re-evaluation of fMRI signatures of motor sequence learning. Elife. 2020;9: e55241. doi:10.7554/eLife.55241

4.　Griswold MA, Jakob PM, Heidemann RM, Nittka M, Jellus V, Wang J, et al. Generalized autocalibrating partially parallel acquisitions (GRAPPA). Magn Reson Med. 2002;47: 1202–1210. doi:10.1002/mrm.10171

5.　Larkman DJ, Hajnal JV, Herlihy AH, Coutts GA, Young IR, Ehnholm G. Use of multicoil arrays for separation of signal from multiple slices simultaneously excited. J Magn Reson Imaging. 2001;13: 313–317. doi:10.1002/1522-2586(200102)13:2<313::aid-jmri1045>3.0.co;2-w

6.　Roemer PB, Edelstein WA, Hayes CE, Souza SP, Mueller OM. The NMR phased array. Magn Reson Med. 1990;16: 192–225. doi:10.1002/mrm.1910160203

7.　Uğurbil K. Imaging at ultrahigh magnetic fields: History, challenges, and solutions. Neuroimage. 2018;168: 7–32. doi:10.1016/j.neuroimage.2017.07.007

8.　Self MW, van Kerkoerle T, Goebel R, Roelfsema PR. Benchmarking laminar fMRI: Neuronal spiking and synaptic activity during top-down and bottom-up processing

in the different layers of cortex. Neuroimage. 2019;197: 806–817. doi:10.1016/j.neuroimage.2017.06.045

9. Self MW, Mookhoek A, Tjalma N, Roelfsema PR. Contextual effects on perceived contrast: figure-ground assignment and orientation contrast. J Vis. 2015;15: 2. doi:10.1167/15.2.2

10. Haarsma J, Kok P, Browning M. The promise of layer-specific neuroimaging for testing predictive coding theories of psychosis. Schizophrenia Research. 2020 [cited 2 Apr 2021]. doi:10.1016/j.schres.2020.10.009

11. Chen G, Wang F, Gore JC, Roe AW. Layer-specific BOLD activation in awake monkey V1 revealed by ultra-high spatial resolution functional magnetic resonance imaging. Neuroimage. 2013;64: 147–155. doi:10.1016/j.neuroimage.2012.08.060

12. Goense JBM, Logothetis NK. Laminar specificity in monkey V1 using high-resolution SE-fMRI. Magn Reson Imaging. 2006;24: 381–392. doi:10.1016/j.mri.2005.12.032

13. Wood IK. Neuroscience: Exploring the brain. J Child Fam Stud. 1996;5: 377–379. doi:10.1007/BF02234670

14. Naidich TP, Duvernoy HM, Delman BN, Sorensen AG, Kollias SS, Haacke EM. Duvernoy's Atlas of the Human Brain Stem and Cerebellum: High-Field MRI, Surface Anatomy, Internal Structure, Vascularization and 3 D Sectional Anatomy. Wien: Springer-Verlag; 2009. doi:10.1007/978-3-211-73971-6

15. Hubel DH, Wiesel TN. Receptive fields, binocular interaction and functional architecture in the cat's visual cortex. J Physiol. 1962;160: 106-154.2. doi:10.1113/jphysiol.1962.sp006837

16. Godlove DC, Maier A, Woodman GF, Schall JD. Microcircuitry of Agranular Frontal Cortex: Testing the Generality of the Canonical Cortical Microcircuit. J Neurosci. 2014;34: 5355–5369. doi:10.1523/JNEUROSCI.5127-13.2014

17. Schmolesky M. Figure 13, Nissl stain of the visual cortex reveals the different layers quite clearly. In: Webvision: The Organization of the Retina and Visual System [Internet]. University of Utah Health Sciences Center; 14 Jun 2007 [cited 27 Apr 2020]. Available: https://www.ncbi.nlm.nih.gov/books/NBK11524/figure/ch31visualcortex.F13/

18. Yacoub E, Harel N, Uğurbil K. High-field fMRI unveils orientation columns in humans. PNAS. 2008;105: 10607–10612. doi:10.1073/pnas.0804110105

19. Nasr S, Polimeni JR, Tootell RBH. Interdigitated Color- and Disparity-Selective Columns within Human Visual Cortical Areas V2 and V3. J Neurosci. 2016;36: 1841–1857. doi:10.1523/JNEUROSCI.3518-15.2016

20. Huettel SA, Song AW, McCarthy G. Functional Magnetic Resonance Imaging. Third Edition. Oxford, New York: Oxford University Press; 2014.

21. Duvernoy HM, Delon S, Vannson JL. Cortical blood vessels of the human brain. Brain Research Bulletin. 1981;7: 519–579. doi:10.1016/0361-9230(81)90007-1

22. Haacke EM, Brown RW, Thompson MR, Venkatesan R, Others. Magnetic resonance imaging: physical principles and sequence design. Wiley-Liss New York:; 1999.

23. Haacke EM, Xu Y, Cheng Y-CN, Reichenbach JR. Susceptibility weighted imaging (SWI). Magn Reson Med. 2004;52: 612–618. doi:10.1002/mrm.20198

24. Lee J, Shmueli K, Kang B-T, Yao B, Fukunaga M, van Gelderen P, et al. The contribution of myelin to magnetic susceptibility-weighted contrasts in high-field MRI of the brain. NeuroImage. 2012;59: 3967–3975. doi:10.1016/j.neuroimage.2011.10.076

25. Özbay PS, Deistung A, Feng X, Nanz D, Reichenbach JR, Schweser F. A comprehensive numerical analysis of background phase correction with V-SHARP. NMR Biomed. 2017;30. doi:10.1002/nbm.3550

26. Robinson SD, Bredies K, Khabipova D, Dymerska B, Marques JP, Schweser F. An illustrated comparison of processing methods for MR phase imaging and QSM: combining array coil signals and phase unwrapping. NMR Biomed. 2017;30. doi:10.1002/nbm.3601

27. Pruessmann KP, Weiger M, Scheidegger MB, Boesiger P. SENSE: sensitivity encoding for fast MRI. Magn Reson Med. 1999;42: 952–962. doi:https://doi.org/10.1002/(SICI)1522-2594(199911)42:5<952::AID-MRM16>3.0.CO;2-S

28. Kim S-G, Ogawa S. Biophysical and Physiological Origins of Blood Oxygenation Level-Dependent fMRI Signals. J Cereb Blood Flow Metab. 2012;32: 1188–1206. doi:10.1038/jcbfm.2012.23

29. Ngai AC, Ko KR, Morii S, Winn HR. Effect of sciatic nerve stimulation on pial arterioles in rats. Am J Physiol. 1988;254: H133-139. doi:10.1152/ajpheart.1988.254.1.H133

30. Thulborn KR, Waterton JC, Matthews PM, Radda GK. Oxygenation dependence of the transverse relaxation time of water protons in whole blood at high field. Biochimica et Biophysica Acta (BBA) - General Subjects. 1982;714: 265–270. doi:10.1016/0304-4165(82)90333-6

31. Pauling L, Coryell CD. The Magnetic Properties and Structure of Hemoglobin, Oxyhemoglobin and Carbonmonoxyhemoglobin. Proc Natl Acad Sci USA. 1936;22: 210–216. doi:10.1073/pnas.22.4.210

32. Ogawa S, Menon RS, Tank DW, Kim SG, Merkle H, Ellermann JM, et al. Functional brain mapping by blood oxygenation level-dependent contrast magnetic resonance imaging. A comparison of signal characteristics with a biophysical model. Biophys J. 1993;64: 803–812. doi:10.1016/S0006-3495(93)81441-3

33. Viessmann O, Scheffler K, Bianciardi M, Wald LL, Polimeni JR. Dependence of resting-state fMRI fluctuation amplitudes on cerebral cortical orientation relative to the direction of B0 and anatomical axes. NeuroImage. 2019;196: 337–350. doi:10.1016/j.neuroimage.2019.04.036

34. Menon RS. Postacquisition suppression of large-vessel BOLD signals in high-resolution fMRI. Magn Reson Med. 2002;47: 1–9. doi:10.1002/mrm.10041

35. Jenkinson M, Beckmann CF, Behrens TEJ, Woolrich MW, Smith SM. FSL. Neuroimage. 2012;62: 782–790. doi:10.1016/j.neuroimage.2011.09.015

36. Esteban O, Markiewicz CJ, Blair RW, Moodie CA, Isik AI, Erramuzpe A, et al. fMRIPrep: a robust preprocessing pipeline for functional MRI. Nature Methods. 2019;16: 111–116. doi:10.1038/s41592-018-0235-4

37. Glover GH, Li TQ, Ress D. Image-based method for retrospective correction of physiological motion effects in fMRI: RETROICOR. Magn Reson Med. 2000;44: 162–167. doi:10.1002/1522-2594(200007)44:1<162::aid-mrm23>3.0.co;2-e

38. Behzadi Y, Restom K, Liau J, Liu TT. A Component Based Noise Correction Method (CompCor) for BOLD and Perfusion Based fMRI. Neuroimage. 2007;37: 90–101. doi:10.1016/j.neuroimage.2007.04.042

39. Griffanti L, Douaud G, Bijsterbosch J, Evangelisti S, Alfaro-Almagro F, Glasser MF, et al. Hand classification of fMRI ICA noise components. NeuroImage. 2017;154: 188–205. doi:10.1016/j.neuroimage.2016.12.036

40. Dale AM, Buckner RL. Selective averaging of rapidly presented individual trials using fMRI. Hum Brain Mapp. 1997;5: 329–340. doi:10.1002/(SICI)1097-0193(1997)5:5<329::AID-HBM1>3.0.CO;2-5

41. Aguirre GK, Zarahn E, D'esposito M. The variability of human, BOLD hemodynamic responses. Neuroimage. 1998;8: 360–369. doi:10.1006/nimg.1998.0369

42. Smith SM, Fox PT, Miller KL, Glahn DC, Fox PM, Mackay CE, et al. Correspondence of the brain's functional architecture during activation and rest. PNAS. 2009;106: 13040–13045. doi:10.1073/pnas.0905267106

43. Kaiser RH, Andrews-Hanna JR, Wager TD, Pizzagalli DA. Large-Scale Network Dysfunction in Major Depressive Disorder: A Meta-analysis of Resting-State Functional Connectivity. JAMA Psychiatry. 2015;72: 603–611. doi:10.1001/jamapsychiatry.2015.0071

44. Fox MD, Greicius M. Clinical applications of resting state functional connectivity. Front Syst Neurosci. 2010;4. doi:10.3389/fnsys.2010.00019

45. Nickerson LD, Smith SM, Öngür D, Beckmann CF. Using Dual Regression to Investigate Network Shape and Amplitude in Functional Connectivity Analyses. Front Neurosci. 2017;11. doi:10.3389/fnins.2017.00115

46. Huber L, Handwerker DA, Jangraw DC, Chen G, Hall A, Stüber C, et al. High-Resolution CBV-fMRI Allows Mapping of Laminar Activity and Connectivity of Cortical Input and Output in Human M1. Neuron. 2017;96: 1253-1263.e7. doi:10.1016/j.neuron.2017.11.005

47. Fischl B, Sereno MI, Dale AM. Cortical surface-based analysis. II: Inflation, flattening, and a surface-based coordinate system. Neuroimage. 1999;9: 195–207. doi:10.1006/nimg.1998.0396

48. Winawer J, Witthoft N. Human V4 and ventral occipital retinotopic maps. Vis Neurosci. 2015;32: E020. doi:10.1017/S0952523815000176

49. Kay K, Jamison KW, Vizioli L, Zhang R, Margalit E, Ugurbil K. A critical assessment of data quality and venous effects in sub-millimeter fMRI. NeuroImage. 2019 [cited 7 Feb 2019]. doi:10.1016/j.neuroimage.2019.02.006

50. Waehnert MD, Dinse J, Weiss M, Streicher MN, Waehnert P, Geyer S, et al. Anatomically motivated modeling of cortical laminae. NeuroImage. 2014;93: 210–220. doi:10.1016/j.neuroimage.2013.03.078

51. Kemper VG, De Martino F, Emmerling TC, Yacoub E, Goebel R. High resolution data analysis strategies for mesoscale human functional MRI at 7 and 9.4T. NeuroImage. 2018;164: 48–58. doi:10.1016/j.neuroimage.2017.03.058

52. Dale AM, Fischl B, Sereno MI. Cortical surface-based analysis. I. Segmentation and surface reconstruction. Neuroimage. 1999;9: 179–194. doi:10.1006/nimg.1998.0395

53. van der Zwaag W, Buur PF, Fracasso A, van Doesum T, Uludağ K, Versluis MJ, et al. Distortion-matched T1 maps and unbiased T1-weighted images as anatomical reference for high-resolution fMRI. NeuroImage. 2018;176: 41–55. doi:10.1016/j.neuroimage.2018.04.026

54. Greve DN, Fischl B. Accurate and robust brain image alignment using boundary-based registration. NeuroImage. 2009;48: 63–72. doi:10.1016/j.neuroimage.2009.06.060

55. Menon RS. The great brain versus vein debate. NeuroImage. 2012;62: 970–974. doi:10.1016/j.neuroimage.2011.09.005

56. Yacoub E, Van De Moortele P-F, Shmuel A, Uğurbil K. Signal and noise characteristics of Hahn SE and GE BOLD fMRI at 7 T in humans. Neuroimage. 2005;24: 738–750. doi:10.1016/j.neuroimage.2004.09.002

57. De Martino F, Zimmermann J, Muckli L, Ugurbil K, Yacoub E, Goebel R. Cortical depth dependent functional responses in humans at 7T: improved specificity with 3D GRASE. PLoS ONE. 2013;8: e60514. doi:10.1371/journal.pone.0060514

58. Lu H, Hua J, van Zijl PCM. Noninvasive functional imaging of cerebral blood volume with vascular-space-occupancy (VASO) MRI. NMR Biomed. 2013;26: 932–948. doi:10.1002/nbm.2905

59. Kay K, Jamison KW, Zhang R-Y, Uğurbil K. A temporal decomposition method for identifying venous effects in task-based fMRI. Nature Methods. 2020; 1–7. doi:10.1038/s41592-020-0941-6

60. Koopmans PJ, Barth M, Orzada S, Norris DG. Multi-echo fMRI of the cortical laminae in humans at 7 T. Neuroimage. 2011;56: 1276–1285. doi:10.1016/j.neuroimage.2011.02.042

61. Markuerkiaga I, Barth M, Norris DG. A cortical vascular model for examining the specificity of the laminar BOLD signal. NeuroImage. 2016;132: 491–498. doi:10.1016/j.neuroimage.2016.02.073

62. Dymerska B, Poser BA, Barth M, Trattnig S, Robinson SD. A method for the dynamic correction of B0-related distortions in single-echo EPI at 7T. Neuroimage. 2016.

63. Curtis AT, Menon RS. Highcor: a novel data-driven regressor identification method for BOLD fMRI. Neuroimage. 2014;98: 184–194. doi:10.1016/j.neuroimage.2014.05.013

64. Chen Z, Caprihan A, Damaraju E, Rachakonda S, Calhoun V. Functional brain connectivity in resting-state fMRI using phase and magnitude data. J Neurosci Methods. 2018;293: 299–309. doi:10.1016/j.jneumeth.2017.10.016

65. Yu M-C, Lin Q-H, Kuang L-D, Gong X-F, Cong F, Calhoun VD. ICA of full complex-valued fMRI data using phase information of spatial maps. Journal of Neuroscience Methods. 2015;249: 75–91. doi:10.1016/j.jneumeth.2015.03.036

66. Qiu Y, Lin Q-H, Kuang L-D, Gong X-F, Cong F, Wang Y-P, et al. Spatial source phase: A new feature for identifying spatial differences based on complex-valued resting-state fMRI data. Human Brain Mapping. 2019;40: 2662–2676. doi:10.1002/hbm.24551

67. Balla DZ, Sanchez-Panchuelo RM, Wharton SJ, Hagberg GE, Scheffler K, Francis ST, et al. Functional quantitative susceptibility mapping (fQSM). Neuroimage. 2014;100: 112–124. doi:10.1016/j.neuroimage.2014.06.011

68. Adrian DW, Maitra R, Rowe DB. COMPLEX-VALUED TIME SERIES MODELING FOR IMPROVED ACTIVATION DETECTION IN FMRI STUDIES. Ann Appl Stat. 2018;12: 1451–1478. doi:10.1214/17-AOAS1117

69. Rowe DB, Logan BR. A complex way to compute fMRI activation. Neuroimage. 2004;23: 1078–1092. doi:10.1016/j.neuroimage.2004.06.042

70. Vu AT, Gallant JL. Using a novel source-localized phase regressor technique for evaluation of the vascular contribution to semantic category area localization in BOLD fMRI. Front Neurosci. 2015;9. doi:10.3389/fnins.2015.00411

71. Barry RL, Gore JC. Enhanced phase regression with savitzky-golay filtering for high-resolution BOLD fMRI. Human Brain Mapping. 2014;35: 3832–3840. doi:10.1002/hbm.22440

72. Curtis AT, Hutchison RM, Menon RS. Phase based venous suppression in resting-state BOLD GE-fMRI. NeuroImage. 2014;100: 51–59. doi:10.1016/j.neuroimage.2014.05.079

73. Barry RL, Strother SC, Gore JC. Complex and magnitude-only preprocessing of 2D and 3D BOLD fMRI data at 7 Tesla. Magn Reson Med. 2012;67: 867–871. doi:10.1002/mrm.23072

74. Barry RL, Williams JM, Klassen LM, Gallivan JP, Culham JC, Menon RS. Evaluation of preprocessing steps to compensate for magnetic field distortions due to body movements in BOLD fMRI. Magn Reson Imaging. 2010;28: 235–244. doi:10.1016/j.mri.2009.07.005

75. Martin RE, MacIntosh BJ, Smith RC, Barr AM, Stevens TK, Gati JS, et al. Cerebral areas processing swallowing and tongue movement are overlapping but distinct: a functional magnetic resonance imaging study. J Neurophysiol. 2004;92: 2428–2443. doi:10.1152/jn.01144.2003

76. Rowe DB, Meller CP, Hoffmann RG. Characterizing Phase-Only fMRI Data with an Angular Regression Model. J Neurosci Methods. 2007;161: 331–341. doi:10.1016/j.jneumeth.2006.10.024

77. Tomasi DG, Caparelli EC. Macrovascular contribution in activation patterns of working memory. J Cereb Blood Flow Metab. 2007;27: 33–42. doi:10.1038/sj.jcbfm.9600314

Chapter 2

2 Receiver phase alignment using fitted SVD derived sensitivities from routine prescans

This article is open access. A version of this chapter has been published in:

Magnetic resonance imaging radio frequency arrays are composed of multiple receive coils that have their signals combined to form an image. Combination requires an estimate of the radio frequency coil sensitivities to align signal phases and prevent destructive interference. Several approaches exist for ultra-high field combination that require manual intervention, specific prescans, or must be completed post-acquisition. This makes these methods impractical for large multi-volume datasets such as those collected for high-resolution functional MRI. This study proposes a fitted SVD method which utilizes existing combination methods to create a phase sensitive combination method targeted at large multi-volume datasets. This method uses a multi-image prescan to calculate the relative receive sensitivities using voxel-wise singular value decomposition. These relative sensitivities are fit to the solid harmonics using an iterative least squares algorithm. Fits of the relative sensitivities are used to align the phases of the receive coils and improve combination in subsequent acquisitions during the imaging session. This method was compared against existing approaches in the human brain at 7T by examining the combined data for the presence of singularities and changes in phase signal-to-noise ratio. The proposed fitted SVD method can combine imaging datasets accurately without supervision during online reconstruction.

2.1 Introduction

Using phase as a contrast has been a subject of interest since the development of magnetic resonance imaging (MRI). Conventional applications of MRI phase have included thermometry [1], susceptibility weighted imaging [2], quantitative susceptibility

mapping (QSM) [3,4], and velocity encoding to measure vessel flow [5]. Improvements in MRI technology and techniques has led to increased popularity of these applications and has also resulted in the development of many novel techniques that use complex data, such as functional MRI (fMRI) analysis [6–8] and the development of functional QSM [9]. These novel functional applications require the collection of large time series datasets where both the magnitude and phase data are analyzed. The current defaults provided by MRI systems are not always optimized for phase datasets and additional coil combination methods may be required [10]. One such example is the default combination for phase fMRI images which is complex sum on many systems, such as the CMRR Multiband EPI sequence on Siemens systems prior to 2017 [11]. The CMRR Multiband EPI sequence on Siemens systems after 2017 is not known to have any of the issues considered in this paper. It is advantageous to generate the phase and magnitude image volumes during reconstruction on the MRI system because exporting the complex data from each individual coil for offline reconstruction can be resource and time consuming. This is particularly true for functional MRI data sets which are routinely large due to their multi-volume nature.

Phase reconstruction is complicated by the use of multi-element receive arrays that are composed of 32, 64 or more radio frequency (RF) coils. Each RF element in these arrays has a complex, spatially varying receive coil sensitivity profile which weights the measured signal of that element. To form an image with optimal signal-to-noise ratio (SNR), RF arrays require accurate receive coil sensitivities during image combination. At lower magnetic fields, relative receive coil sensitivities are typically obtained by using a reference coil or body coil with a spatially homogeneous sensitivity profile [12]. At ultra-high fields, body coils are rarely available, and if they are, they suffer from poor homogeneity [10]. This translates to poor relative complex-valued sensitivity estimates and thus poor combination of phase data. These in turn result in a reduction in SNR and, in the worst case, phase singularities in the combined phase images. Phase singularities can be caused by destructive interference between coils as the magnitude sums to zero and the phase is undefined. These phase singularities cause issues for downstream phase processing such as spatial unwrapping and high pass

filtering [10] and can also be mistaken for pathology [4]. A successful coil combination method should not introduce phase singularities into the combined data.

Coil combination in absence of a physical reference coil has many possible solutions that can be organized into two main categories: inline, where combination is done on the MRI system as images are acquired and reconstructed, or offline, where combination occurs post-acquisition after all volumes have been collected and the data is exported off the MRI system. For large multi-volume imaging sets like those used in fMRI or fQSM, fast, robust, and automatic inline combination is essential to an efficient workflow, as data transfer and handling for offline processing becomes prohibitive. Inline combination methods include complex sum, adaptive combine [13], the virtual reference coil (VRC) [14], and the virtual body coil (VBC) [15]. These methods can often experience issues with robustness. Complex sum and adaptive combine create combinations with phase singularities, indicating their poor combination quality. The VRC method is susceptible to error because it relies on calculating phase of the virtual coil relative to a single voxel [14]. If this voxel is poorly selected, VRC requires user intervention to correct this error. This results in suboptimal combination without user supervision. The VBC method relies on compressing the data globally using a singular value decomposition (SVD) across the image. This can yield suboptimal combinations when completed at ultra-high fields [15,16]. Thus, while these inline implementations are fast enough to be used for high resolution phase imaging, they tend to lack robustness and require user supervision [10,17].

Post-acquisition combination methods require all the data to be collected before combination, making them difficult to apply to large datasets as they require the complex data from each coil to be exported, resulting in 32x to 64x larger amounts of data for typical studies performed with a head coil array. Common offline combinations include voxel-wise SVD [13], combining phase images from array coils using a short echo time reference scan (COMPOSER) [17], Block Coil Compression (BCC) [16], and the Adaptive Combine Phase Solution [18]. Voxel-wise SVD can be parallelized across voxels, but because all the processing must occur after acquisition is completed it would introduce significant processing delays if implemented inline for long time-series data

such as fMRI. COMPOSER uses a specialized short echo reference prescan and relies on scan-to-scan alignment which is completed using software such as FSL [19], which is not available on vendor-implemented reconstruction systems. Additionally, COMPOSER can result in edge effects such as Gibbs ringing when a low frequency prescan is used [20]. BCC uses a modification of the VBC method to initialize an ESPIRiT reconstruction [21] as ESPIRiT at ultra-high fields requires a locally varying phase estimate to capture the coil sensitivities. Unfortunately, BCC has high compute costs and would not be feasible on large datasets without refactoring. The adaptive combine phase solution [18] uses an SVD on a block of voxels to combine data with smooth image phase but may not be optimal for ultra-high fields. These solutions all yield optimal or near optimal SNR combinations but are hard to implement for larger imaging datasets, such as time-series data.

One possible option to expand on existing offline coil combination methods is to use them on low resolution data to create a reference coil that can be applied to every imaging scan with minimal overhead. One potential method to generalize coil sensitivities from a low resolution prescan to higher resolution images is to fit them to a physically plausible basis. Previous work has shown that RF coil sensitivities are governed by the Helmholtz equations [22]. These equations rely on a wave number that is variable across the brain and can be difficult to estimate [23]. As an alternative, we suggest a relaxation of the Helmholtz equations whose solution is the solid harmonics. This basis is similar to the Helmholtz solution without the complexity of estimating a wavenumber. Fitting sensitivity profiles to the solid harmonics would allow them to be applied quickly to all images acquired during the imaging session.

Coil combination of large imaging sets requires an inline method that is robust across the imaging session. Our proposed approach uses existing small, low-resolution datasets to estimate coil sensitivities, in order to reduce the processing time requirements. These sensitivity estimates are then fit to a functional basis, allowing the estimates to be applied inline to any acquired geometry. Throughout the manuscript this method is referred to as the fitted SVD method and is outlined graphically in Figure 2.1. The fitted SVD method exploits the use of the routinely acquired B_1^+ shimming prescan on our

parallel transmit (pTx) enabled 7T scanner in order to calculate relative receive coil sensitivities using a voxel-wise SVD. The use of SVD-derived sensitivities is similar to work done by previous groups that have used ESPIRiT [21], BCC [16] or the Adaptive Combine Phase Solution [18]. These relative receive coil sensitivities, as a consequence of the SVD algorithm, contain an arbitrary common phase which must be removed to allow accurate fitting. This common phase can be removed using a robust virtual reference coil [14] created through a minimax algorithm. The corrected relative coil sensitivities can then be iteratively fit to a physically plausible basis of solid harmonics to create a computationally efficient representation. The phase of these fitted coil sensitivities can be applied to align imaging data prior to complex sum combination to produce phase images. Hence, our proposed fitted SVD method is the amalgamation of ESPIRiT [21], voxel-wise SVD combination [13], VRC combination [14] and the Sbrizzi representation of sensitivities [22]. Combining these methods yields a technique tailored for robust acquisition of large multi-volume datasets for complex fMRI or fQSM, and additionally, may be applied to other acquisitions in the same session.
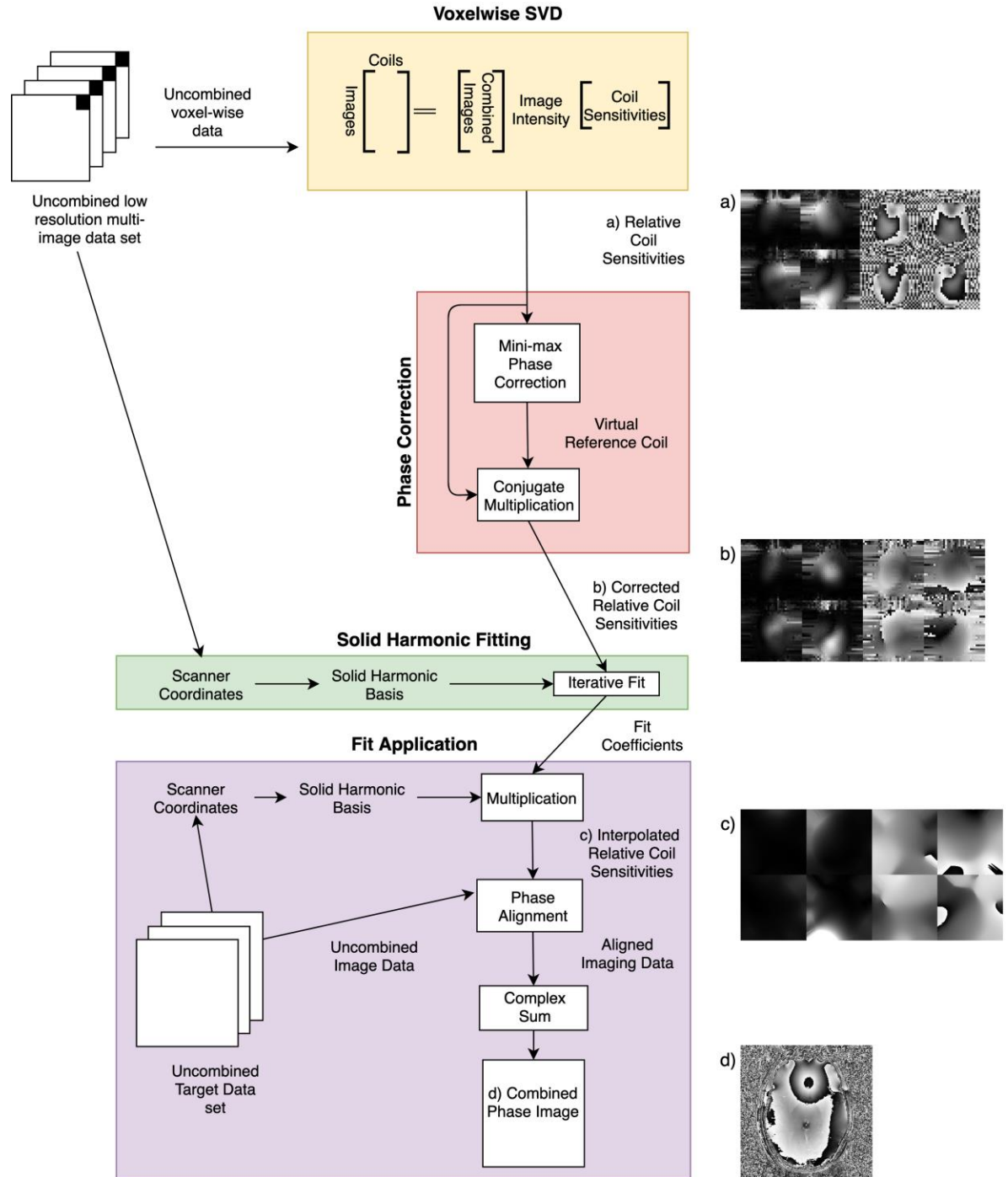
Figure 2.1: Flow chart of the Fitted SVD method. Images represent example coil sensitivities across the same slice of the brain (four of 32 shown). The four left images are magnitudes of the coil sensitivities, and the four right images are phases of the coil sensitivities. a) Relative coil sensitivities calculated by voxel-wise SVD in prescan space, b) Coil sensitivities after alignment to a virtual reference coil created through minimax optimization across prescan space, c) Fitted coil sensitivities in target image space, d) Combined phase image after alignment with fitted coil sensitivities.

37

2.2   Methods

2.2.1   Mathematical Methods

Calculation of the relative receive coil sensitivities

The relative receive coil sensitivities can be calculated from a conventional voxel-wise SVD combination as follows. The measured complex-valued signal s from a voxel is given by the integral of the product of the receive coil sensitivity c and the magnetization m over the sensitivity volume of the voxel.

$$s = \int c(r)m(r)dV \qquad (2.2.1)$$

If either the coil sensitivities or the magnetization are assumed to be uniform over the integrated region, then the integral becomes separable and measured signal is given by the product of the average sensitivity $\bar{c}$ and the average magnetization $\bar{m}$.

$$s = \bar{c}\bar{m} \qquad (2.2.2)$$

Assuming the coil sensitivity is constant in time, i.e., over multiple images, then a voxel's measured signal for the ith coil and the jth image is given by

$$s_{i,j} = \bar{c}_i\bar{m}_j \qquad (2.2.3)$$

This can be represented as a rank one matrix $\mathbf{S}$, where $\mathbf{c}$ is the vector of coil sensitivities and $\mathbf{m}$ is the vector of magnetizations across images, and T is the transpose operator.

$$\mathbf{S} = \mathbf{cm}^T \qquad (2.2.4)$$

Assuming the noise in the measurements is uniform and normally distributed, the optimum least squares low rank approximation of $\mathbf{S}$ is given by the SVD [24], where the first left and right singular vectors give the best estimate of $\mathbf{c}$ and $\mathbf{m}$, respectively. As singular vectors are defined to have unit norm, the magnitudes of $\mathbf{c}$ and $\mathbf{m}$ are contained in the first singular value, λ_1:

$$\lambda_1 = (\mathbf{c}^H \mathbf{c} \mathbf{m}^H \mathbf{m})^{1/2} \tag{2.2.5}$$

where H is the Hermitian conjugate. This deconstruction works with any number of coils and images greater than zero and is equivalent to the traditional sum of squares combination when only one image is used. However, the accuracy of $\mathbf{c}$ and $\mathbf{m}$ estimates is improved with increasing numbers of images. Estimation of $\mathbf{c}$ and $\mathbf{m}$ also improves with large variation in contrast in the images, such as in B_1^+ mapping.

Phase correction of the relative receive coil sensitivities

The SVD of a complex matrix is only unique up to an arbitrary phase. Typically, the phase of the first element of the left or right singular vector is assigned to zero to impose a unique solution. If the phase of the right singular vector, i.e., $\mathbf{m}$, is set to zero, this forces the phase of the magnetization for the first image, $\varphi_\mathbf{m}$, to be assigned to $\mathbf{c}$. The estimated complex-valued coil sensitivity, $\mathbf{c}'$, is then defined as:

$$\mathbf{c}' = \mathbf{c} \frac{m_1^H}{(m_1^H m_1)^{1/2}} = \frac{\mathbf{c}}{|\mathbf{c}|} e^{-i\varphi_\mathbf{m}} \tag{2.2.6}$$

$\varphi_\mathbf{m}$ comes from numerous sources, including the B_1^+ phase, off-resonance phase accrued from B_0 inhomogeneities, and acquisition timing. It is preferable to set the phase of an image to zero because it is likely to be well defined over the entire imaging region, whereas the sensitivity of the first coil will often have areas where its magnitude approaches zero and the phase is therefore ill defined. Because $\varphi_\mathbf{m}$ contains B_1^+ contributions, it may contain phase singularities related to destructive interference during excitation. This is particularly an issue with parallel excitation schemes or ultra-high magnetic fields. These phase singularities introduced by $\varphi_\mathbf{m}$ do not correspond to magnitude nulls in the coil sensitivities and make solid harmonic fitting difficult. Therefore, it is necessary to remove $\varphi_\mathbf{m}$ from the coil sensitivity estimates. For a single voxel, any linear combination of $\mathbf{c}'$ with weights, $\mathbf{w}$, will also contain $\varphi_\mathbf{m}$ and can be applied to $\mathbf{c}'$ to remove $\varphi_\mathbf{m}$ as follows:

$$\tilde{\mathbf{c}} = (\mathbf{w}^H \mathbf{c}')^H \mathbf{c}' = \left(\mathbf{w}^H \frac{\mathbf{c}}{|\mathbf{c}|} e^{-i\varphi_{\mathbf{m}}}\right)^H \frac{\mathbf{c}}{|\mathbf{c}|} e^{-i\varphi_{\mathbf{m}}} = \left(\mathbf{w}^H \frac{\mathbf{c}}{|\mathbf{c}|^2}\right)^H \mathbf{c} \qquad (2.2.7)$$

where $\tilde{\mathbf{c}}$ represents the coil sensitivities with $\varphi_{\mathbf{m}}$ removed. Since $\mathbf{c}$ is desired, the

optimum $\mathbf{w}$ would result in $\frac{\mathbf{w}^H \mathbf{c}}{|\mathbf{c}|^2}$ being one. To maintain spatial phase coherence, the same

$\mathbf{w}$ must be used for all voxels. Therefore, we want $\mathbf{w}$ that provides a spatially uniform

virtual reference coil. We extend the voxel-wise case across the image by defining $\mathbf{C}'$ as

the matrix of all the relative sensitivities across all k voxels in the image as shown.

$$\mathbf{C}' = [\mathbf{c}'_k] \qquad (2.2.8)$$

Finding $\mathbf{w}$ which makes $\frac{\mathbf{w}^H \mathbf{c}}{|\mathbf{c}|^2}$ spatially uniform over all voxels is difficult and simply

minimizing least-square deviation can lead to solutions with signal nulls which may

remain in the final combination. These signal nulls are problematic because they

introduce phase singularities common to all coils prior to fitting. This could result in

phase singularities in the final image which will interfere with downstream processing.

Alternatively, a robust elimination of signal nulls can be obtained via the use of a

minimax algorithm which maximizes the minimum value of the combination across the

image.

$$\max_{\mathbf{w}} \min_{k} |\mathbf{w}^H \mathbf{C}'| \qquad (2.2.9)$$

This minimax estimation is restricted to the imaging volume by defining a SNR-based

mask created via SNR threshold as discussed below in "Masking Considerations". Using

this method for finding $\mathbf{w}$ provides a non-uniform but signal null free $\mathbf{w}^H \mathbf{C}'$ for removing

$\varphi_{\mathbf{m}}$. The corrected relative coil sensitivities for all k voxels are

$$\tilde{\mathbf{C}} = [\tilde{\mathbf{c}}_k] \qquad (2.2.10)$$

and is weighted by this minimax generated virtual reference coil.

Fitting the relative receive coil sensitivities to a solid harmonic basis

In order to apply the relative coil sensitivities, it is necessary to represent them using a form that can be generalized to different orientations and resolutions. This can be done by fitting $\tilde{\mathbf{C}}$ to a physically plausible basis in order to interpolate the estimated sensitivities. Such a basis set are the solid harmonics, which are composed of polynomial functions. If the coil sensitivities can be modeled as solid harmonics, $\tilde{\mathbf{C}}$ can also be modelled using solid harmonics of higher order because it is the product of two coil sensitivities. A solid harmonic fitting basis is chosen for two reasons. First, solid harmonics are an efficient basis for spheroid shapes, such as human and animal heads. Secondly, the B_1^- field, which governs the coil sensitivities, in a homogeneous medium follows the Helmholtz equation. The general solution of the Helmholtz equation is similar to the solid harmonics and therefore the solid harmonics are a physically plausible basis set that can be used to approximate the true B_1^- field behavior.

Fitting to the solid harmonics is completed using variable exchange. After removal of $\varphi_{\mathbf{m}}$, $\tilde{\mathbf{C}}$ will contain a virtual reference coil sensitivity component. This means that $\tilde{\mathbf{C}}$ has an unknown common voxel-wise complex spatial scaling across coils, $\mathbf{d}$. This common voxel-wise scaling originates from the minimax virtual reference coil and does not affect the relative phase of the individual relative coil sensitivities and its removal will only serve to improve interpolation quality. However, as $\mathbf{d}$ is only estimated, there could remain an incomplete removal of the virtual reference coil or physical common phase (such as B_1^+ phase) which may result in a low frequency spatial phase offset in phase images which will require background removal. As a result, this combination is best used for phase images for which further analysis uses phase differences [6,9] or will employ postprocessing methods to remove low frequency background patterns [25]. Post processing to remove low frequency patterns would aid in correcting any asymmetry introduced into the image by incomplete removal of $\mathbf{d}$.

The solid harmonic basis A is defined below where r, θ, φ represent the spherical coordinates, N is the maximal fit order, and Y_m^l is a spherical harmonic

$$A(r, \theta, \varphi) = \sum_{l=0}^{N} \sum_{m=-l}^{l} \sqrt{\frac{4\pi}{2l+1}} r^l Y_m^l(\theta, \varphi) \qquad (2.2.11)$$

41

The exchange is set up in two steps as follows:

$$min \sum_i |\mathbf{AX} - diag(\mathbf{d})\tilde{\mathbf{C}}|^2 \; s.t. \; \mathbf{d}^H\mathbf{d} = k \qquad (2.2.12)$$

Where X is the fit coefficients, $diag(\mathbf{d}) = \begin{bmatrix} d_1 & \cdots & 0 \\ \vdots & \ddots & \vdots \\ 0 & \cdots & d_k \end{bmatrix}$ and k is the number of voxels

in the fit. The iteration begins with the calculation of $\mathbf{X}$ through least squares fitting. $\mathbf{d}$ is then calculated from $\mathbf{AX} = diag(\mathbf{d})\tilde{\mathbf{C}}$ and applied to the next iteration. The least squares fit was weighted by the square-root of the first singular value ($\sqrt{\lambda_1}$) in order to reduce the effects of noise in areas of low signal. The scaling of $\mathbf{d}$ is required to avoid the trivial $\mathbf{X} = 0, \mathbf{d} = 0$ solution. Fitting is completed over an SNR-based mask and is continued until the residuals of the least-squares fit change by less than 0.01%. The fit coefficients can then be used to estimate phase of the relative coil sensitivities and align receivers prior to combination.

Image combination

The application of the relative sensitivity estimates can be done inline as each image is reconstructed. The complex signals are multiplied by the normalized conjugate of the relative sensitivity estimates and combined via a complex sum to create a complex image. This operation is applied voxel-wise as shown:

$$v = \frac{\tilde{\mathbf{c}}^H}{|\tilde{\mathbf{c}}|}\mathbf{s} \qquad (2.2.13)$$

The resulting phase of this image should be free of singularities and have high SNR. This could be further improved by inclusion of the noise covariance matrix if desired [12].

2.2.2   Masking Considerations

The fitted SVD method is reliant on masking out the regions without sensitivity information. To accomplish this, an SNR estimate was created using the ratio of the first and second singular values. This ratio is then thresholded by a hyperparameter in order to

determine which voxels in the imaging volume should be included in either the minimax algorithm or the fitting. The effect of the threshold on the minimax algorithm was examined over nine values from 5 to 45. A second SNR threshold was applied during least squares fitting and was also tested over values from 5 to 45.

In order to apply the relative sensitivity estimates to images with differing geometries from the prescan it is necessary to constrain the fitted sensitivities to only parts of the image where the prescan data was able to estimate the sensitivities. Due to the known poor extrapolation performance of polynomial fits, a convex hull around all voxels used in the least squares fitting is computed. When applying the fit for phase alignment, voxels within the convex hull are aligned based on the fit and exterior points are aligned based on the fit at the closest point on the convex hull. This allows the method to be applied to differing fields of view and ensures only reliable coil sensitivity estimates are used.

2.2.3   Imaging

All imaging was completed on the 68 cm bore 7T Siemens Magnetom Step 2.3 System equipped with an AC-84 Mark II head gradient coil located at the Centre for Functional and Metabolic Mapping at the University of Western Ontario. Imaging of three healthy volunteers (ages 23-27) was performed with written informed consent and approved by the Human Subjects Research Ethics Board at the University of Western Ontario. To investigate the fitted SVD method three datasets were acquired with one subject each: one dataset to compare the fitted SVD method to existing combinations, one dataset with an asymmetrical coil, and one dataset with subject motion.

Dataset 1: Comparative Combination

This experiment used a whole head coil with a conformal 32 channel receive array and an eight channel transmit array operated in parallel transmit mode [26]. Three sets of images were acquired. First, prescan data was acquired for B_1^+ shimming which was then used as the low-resolution input for the fitted SVD method. This data consisted of one actual flip-angle imaging map [27] (TE/TR=2.75/20 ms, FA=70º) and 8 fourier

encoded B_1^+ images [28] (TE/TR=2.75/6 ms, FA=5°) with an 8 mm isotropic resolution, matrix size of 32x32x32, and BW=1000 Hz/pixel. Next, an ultrashort echo time prescan was acquired to allow for comparison to COMPOSER [17], this data was a gradient recalled echo (GRE) with a resolution of 2x2x4 mm, matrix size 128x122x52, TE/TR=0.8/5ms, FA=10°, BW=810 Hz/pixel and no acceleration. Finally, an acceleration free GRE sequence was collected 10 times. Five GRE images were used to generate high resolution coil sensitivities for testing the fitted SVD method on parameter matched data and five were used to calculate the voxel-wise SVD solution for the quality ratio calculation as well as serve as the target volume to combine when different combinations were compared. This target GRE sequence had a 1 mm isotropic resolution, matrix size 210x210x60, TE/TR=7.7/15 ms, FA=15°, BW=140 Hz/pixel.

Dataset 2: Asymmetrical Coil

This experiment used a highly asymmetric head coil with a conformal 32 channel receive array and eight channel transmit array also operated in parallel transmit mode, with both transmit and receive coils covering only the occipital-parietal regions [29]. This dataset consisted of two image sets, a B_1^+ prescan as described above and a gradient echo echo planar image set (GE-EPI) collected as the target image set to combine. The GE-EPI had a 2 mm isotropic resolution, matrix size 104x104x54, TE/TR=20/1250 ms, FA=45°, BW=1457 Hz/pixel and GRAPPA factor 3 with 36 reference lines [11].

Dataset 3: Subject Motion

This dataset was collected with a third coil that is the next generation whole head coil from the coil used for Dataset 1. It was a 32 channel receive array and eight channel transmit array with dipoles (rather than loops) as transmit elements and loops as receive elements [30]. As the dataset was investigating motion it was acquired in two parts. Part one consisted of a B_1^+ prescan and 5 GRE images without motion. Part two then instructed the subject to move in the coil before an additional GRE and another B_1^+ prescan were collected. This allows assessment of the fitted SVD method in the case of subject motion. Due to an intervening MRI system upgrade the prescan parameters are slightly different than the other two sets. The prescan data still consisted of one actual

44

flip-angle imaging map [27] (TE/TR=2.84/20 ms, FA=50º) and 8 fourier encoded B_1^+ images [28] (TE/TR=1.75/3.8 ms, FA=3º) with an 8 mm isotropic resolution, matrix size of 32x32x32, and BW=1000 Hz/pixel. The target GRE sequence was collected identically to the target GREs in Dataset 1.

2.2.4   Comparison Metrics

To compare different combination techniques, three methods were employed. First, the output phase was unwrapped [31] and examined for singularities inside the volume of interest. Second, to quantify the performance of the fitted SVD method relative to other combinations, the quality ratio was measured across the target dataset for each combination method. The quality ratio is a measure of magnitude signal loss and therefore will be proportional to the phase SNR [32]. The quality ratio is defined as:

$$Q = \frac{|S_{method}|}{|S_{VSVD}|} \qquad (2.2.14)$$

where S_{method} is the complex signal resulting from the combination method of interest and S_{VSVD} is the complex signal resulting from a voxel-wise SVD combination. This is a modification of the quality factor which uses the sum of the magnitudes in the denominator [10,17]. The magnitude sum has a noise bias that is not present in the voxel-wise SVD combination. All average quality ratios are calculated across a brain mask excluding voxels less than 3% of the median value to reduce outliers such as large veins where signal is naturally too low to compare combination techniques [17]. Brain masks were generated based off sum-of-squares combined magnitude images using FSL's Brain Extraction Tool (5.10.0) [19] and then eroded once using fslmaths. Finally, to compare the relative runtime of the different methods, all combinations were run single-threaded on a Centos 6.0 system with 256 GB of memory and Intel Xenon E5-2760 CPU and the reported runtime is the average clock time in seconds that the operation took to complete over five runs. This was performed single threaded as not all comparative combinations were available in a multi-threaded implementation.

2.2.5 Fitted SVD Parameter Selection

Three input hyperparameters are required to use the fitted SVD method: the SNR-based mask thresholds for the minimax and least squares fitting steps as well as the fit order. In order to determine the optimal hyperparameter set in the case were the B_1^+ prescan is used to create sensitivities, the fit was run from solid harmonic orders one to ten as well as nine equally spaced masking thresholds between 5 and 45 for both the minimax correction and solid harmonic fitting. The mean quality ratio and the coefficient of variation of the quality ratio were examined across the brain mask to determine the optimal hyperparameter set. The coefficient of variation is defined as:

$$CV = \frac{\sigma}{\mu} * 100 \tag{2.2.15}$$

Where σ is the standard deviation of the quality ratio over the brain mask and μ is the mean quality ratio over that mask. The mean quality ratio determines what degree of signal loss that a parameter set incurs but the coefficient of variation ensures that the spread in quality ratio is consistent across the brain.

2.2.6 Comparative Combinations

Complex sum, voxel-wise SVD [13], VRC [14], COMPOSER [17], and the fitted SVD method were all implemented using in-house MATLAB code (R2018a) that is available at: https://gitlab.com/ostanley1/phasecombofunctions-matlab. These are also briefly described below. The BCC method [16] was implemented using the toolbox provided by the authors.

At the time of development, complex sum was the default on the MRI system for functional phase data (CMRR-MB on the Siemens scanner [11] prior to R16 (2017)). Complex sum is a simple sum of all the coil data followed by a calculation of the phase. We were particularly interested in the CMRR-MB sequence for studying the phase effects of large vessels in fMRI, but the method we propose is applicable to all types of images, where appropriate phase combinations may still not be available.

Voxel-wise SVD [13] is completed by calculating the SVD of a matrix formed by volumes and coils. To prevent singularities resulting from the arbitrary phase of the SVD, the phase of the first volume is set to zero making this method a measure of relative phase as opposed to absolute phase.

The VRC method [14] uses a voxel as a reference to align the coil images and create a reference coil. The reference voxel is chosen as the voxel with the largest minimum magnitude across all coils [14]. This voxel's phases are then subtracted from each coil profile before summation to create a virtual reference coil. This virtual reference coil is then subtracted from each coil profile to create phase offsets which are smoothed with a three-dimensional 10mm gaussian blur and used to align the data prior to combination.

COMPOSER [17] was implemented using the FSL registration tool FLIRT (5.10.0) on the magnitude images to determine the transformation between the short echo time reference image and the target data. Uncombined coil data was then saved to real and imaginary NIFTIs, and this transformation was applied to both the real and imaginary components separately [19]. These transformed reference images were used to remove shared coil signal prior to image combination using complex sum.

The BCC method [16] uses a regional SVD to create a common reference coil block by block, followed by aligning adjacent blocks to ensure phase smoothness. Once this reference data is created the data undergoes an ESPIRiT combination [21] using the newly created virtual coil as a reference channel to ensure successful phase combination.

The fitted SVD method was completed on the B_1^+ shimming dataset and a set of five matched scans identical to the target image set. This was done to examine the effects of using a prescan for fitting and to compare against a reference approach using identical parameters to the target image set. The method was developed to use a multi-image prescan such as the B_1^+ shimming datasets because they are routinely collected on pTx systems and can be used with no additional imaging time requirements. On non-pTx systems other multi-image sets could be used such as those collected for B_0 shimming to obtain the same time benefits.

2.2.7   Temporal Noise

To compare the noise across time the EPI data from Dataset 2 was used. The fitted SVD method was used to calculate sensitivities from the B_1^+ prescan and was applied to each volume in the EPI series. As comparators, the VRC and BCC sensitivities were calculated from the first volume and applied to every volume in the series and voxel-wise SVD was performed across all volumes. Finally, the fitted SVD method was performed using the sensitivities from the voxel-wise SVD as input, a case equivalent to performing the fitted SVD method on matched image data. Once these time series were created the phase of the first volume was removed and the images were unwrapped through time to remove any jumps of 2π. In order to remove system drift, the time series were linearly detrended voxel-wise prior to calculating the phase noise. The temporal standard deviation was then calculated to create phase noise images. The phase noise ratio between each combination and the voxel-wise SVD was used to investigate differences in phase noise levels between combinations. It is defined as:

$$Phase\ Noise\ Ratio = \frac{\sigma_{method}}{\sigma_{VSVD}} \tag{2.2.16}$$

where σ_{method} is the temporal standard deviation of the phase time course for the combination method of interest and σ_{VSVD} is the temporal standard deviation of the phase time course for the voxel-wise SVD. Comparing noise relative to a reference method removes sources of variance shared across combination methods such as an increase in noise in lower SNR areas of the asymmetric coil.

2.3   Results

2.3.1   Fit Order and Masking Threshold Selection

The fitted SVD method relies on three hyperparameters: the thresholds for the SNR-based masks during minimax phase correction and solid harmonic fitting as well as the order of the solid harmonic basis. The effect of solid harmonic order and SNR-based masking during the fit are shown in Figure 2.2 for a single subject. To assess performance the quality ratio was averaged over an eroded brain mask generated using

FSL's BET tool on all sixty slices (example Figure 2.3). These results show there is a large parameter space which allows for high quality combinations. For this paper the chosen parameters were SNR-based mask thresholds of 20 for the minimax algorithm and 20 for the least squares fitting and a basis of solid harmonic order 6 which yields a high mean quality ratio of 0.96±0.04 (μ±σ) and a low coefficient of variation of 4.4%. This shows that using a low resolution prescan slightly reduces phase SNR (4% reduction), but still effectively combines the data.
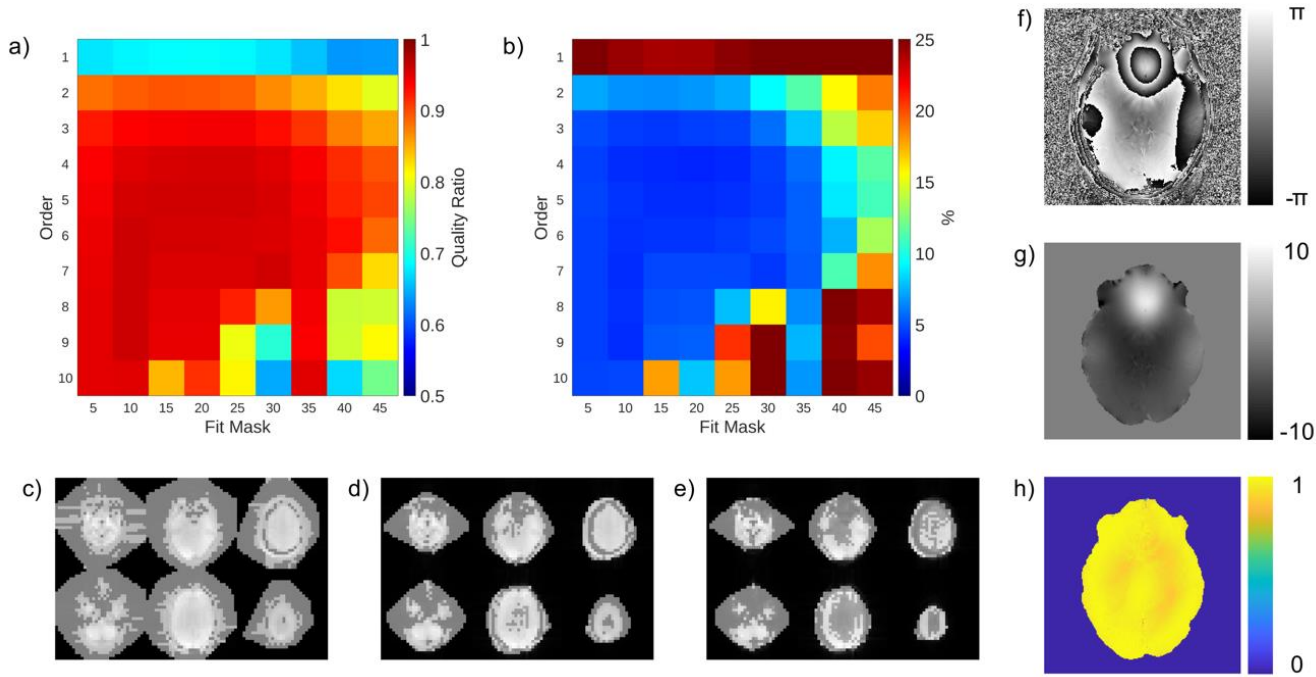
Figure 2.2: Fitted SVD Method in a human using B_1^+ prescan data from a single subject. a) Average quality ratio and b) coefficient of variation of quality ratio as a function of fit order and fit mask size. Example convex hull (grey) and voxels included in fit (white) for various mask thresholds c) 10, d) 20, e) 30. f) Example phase image, g) unwrapped phase image, and h) quality ratio map at the selected parameters (order 6, fit mask of 20, minimax mask of 20).
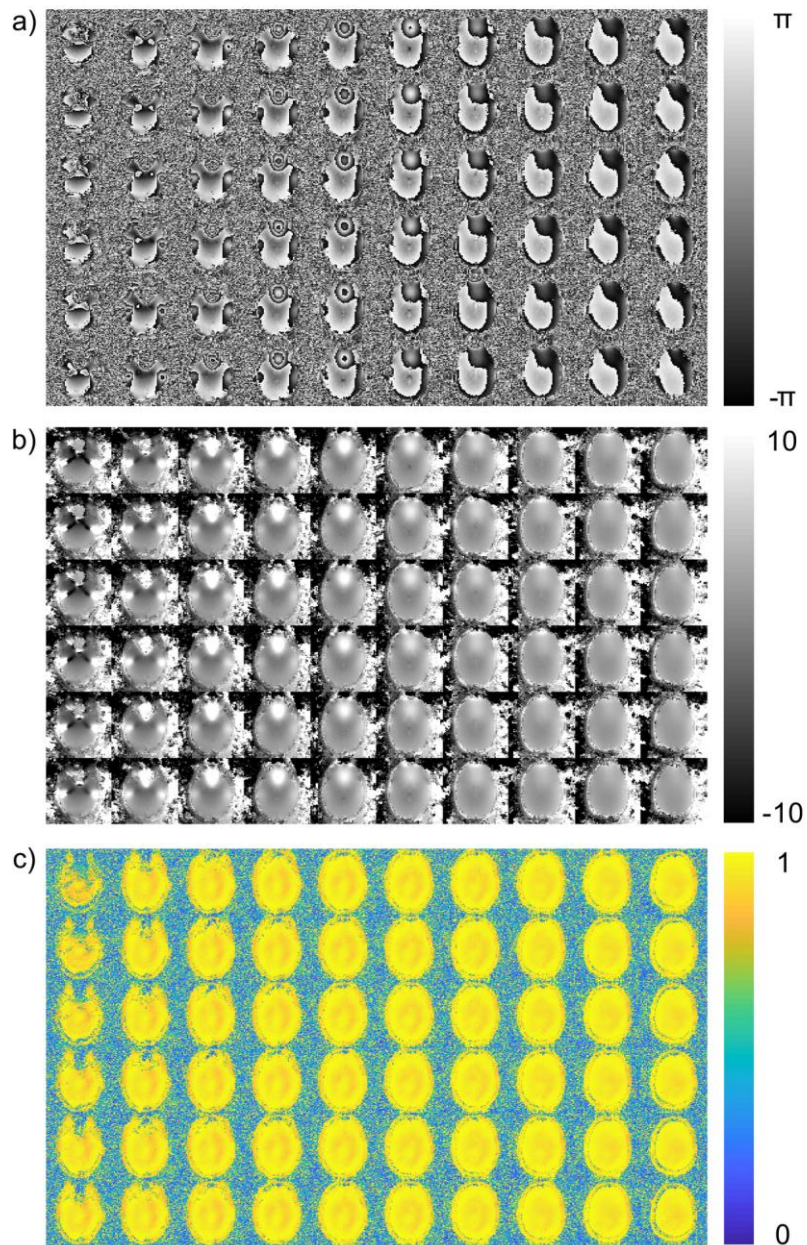
Figure 2.3: All slices of Dataset 1 for inspection for artifacts. a) phase image, b) unwrapped phase image, and c) quality ratio map at the selected parameters (order 6, fit mask of 20, minimax mask of 20).

2.3.2 Fitted SVD and Comparative Methods

To investigate the quality of the fitted SVD method against other benchmarks, three criteria were used: singularities, quality ratio, and runtime. Figure 2.4 shows a

qualitative comparison between complex sum, VRC, the fitted SVD method using prescan data, COMPOSER, BCC, voxel-wise SVD combination, and the fitted SVD method using a parameter matched image set. Receiver-based phase singularities can indicate destructive interference, the worst case of coil combination, and any phase combination method should not produce these artifacts. Singularities present in the complex sum are corrected in all the combination methods except the VRC method. Singularities can also be present due to global phase shared across coils and in this case still present post processing difficulties that need to be corrected. This was the case in the VRC combination where it was not possible to obtain an acceptable virtual coil for the VRC method using the maximum shared signal method for voxel selection [14]. The voxel selected was outside the brain in our target data and produced a reference with signal nulls and phase singularities (Figure 2.5). Unfortunately, this is not a robust option for phase combination as the singularity introduced by the reference coil will cause downstream processing issues when the data is further analyzed. For the fitted SVD method, the minimax algorithm was used to overcome this inherent VRC limitation. One additional observation is that most methods do result in a left-right asymmetry that can be seen in the wrapped and unwrapped phase images. The images in Figure 2.4 are sorted by relative runtime. One consideration when comparing runtimes is that fitted SVD method runtimes include both relative receive sensitivity estimation and fitting as well as applying the fit to the target dataset. The estimation of the fitted sensitivities needs to only be done once per session and then can be applied to the remaining images in the session. This application of the fitted sensitivities takes 18 seconds on the target data when the prescan was used for fitting.
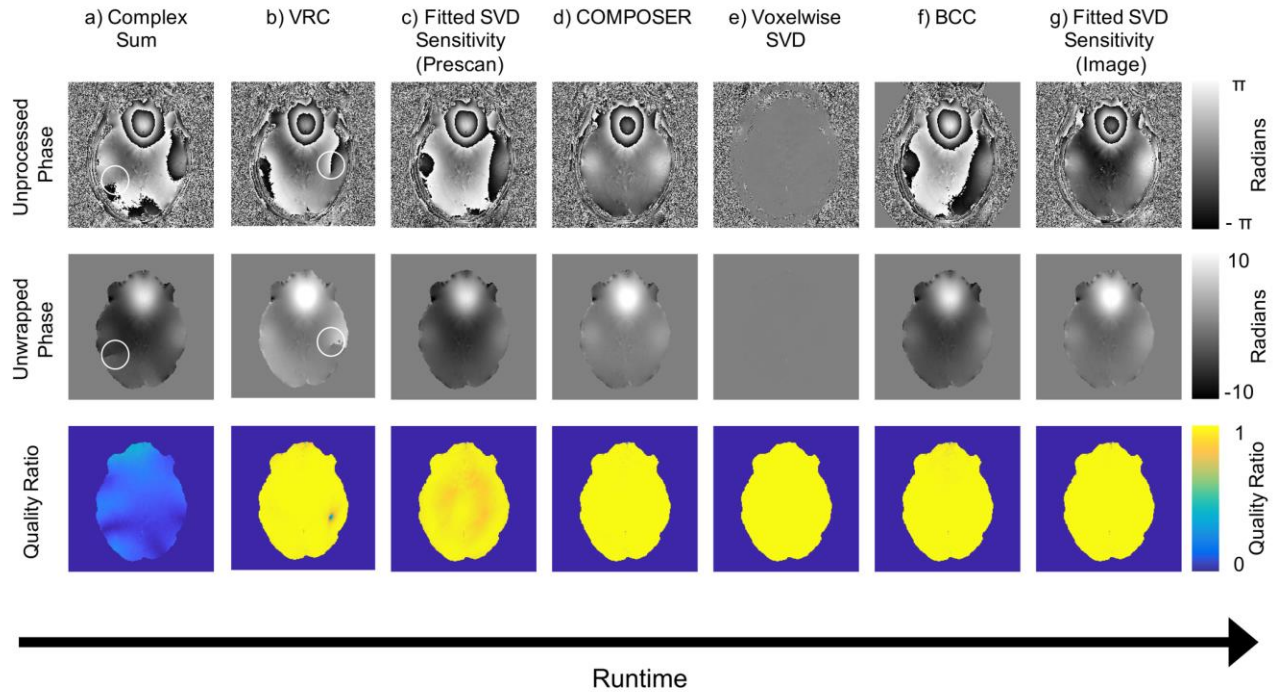
Figure 2.4: Comparison of Phase Combination Methods. One example slice is shown for each method. Top row: raw phase image, Middle row: unwrapped phase image for easier visualization (singularities circled in white), Bottom row: quality ratio across a representative slice. a) Complex sum combination, b) VRC c) Fitted SVD method using a low resolution B_1^+ prescan, d) COMPOSER, e) Voxel-wise SVD combination, f) BCC, g) Fitted SVD method using parameter matched dataset. Single threaded runtime of each method increases left to right and can be found in Table 1. Note: the BCC method applies a rough mask to the region-of-interest during combination and this causes zeros in the exterior of the raw phase image.
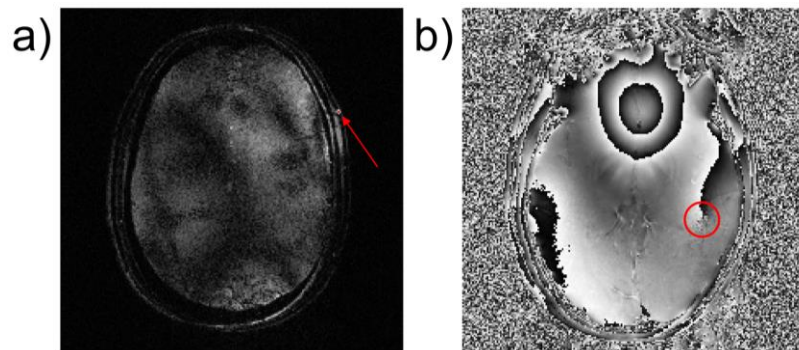
Figure 2.5: VRC Combination. a) Image of the largest minimum magnitude across all coils for VRC reference voxel selection. Voxel is in red and is indicated by a red arrow. b) Virtual reference coil created when using the selected voxel. A singularity is circled in red. This singularity is also present in the combined images and using VRC in this case results in an image with a phase singularity which affects downstream processing.

Phase singularities represent complete signal loss at their location in the image however there can also be subtler SNR decreases throughout the brain. To identify phase SNR decreases it is necessary to compare quality ratio between combination methods (Figure 2.4 and Table 2.1). The fitted SVD method can combine the target image with no loss of phase SNR when matched resolution images are used. In contrast, there was a slight quality degradation (4%) when the lower resolution B_1^+ prescan data was used. This degradation was small compared to the complex sum combination. Although methods such as COMPOSER and BCC show fractionally higher quality ratios, this is offset by substantially larger computational expense which makes using them for large phase datasets impractical.

Table 2.1: Summary of Coil Combination Methods quality and single threaded runtime when implemented in Matlab R2018a. All quality ratio values are calculated over the entire brain mask.

Combination Method	Singularities Present	Quality ratio (mean±std)	Runtime in Matlab (seconds)
Complex Sum	Yes	0.17±0.08	0.09
Virtual Receive Coil	Yes	0.98±0.05	1.2
Fitted SVD Method (Prescan data)	No	0.96±0.04	36
COMPOSER	No	1.00±0.03	137
Voxel-wise SVD	No	1.00±0.00	400
Block coil combination	No	1.00±0.04	2700
Fitted SVD Method (Image data)	No	1.00±0.03	4900

2.3.3   Fitted SVD and the Occipital-Parietal Coil

To investigate potential coil geometry dependency of the fitted SVD method, it was used with an occipital-parietal coil designed for high-resolution imaging of the visual system [29]. The same fit parameters were used from the whole head coil. The

combination shows no degradation in signal in the areas targeted by the coil (Figure 2.6). The quality ratio across the area of interest was 0.95±0.04 when the B_1^+ prescan was used to determine coil sensitivities. As this combination was done without new parameter selection for the occipital-parietal coil, this demonstrates that the solid harmonic fitting is not dominated by RF receiver design and the fitted SVD method can operate even when imaging with an asymmetrical coil.
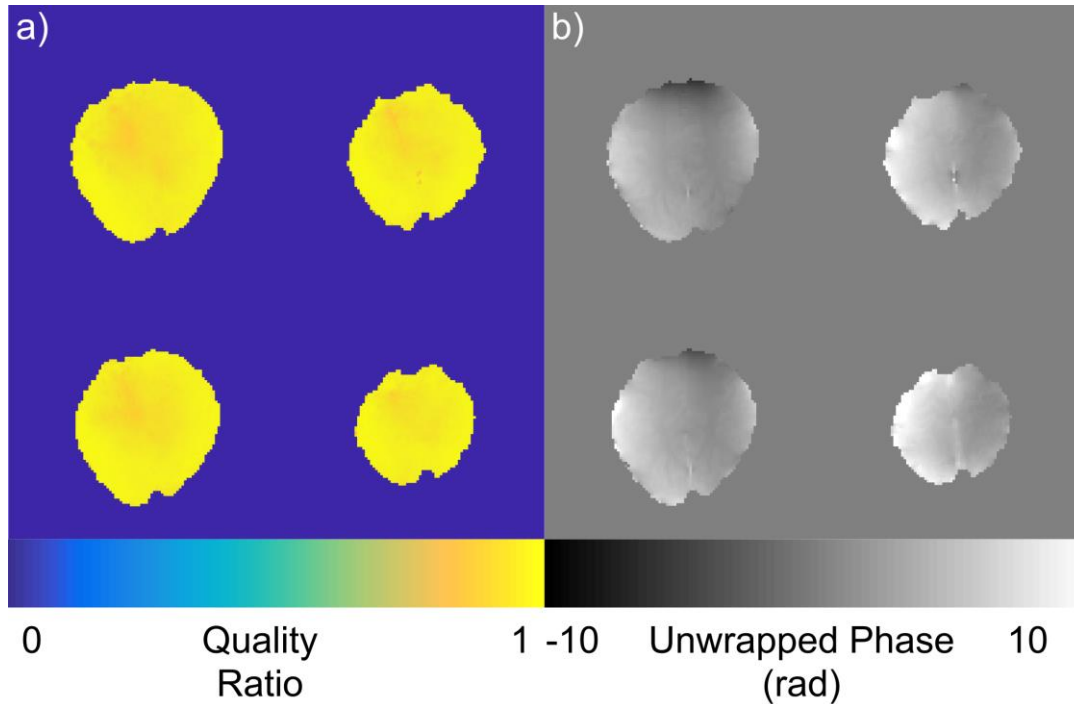
Figure 2.6: Combination quality of an asymmetrical coil. a) Quality ratio of data collected in an occipital parietal coil when combined with the fitted SVD method, b) Spatially unwrapped phase data after fitted SVD combination.

The functional data acquired using the occipital-parietal coil also allowed for investigation of the phase noise over time. This was investigated by calculating the temporal standard deviation of the unwrapped and linearly detrended phase time courses to create phase noise images. The ratios of these phase noise images were then calculated between each combination and, our reference method, the voxel-wise SVD (Figure 2.7). Two combination methods lead to singularities in the combined images when the EPI data was used (Figures 2.7a and 2.7b) and these can be seen in the noise images as hyperintensities. BCC shows elevated phase noise throughout the image (Figure 2.7c).

The phase noise ratio images show that there are no large increases in noise between voxel-wise SVD and the fitted SVD method using a prescan (Figure 2.7d) or a matched image set (Figure 2.7e), demonstrating that for applications such as complex fMRI using the fitted SVD method will not lead to significant additional noise. This is advantageous because using voxel-wise SVD can become expensive when operating on long timeseries or large image sets.
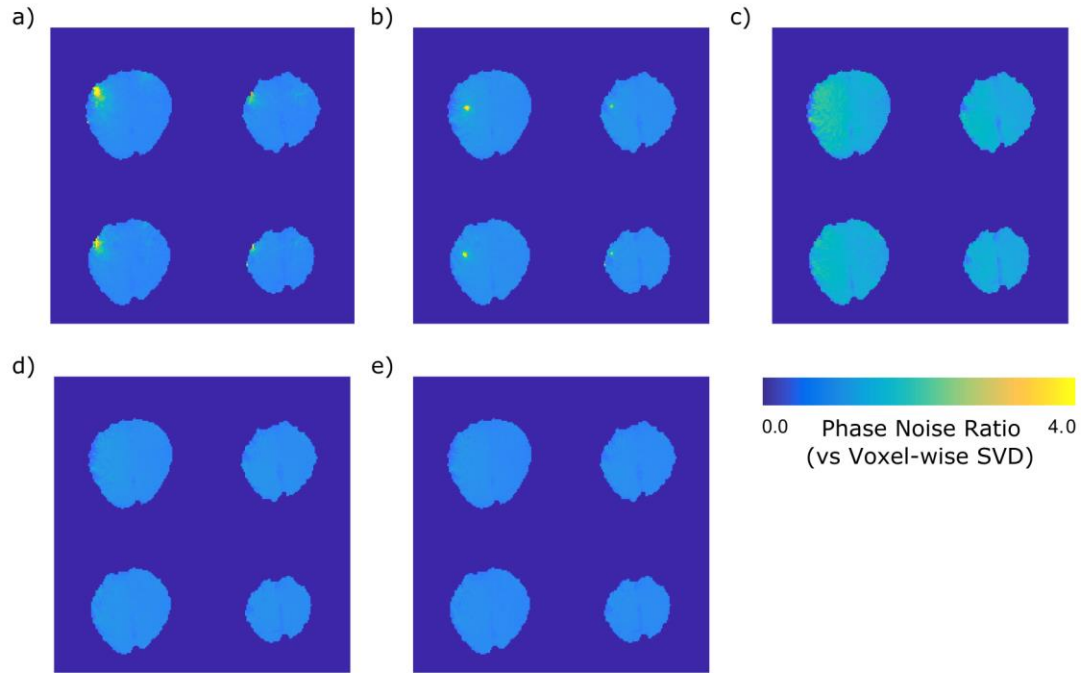
Figure 2.7: Phase noise ratios in an asymmetrical coil. Voxel-wise SVD was used as the reference method. Phase noise ratio combined using a) complex sum, b) VRC, c) BCC, d) the fitted SVD method using the B1+ prescan, and e) the fitted SVD method using the EPI timeseries as input. Hyperintensities correspond with phase singularities in a and b.

2.3.4   Fitted SVD and subject motion

Finally, it is necessary to investigate the fitted SVD method in the case of subject head motion. Subject head motion could slightly change the coil loading and as a result could degrade the quality of the phase combination as the sensitivities change. This limitation is always a concern when using any prescan based approaches, including reference lines for accelerated acquisitions. A B_1^+ prescan and five target GREs were

collected after which the subject was asked to move in the coil and a single GRE and the B_1^+ prescan were collected again. Registration between the first GRE and the reference collected after the subject moved show the subject had a root-mean-squared motion of 3.5 mm, far beyond the tolerance of any functional study and representing a true worst-case scenario with respect to subject motion [33]. The premotion B_1^+ prescan resulted in a quality ratio across the brain of 0.95±0.05. When the prescan collected after large head motion was used the quality ratio remained the same (0.95±0.05). This demonstrates that combination quality is tolerant of significant head motion (Figure 2.8). This is likely due to the smooth spatial frequency characteristics of the solid harmonic fitting and the low resolution prescan.
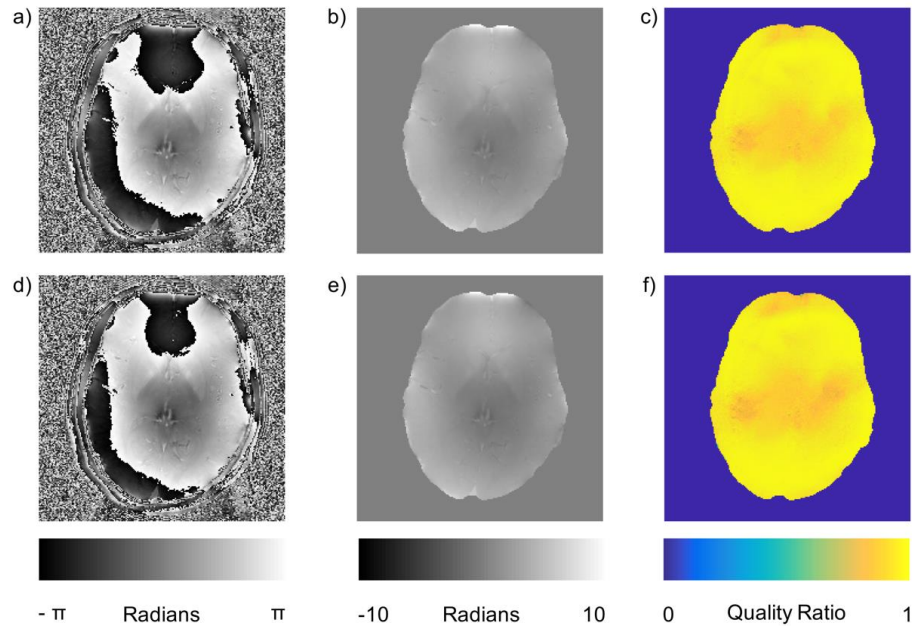
Figure 2.8: Effects of motion on the fitted SVD method. a) Raw phase image, b) unwrapped phase image, c) quality ratio map created with no motion between the $\boldsymbol{B_1^+}$ prescan and the imaging. d) Raw phase image, e) unwrapped phase image, f) quality ratio map created with 3.5 mm motion between the $\boldsymbol{B_1^+}$ prescan and the imaging. No singularities were observed.

2.4   Discussion

Phase imaging requires robust coil combination to be useful. In large multi-volume imaging datasets, such as those acquired for fMRI or fQSM, inline combination becomes vital as the computational load for exporting uncombined data can be prohibitive (hours for a typical fMRI timeseries). The fitted SVD method was created to combine these large imaging sets, though it is equally applicable for all MRI applications. Its implementation will allow for combination of phase data inline, expanding the utility of phase based image processing such as fQSM [9] or phase regression at high resolution [8]. This method is needed as these applications are growing fastest at ultra-high field strengths where the combination issues are most pronounced. The idea of creating a phase combination method tailored to a specific application has already been established in the literature. Several methods have already been established for multi-echo data for QSM such as phase difference methods [34], ASPIRE [35] and voxel-wise SVD combination (Equation 1, [13]). In addition, work has been undertaken to complete a reference free coil combination of water fat imaging [36] and provide a bias free combination for QSM [20]. The proposed fitted SVD method is another such approach to optimizing phase sensitive combination to a specific application, in this case large functional imaging datasets. This method is uniquely suited to processing large datasets in two ways: (1) by creating a combination that could be applied to the data during inline reconstruction and (2) by ensuring the method is robust across coil configurations and motion.

2.4.1   The fitted SVD method will require no export of data off system

In order to avoid export of large uncombined datasets off the MRI system, the coil sensitivities could be quickly estimated using prescans and then applied to a scanning session during inline reconstruction. This is future work. However, in MATLAB testing, the use of a B_1^+ prescan reduced computational runtime by two orders of magnitude compared to using data with parameters matched to the target imaging set. When compared to other combination methods, the fitted SVD method performed faster than

BCC or COMPOSER [17] and had no singularities, like VRC [14] or complex sum (Table 1). These results establish that this method is a suitable trade-off between quality and functionality.

2.4.2 The fitted SVD method is robust across coil configurations and motion

Several features of the fitted SVD method were designed to increase its robustness for routine use. First, the use of a voxel-wise SVD to derive receive coil sensitivities makes the method extensible to any multi-image prescan, including several of the conventionally used shimming prescans. As a result, this method easily fits into existing protocols and produces images with a quality ratio of 0.96±0.04 (mean±std) when using these prescans, as opposed to 1.00±0.03 when using a matched image set. The image created by the default combination on our MRI system results in a quality ratio of 0.17±0.07 across the brain and contains phase singularities (Figure 2.4). Second, use of the minimax algorithm to create a virtual receive coil increases robustness above maximum shared signal selection [14], making this method more robust than VRC. Finally, through fitting the coil sensitivities to a basis, we can extend their utility to scans of various geometries with minimal SNR penalties (Figures 2.2 and 2.6). This fitted SVD method produces a stable combination across time (Figure 2.7) as well as maintains high SNR results in the case of extreme subject motion (Figure 2.8). The solid harmonics can model sensitivities from a coil with symmetrical or asymmetrical geometry to produce high quality ratio images (Figure 2.6). As the solid harmonic solution is a relaxation of the Helmholtz equations, this method should also be able to model coil sensitivities far from the head, where the shapes are non-spheroid [22], although more investigation is required. These factors demonstrate that the fitted SVD method is a robust phase sensitive combination.

2.4.3 Applications of the fitted SVD method for phase combination

This fitted SVD method can be used for any type of imaging and is ideally positioned to combine large multi-volume datasets such as those used in complex valued

fMRI and fQSM. Although the fitted SVD method results in a left right asymmetry this is not due to a reduced quality ratio and can either be corrected using relative phase across time [6] or high pass filtering as is common in QSM [20]. Several other factors make it attractive for phase combination in other applications, including that this method can be applied in absence of a body coil, making it a strong choice in a research environment that uses high B_0 fields where body coils cannot be used to estimate coil sensitivities. Additionally, implementation of the method requires no extra acquisitions in a conventional pTx scanning protocol, due to the use of an existing prescan to derive the receive coil sensitivity estimates. This combination method can be used for all applications free of supervision, as the three parameters governing its operation can be set to be optimal for the specific system (and potentially coil) as needed. In this study, once these parameters were selected, there was no case collected in the three datasets in which the fitted SVD method produced singularities. These factors make the fitted SVD method useful for any ultra-high field system in need of a push button solution, particularly those applications that acquire multivolume phase data.

2.4.4   Study limitations

This preliminary study of the fitted SVD method used datasets targeted at the goal application for analysis. These experiments included our proposed target application, functional phase imaging, and provided estimates of quality as well as temporal noise. Future work could further investigate the efficacy of this technique across a larger subject group to ensure quality in other applications.

The quality of the fitted SVD method does depend on the resolution of the data used to derive coil sensitivities, which becomes a trade-off between quality versus time because the low-resolution nature of the prescan reduces the time required to fit it to the solid harmonics. The fitting will take more time if it is applied to higher resolution data, but this trade-off does not result in a large phase SNR decrease (4%, Figure 2.2). This method is also limited by any motion between the prescan and the imaging session, however the worst-case analysis in our head coil shows that this effect is minimal (Figure 2.8). In fact, the resistance of this method to motion makes it an excellent candidate for

functional imaging. While it may not be suited to every application of phase imaging, it is an excellent option for those that would otherwise be limited in compute resources.

2.5   Conclusions

In conclusion, the fitted SVD method proposed in this pilot study potentially allows for robust phase coherent combination inline and with minimal phase SNR loss. This method is an extension of the existing ESPIRiT, voxel-wise SVD, and VRC combination methods. Using voxel-wise SVD allows us to compute coil sensitivity estimates from routinely acquired prescans without relying on a physical reference coil. Using a minimax optimization to determine our virtual reference coil has removed shared singularities from our sensitivities and ensures a good fit across the region of interest. The solid harmonic fitting allows us to use the power of the voxel-wise SVD combination on a small, acquired dataset and apply that solution to align and combine the entire session for better phase imaging that takes full advantage of conventionally acquired protocols. These different steps allow for stable phase imaging on high throughput systems such as ultra-high field research systems, allowing for phase contrast images to be added without additional scan or compute time.

2.6   References

1.   Rieke V, Butts Pauly K. MR thermometry. J Magn Reson Imaging JMRI. 2008;27: 376–390. doi:10.1002/jmri.21265

2.   Haacke EM, Xu Y, Cheng Y-CN, Reichenbach JR. Susceptibility weighted imaging (SWI). Magn Reson Med. 2004;52: 612–618. doi:10.1002/mrm.20198

3.   de Rochefort L, Brown R, Prince MR, Wang Y. Quantitative MR susceptibility mapping using piece-wise constant regularized inversion of the magnetic field. Magn Reson Med. 2008;60: 1003–1009. doi:10.1002/mrm.21710

4.   Haacke EM, Liu S, Buch S, Zheng W, Wu D, Ye Y. Quantitative susceptibility mapping: current status and future directions. Magn Reson Imaging. 2015;33: 1–25. doi:10.1016/j.mri.2014.09.004

5.   Wigström L, Sjöqvist L, Wranne B. Temporally resolved 3D phase-contrast imaging. Magn Reson Med. 1996;36: 800–803. doi:10.1002/mrm.1910360521

6. Menon RS. Postacquisition suppression of large-vessel BOLD signals in high-resolution fMRI. Magn Reson Med. 2002;47: 1–9. doi:10.1002/mrm.10041

7. Rowe DB, Logan BR. Complex fMRI analysis with unrestricted phase is equivalent to a magnitude-only model. NeuroImage. 2005;24: 603–606. doi:10.1016/j.neuroimage.2004.09.038

8. Stanley OW, Kuurstra AB, Klassen LM, Menon RS, Gati JS. Effects of phase regression on high-resolution functional MRI of the primary visual cortex. NeuroImage. 2021;227: 117631. doi:10.1016/j.neuroimage.2020.117631

9. Balla DZ, Sanchez-Panchuelo RM, Wharton SJ, Hagberg GE, Scheffler K, Francis ST, et al. Functional quantitative susceptibility mapping (fQSM). NeuroImage. 2014;100: 112–124. doi:10.1016/j.neuroimage.2014.06.011

10. Robinson SD, Bredies K, Khabipova D, Dymerska B, Marques JP, Schweser F. An illustrated comparison of processing methods for MR phase imaging and QSM: combining array coil signals and phase unwrapping. NMR Biomed. 2017;30. doi:10.1002/nbm.3601

11. Moeller S, Yacoub E, Olman CA, Auerbach E, Strupp J, Harel N, et al. Multiband multislice GE-EPI at 7 tesla, with 16-fold acceleration using partial parallel imaging with application to high spatial and temporal whole-brain fMRI. Magn Reson Med. 2010;63: 1144–1153. doi:10.1002/mrm.22361

12. Roemer PB, Edelstein WA, Hayes CE, Souza SP, Mueller OM. The NMR phased array. Magn Reson Med. 1990;16: 192–225. doi:10.1002/mrm.1910160203

13. Walsh DO, Gmitro AF, Marcellin MW. Adaptive reconstruction of phased array MR imagery. Magn Reson Med. 2000;43: 682–690. doi:10.1002/(SICI)1522-2594(200005)43:5<682::AID-MRM10>3.0.CO;2-G

14. Parker DL, Payne A, Todd N, Hadley JR. Phase reconstruction from multiple coil data using a virtual reference coil. Magn Reson Med. 2014;72: 563–569. doi:10.1002/mrm.24932

15. Buehrer M, Pruessmann KP, Boesiger P, Kozerke S. Array compression for MRI with large coil arrays. Magn Reson Med. 2007;57: 1131–1139. doi:10.1002/mrm.21237

16. Bilgic B, Marques JP, Wald LL, Setsompop K. Block coil compression for virtual body coil without phase singularities. Proceedings of the 4th International Workshop on MRI Phase Contrast & Quantitative Susceptibility Mapping. Graz, Austria; 2016.

17. Robinson SD, Dymerska B, Bogner W, Barth M, Zaric O, Goluch S, et al. Combining phase images from array coils using a short echo time reference scan (COMPOSER). Magn Reson Med. 2017;77: 318–327. doi:10.1002/mrm.26093

18. Inati SJ, Hansen MS, Kellman P. A Solution to the Phase Problem in Adaptive Coil Combination. Proceedings of the 21st International Society for Magnetic Resonance in Medicine Annual Meeting. Salt Lake City, USA; 2013. Available: http://archive.ismrm.org/2013/2672.html

19. Jenkinson M, Beckmann CF, Behrens TEJ, Woolrich MW, Smith SM. FSL. NeuroImage. 2012;62: 782–790. doi:10.1016/j.neuroimage.2011.09.015

20. Bollmann S, Robinson SD, O'Brien K, Vegh V, Janke A, Marstaller L, et al. The challenge of bias-free coil combination for quantitative susceptibility mapping at ultra-high field. Magn Reson Med. 2018;79: 97–107. doi:10.1002/mrm.26644

21. Uecker M, Lai P, Murphy MJ, Virtue P, Elad M, Pauly JM, et al. ESPIRiT — An Eigenvalue Approach to Autocalibrating Parallel MRI: Where SENSE meets GRAPPA. Magn Reson Med Off J Soc Magn Reson Med Soc Magn Reson Med. 2014;71: 990–1001. doi:10.1002/mrm.24751

22. Sbrizzi A, Hoogduin H, Lagendijk JJ, Luijten P, van den Berg CAT. Robust reconstruction of B1 (+) maps by projection into a spherical functions space. Magn Reson Med. 2014;71: 394–401. doi:10.1002/mrm.24640

23. Katscher U, Berg CAT van den. Electric properties tomography: Biochemical, physical and technical background, evaluation and clinical applications. NMR Biomed. 2017;30: e3729. doi:10.1002/nbm.3729

24. Eckart C, Young G. The approximation of one matrix by another of lower rank. Psychometrika. 1936;1: 211–218. doi:10.1007/BF02288367

25. Özbay PS, Deistung A, Feng X, Nanz D, Reichenbach JR, Schweser F. A comprehensive numerical analysis of background phase correction with V-SHARP. NMR Biomed. 2017;30. doi:10.1002/nbm.3550

26. Gilbert KM, Gati JS, Kho E, Martyn Klassen L, Zeman P, Menon RS. An parallel-transmit, parallel-receive coil for routine scanning on a 7T head-only scanner. Proceedings of the 23rd International Society for Magnetic Resonance in Medicine Annual Meeting. Toronto, CA; 2015.

27. Yarnykh VL. Actual flip-angle imaging in the pulsed steady state: a method for rapid three-dimensional mapping of the transmitted radiofrequency field. Magn Reson Med. 2007;57: 192–200. doi:10.1002/mrm.21120

28. Curtis AT, Gilbert KM, Klassen LM, Gati JS, Menon RS. Slice-by-slice B1+ shimming at 7 T. Magn Reson Med. 2012;68: 1109–1116. doi:10.1002/mrm.23319

29. Gilbert KM, Gati JS, Menon RS. Occipital-Parietal Coil with variable-density element distribution for 7T functional imaging. Proceedings of the 25th International Society for Magnetic Resonance in Medicine Annual Meeting. Honolulu, USA; 2017.

30. Gilbert KM, Klassen LM, Mashkovtsev A, Zeman P, Menon RS, Gati JS. Radiofrequency coil for routine ultra-high-field imaging with an unobstructed visual field. NMR Biomed. 2021;34: e4457. doi:10.1002/nbm.4457

31. Abdul-Rahman HS, Gdeisat MA, Burton DR, Lalor MJ, Lilley F, Moore CJ. Fast and robust three-dimensional best path phase unwrapping algorithm. Appl Opt. 2007;46: 6623–6635. doi:10.1364/ao.46.006623

32. Haacke EM, Brown RW, Thompson MR, Venkatesan R, Others. Magnetic resonance imaging: physical principles and sequence design. Wiley-Liss New York:; 1999.

33. Power JD, Mitra A, Laumann TO, Snyder AZ, Schlaggar BL, Petersen SE. Methods to detect, characterize, and remove motion artifact in resting state fMRI. NeuroImage. 2014;84: 320–341. doi:10.1016/j.neuroimage.2013.08.048

34. Bernstein MA, Grgic M, Brosnan TJ, Pelc NJ. Reconstructions of phase contrast, phased array multicoil data. Magn Reson Med. 1994;32: 330–334. doi:10.1002/mrm.1910320308

35. Eckstein K, Dymerska B, Bachrata B, Bogner W, Poljanc K, Trattnig S, et al. Computationally Efficient Combination of Multi-channel Phase Data From Multi-echo Acquisitions (ASPIRE). Magn Reson Med. 2018;79: 2996–3006. doi:10.1002/mrm.26963

36. Liu S, Wu P, Liu H, Hu Z, Guo H. Referenceless multi-channel signal combination: A demonstration in chemical-shift-encoded water-fat imaging. Magn Reson Med. 2020;83: 1810–1824. doi:10.1002/mrm.28028

3 Effects of Phase Regression on High-Resolution Functional MRI of the Primary Visual Cortex

This study investigated the efficacy of phase regression at high-resolution to determine its utility in laminar fMRI. Phase regression was applied to GE-EPI timeseries and compared to SE-EPI to determine if GE-EPI's specificity to the microvascular compartment improved. To do this, functional data was collected from seven human subjects at 800 μm isotropic resolution. Phase data from the GE-EPI was used to create a microvasculature-weighted time series (GE-EPI-PR). The GE-EPI-PR surface activation maps showed a high qualitative similarity with SE-EPI and produced laminar activity profiles similar to SE-EPI. Furthermore, it was shown that GE-EPI-PR has a higher contrast-to-noise ratio than SE-EPI demonstrating the technique has higher sensitivity than SE-EPI. Taken together this evidence suggests phase regression is a useful method for macrovascular signal reduction in high-resolution fMRI.

3.1 Introduction

The human cortex is organized into functionally distinct layers parallel to the pial surface and, in select areas, columns perpendicular to the surface. Cortical layers and columns are key functional units in understanding how the brain is organized. Similarly positioned layers perform similar tasks across different parts of the brain [1]. Specifically, the neuronal inputs and outputs are contained in different cortical layers. Measurement of interactions between cortical features such as these could allow for a deeper understanding of intra-cortical and inter-cortical communication. Historically, investigating the function of these small structures required invasive electrophysiology techniques of single and multi-cell recordings in human or animal models [2,3].

More recently, ultra-high field MRI has afforded investigation of brain function at high-resolution through increased signal-to-noise ratio (SNR) and sensitivity to blood oxygenation. High-resolution fMRI using various methods in healthy human subjects has shown agreement with previously published electrophysiological results from animals [4]. This agreement supports the use of high-resolution fMRI as a neuroscience tool. This technique has been used to investigate the organization of cortical layers [5–9] and columns [10–13] across the human brain.

High-resolution fMRI using blood oxygenation level dependent (BOLD) contrast struggles with various acquisition challenges that require consideration prior to data collection. These include lower SNR as resolution increases, macrovascular bias, and specific absorption rate (SAR) constraints at ultra-high fields. Several different acquisition approaches have been used to perform high-resolution fMRI although the two most commonly used are gradient echo EPI (GE-EPI) and spin echo EPI (SE-EPI). Conventional GE-EPI produces the largest signal changes but is not specific to microvasculature [14–18]. Unlike GE-EPI, SE-EPI is more specific due to the use of a refocusing pulse to suppress the macrovascular signal. Unfortunately, this sequence suffers from SNR and SAR penalties making it a less sensitive technique overall. Comparisons between the sensitivity and specificity of these techniques shows that GE-EPI has 1.29 times higher percent signal change in grey matter than SE-EPI and 5.33 times higher percent signal change in vessels at 7T [19]. These advantages have made GE-EPI the overwhelming choice for high resolution fMRI studies.

Several alternatives to GE-EPI and SE-EPI have been investigated such as vascular space occupancy (VASO) [20,21], balanced steady state free procession (bSSFP) [22] and gradient and spin-echo imaging (GRASE) [13,23]. VASO focuses on imaging changes in cerebral blood volume which results in more specificity to the microvasculature [21]. bSSFP shows T_2-like weighting and SNR efficiency but is limited to a small slab to avoid excessively long acquisition times. GRASE reduces macrovascular signal by placing refocusing pulses throughout a GE-EPI sequence which lowers T_2^* weighting [23] but also limits coverage to a specific region of interest to avoid

reintroducing these T_2^* effects. However, GE-EPI remains the most commonly used fMRI technique today due to its robustness and well understood signal properties.

Previous work by many groups has attempted to reduce the vascular bias from high-resolution GE-EPI while maintaining sensitivity. These methods include optical imaging to identify larger vessels [24], susceptibility weighted imaging to identify veins [9,25], removing venous bias through deconvolution with a vascular PSF [26], looking at the initial dip of the BOLD response [27], contrast subtraction [10,28] and removing the higher cortical layers where such veins are present from further analysis [29]. These techniques all rely on knowledge and/or assumptions of the vein's locations in the GE-EPI images which can require additional acquisitions or signal modelling, and this can complicate their use in high resolution fMRI. Another very recent approach that utilizes the temporal lag between microvascular BOLD signals and macrovascular BOLD signals shows promise in an initial report [30].

This paper proposes the use of the phase of the high-resolution GE-EPI images to estimate BOLD signal caused by large vessels and subtract it from the magnitude data. This data-driven method reduces macrovascular bias without using additional venous identification. fMRI phase is an intrinsic part of a conventional GE-EPI acquisition but is usually not reconstructed and saved as part of the fMRI pipeline. Phase regression has previously been used at low resolutions to reduce large vessel contributions in the magnitude images [31–34]. This technique relies on the fact that although magnitude signal will contain BOLD changes from both large and small vasculature, phase data will primarily contain BOLD changes from large vessels [34].

Some discussion of what constitutes a large vessel with respect to this technique is necessary. Cortical veins can be divided into three groups: pial veins (>280 μm), run along the cortical surface; intracortical penetrating veins (80-170 μm), run perpendicular to the cortical surface; and smaller intracortical tangential veins, which run at different depths parallel to the layers of the cortex [35]. For the current experiments, it is unlikely that useful phase information can be obtained from vessels smaller than 150 μm in diameter [36]. Additionally, all phase related BOLD changes will increase in amplitude

as the vessel size increases [37] so larger vessels will dominate the phase time course. Thus, for the purposes of this paper we define the macrovasculature as vessels large enough to produce a detectable BOLD phase change, which will primarily be pial vessels and a few of the largest intracortical veins.

At low resolutions, BOLD related phase changes are primarily due to the intravascular BOLD signal [34,37]. The extravascular phase signal for the macrovasculature will be negligible at low resolutions due to the symmetric extravascular frequency profile. Therefore, it can be assumed any voxel with a high correlation between magnitude and phase contains signal from the intravascular component of macrovasculature. This assumption has yet to be tested in voxels near the size of pial vessels on the cortical surface which this paper seeks to investigate. Extravascular frequency shifts could produce a phase change in a sufficiently small voxel when the symmetry assumption is violated [38]. This would result in phase changes and suppression of extravascular and intravascular BOLD signal, improving the reduction in macrovascular bias for high resolution data.

This paper investigates phase regression of high-resolution GE-EPI functional time series data as a method to reduce macrovascular bias. Laminar structures are evaluated in GE-EPI and SE-EPI functional acquisitions and compared with GE-EPI-PR (GE-EPI with phase regression) data. This paper examines the surface activation maps of the GE-EPI, SE-EPI and GE-EPI-PR as well as their activation distributions and contrast-to-noise ratio (CNR). Furthermore, the laminar profiles of GE-EPI, SE-EPI and GE-EPI-PR are compared to determine the effect of phase regression on the laminar profile proximal to and distal from a vessel.

3.2   Methods

3.2.1   Data Acquisition

Imaging Protocol

Data from seven subjects was acquired (5 male, 2 female, 25.8 ± 4.0 years). Each individual was positioned supine on the MRI bed with a mirror placed over the eyes for viewing a rear-projection screen 28-cm away producing a left-right visual angle of 27.5 degrees. Foam cushions were placed around the head for comfort and immobilization as well as medical tape across the forehead for haptic feedback to reduce motion. Informed consent of all participants was collected in accordance with and approved by the Human Subjects Research Ethics Board at the University of Western Ontario.

Imaging was performed using a 680 mm neuro-optimized 7 T MRI (Siemens Magnetom Step 2.3, Erlangen, Germany) equipped with an AC84 Mark II head gradient coil. An 8-channel Tx, 32-channel Rx radiofrequency coil optimized for occipital-parietal imaging with no visual obstruction over the face was chosen for data collection [39]. The actual flip-angle imaging (AFI) technique [40], augmented with an RF and gradient spoiling scheme [41], was used to map the transmit field. In addition, 8 images with Fourier B_1^+ encoding were acquired to map relative transmit profiles. RF shimming was subsequently performed, which consisted of setting the phase and magnitude of each transmit channel using a least-squares optimization that balanced transmit efficiency and uniformity [42]. The B_1^+ shim solution was optimized over the region of interest relevant to the BOLD measurements. To ensure phase was not inappropriately filtered zero-filling partial Fourier was used. The scanning protocol consisted of GE-EPI, SE-EPI, a multi-echo gradient echo sequence for venous localization and an MP2RAGE sequence with high gray-white contrast to extract functional surfaces. Parameters for all imaging sequences can be found in Table 3.1.

Table 3.1: Imaging Parameters

Sequence	Resolution (mm)	Matrix Size	Slice Spacing	TE (ms)	TR (ms)	FA (deg)	BW (Hz/Px)	Acceleration	Notes
Actual Flip Angle Imaging	8x8x8	32x32x32	0%	2.75	20	70	1002	none	
Relative B_1^+ images	8x8x8	32x32x32	0%	2.75	6	70	1002	none	8 images were collected with fourier-encoding to provide relative B_1^+ contrast [42]
Gradient Echo-EPI	0.8x0.8x0.8	240x238x29	10%	23	2500	60	1488	GRAPPA 3, Partial Fourier 6/8	FWHM of the magnitude of the complex PSF in PE 1.35mm
Spin Echo-EPI	0.8x0.8x0.8	240x240x25	10%	41	2500	90	1488	GRAPPA 3, Partial Fourier 6/8	FWHM of the magnitude of the complex PSF in PE 1.54mm
Multi-Echo GRE	0.31x0.31x0.8	620x542x32	0%	See note	40	9	202	GRAPPA 2	TE=5.82,11.68,17.54,23.4ms
MP2RAGE	0.75x0.75x0.75	214x214x128	0%	2.4	6000	4	180	GRAPPA 3	Inversion times 800ms and 2700ms

Phase reconstruction of the GE-EPI data was completed using the fitted SVD method [43] described in Chapter 2 to prevent destructive interference. Coil sensitivity estimates are obtained by utilizing the multi-image prescan collected for B_1^+ mapping and performing a singular value decomposition. These estimates are fit to a functional basis to allow for their interpolation to other fields of view during the imaging session. The fitted SVD derived coil sensitivities are multiplied with the uncombined coil data to align it prior to a complex sum. This multiplication and complex sum were completed as part of the Siemens reconstruction chain of the CMRR multiband sequence through insertion of a custom functor. Maxwell correction is turned off to prevent any spatial translation differences between the magnitude and phase images after combination. This method of combination is memory efficient due to the low resolution prescan and through the use of custom functors during the normal Siemens reconstruction pipeline; typically, a few hundred megabytes. For non-Siemens sites, phase combination can use the fitted SVD method or additional methods such as COMPOSER [44,45], the virtual reference coil method [46] or the voxelwise SVD method [47]. We recommend an online combination for computational efficiency when dealing with large datasets [48]. A sum-of squares combination from all Rx channels was used to reconstruct the magnitude data.

The magnitude of the complex point spread function of the EPI acquisitions was calculated for the phase encode direction, by simulating a real uniform EPI echo train in k-space to estimate the effective image resolution (Table 1). The effects of acceleration were applied, lines were skipped from GRAPPA, T_2^* and/or T_2 signal decay added, and the echo was zero filled consistent with the partial Fourier technique used during acquisition. The phase encode profile was inverse Fourier transformed and the full width half maximum of the magnitude was measured and reported as the point spread function (PSF) of each EPI sequence. The protocols for the SE-EPI and GE-EPI acquisitions were matched as closely as possible resulting in the SE-EPI having a slightly wider PSF than the GE-EPI. This estimate was performed to compare the two EPI acquisitions and may not be entirely representative of the true resolution [49].

Functional Stimulus

The visual stimulus was an 8 Hz contrast reversing checkerboard created using Pyschtoolbox (3.0.11) in Matlab (2015a). This was delivered in a rest-activation paradigm of 15 seconds off, 15 seconds on lasting for 8 repetitions and ending on a rest block. To help maintain attention, a button press task was used where participants were asked to respond when a central fixation cross changed orientation by 45 degrees. Three runs were acquired for each participant and for each sequence type: GE-EPI and SE-EPI.

3.2.2   Data Preprocessing

Data Analysis Software

All imaging data was converted to the brain imaging data structure (BIDS) format using in-house conversion tools wrapped around heudiconv (Heuristic Dicom Conversion). Analysis was completed using Nipype pipelines (1.1.8 [50]) including several custom interfaces for phase analysis. The in-house software used can be found at: https://github.com/ostanley/phaseprep. An overview of reconstruction and preprocessing is available in Figure 3.1.

On MRI System

- Uncombined low resolution multi-image dataset → Voxelwise SVD → Relative Coil Sensitivities → Iterative Fit onto functional basis
- Fitted Coil Sensitivities
- Uncombined complex data, unaliased and in image space → Alignment using multiplication → Complex Sum → Combined Phase Image
- Sum-of-squares combination → Combined Magnitude Image

Uncombined Target Dataset

Preprocessing

- Motion correct
- Raw magnitude image
- Motion parameters
- Convert to radians → Convert to real and imaginary → Apply motion correction to complex data → Convert to phase → Temporally unwrap and subtract phase of first volume → Linearly Detrend → Apply brain extraction → Preprocessed Phase Data
- Linearly Detrend → Brain Extract → Brain mask → Preprocessed Magnitude Data

Figure 3.1: Overview of reconstruction and preprocessing prior to phase regression.

Functional Data Preprocessing

Both GE-EPI and SE-EPI underwent the same magnitude preprocessing. Each functional imaging run (GE-EPI or SE-EPI) was motion corrected and aligned to the first volume of the first run using AFNI (18.1.24 [51]). Brain extraction was completed on the same first functional volume using FSL's BET tool and the mask was applied to all functional runs (FSL version 5.0.10). The preprocessed magnitude data was then used as the magnitude input for phase regression. After phase regression but prior to general

linear modelling all data was scaled to a mean of 10000 and high pass filtered with a window of 100 seconds (identical to conventional FSL FEAT preprocessing [52]).

Preprocessing of the phase data was performed using the in-house Nipype workflow, *preproc_phase_wf.py*. The workflow consists of conversion of the magnitude and phase data to real and imaginary. Motion correction was performed in real and imaginary space since it is spatially smooth and interpolatable. The transformations from the magnitude images were applied to the real and imaginary data and then converted back to magnitude and phase images. The phase data was further processed by performing first volume subtraction, temporal unwrapping, and linear detrending. Voxelwise detrending was performed to remove systematic linear frequency drift and B_0 field variations over time. The result was a motion corrected phase timeseries, free of temporal and spatial wraps which also accounts for linear system and B_0 field variation.

Phase regression

Previous work on phase regression has shown BOLD related phase changes will correlate with an associated BOLD related change in magnitude and this can be used to estimate signal originating from macrovasculature [34]. This estimated signal can then be subtracted from the magnitude signal to reduce signal from large vessels. This method relies on two assumptions: (1) the temporal correlation of magnitude and phase is different in the microvasculature than in macrovasculature, which prevents complete suppression of the tissue signal in a voxel with a large vessel [53], (2) that all large vessels produce a phase change, which may not be true for vessels at certain orientations [37].

Phase regression was performed using voxelwise orthogonal distance regression (ODR) in the in-house Nipype gadget, *PhaseFitODR.py* [32]. ODR uses residuals perpendicular to the line of best fit and was selected due to the noise present in both magnitude and phase data. The regression was completed to solve the following equation:

$$M = A\varphi + B \tag{3.2.1}$$

where M is the magnitude signal, φ is the phase signal and A and B are the fit coefficients. ODR requires inputs to estimate error ellipses prior to fitting. In order to estimate these errors for magnitude and phase, each time course is high pass filtered at 0.15 Hz (above the task frequency). The temporal standard deviation of these filtered signals was then used as the inputs to the ODR for uncertainties and the unfiltered signals are used as input to the fits. ODR is then used to estimate the component of the signal with high magnitude and phase correlation which is assumed to be macrovascular signal. Subtraction of this estimated macrovascular signal results in a signal weighted towards microvasculature (M_{micro} or GE-EPI-PR):

$$M_{micro} = M - (A\varphi + B) \tag{3.2.2}$$

The effect of this on the timeseries of both a tissue and venous voxel is shown in Figure 3.2. Both the estimated macrovasculature and GE-EPI-PR timeseries underwent the same preprocessing steps as the GE-EPI and SE-EPI time courses (scaling to 10000 and high-pass filtering with a filter window of 100 seconds).
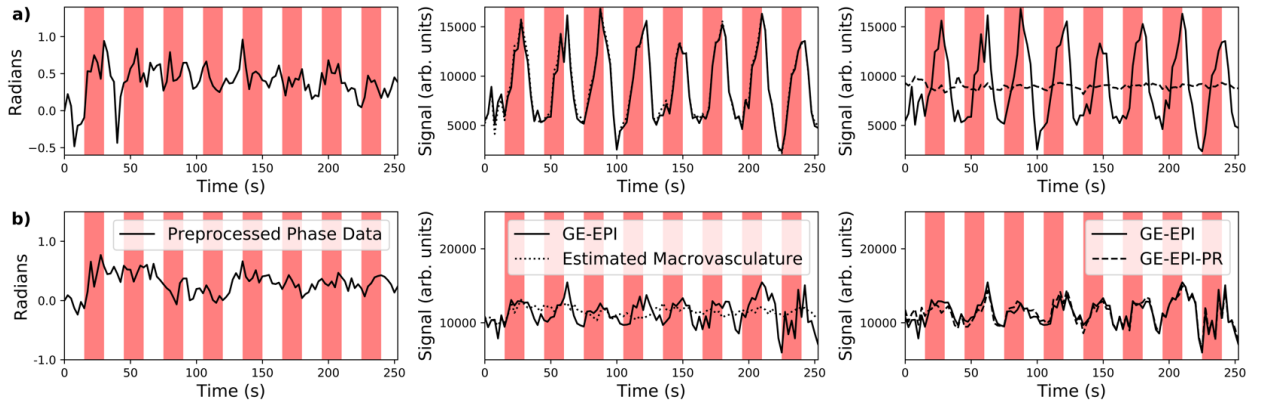
Figure 3.2: Time series for example voxels. (a) a voxel containing a visible vein and (b) a voxel with no visible vein. Left column: preprocessed phase time course, Middle column: the preprocessed magnitude time course and the estimated macrovascular time course and, Right column: the preprocessed magnitude time course as well as the GE-EPI-PR time course. Red indicates a stimulus-on period.

Functional Data Fitting

In order to perform physiological noise correction, regressors were created using anatomical Compcor [54] from each subject's eroded white matter mask transformed to native EPI space. Compcor masks were generated with two erosions in *fslmaths* using a 3x3x3 kernel. Six compcor regressors and the six motion regressors were included as regressors of no interest in the GLM to account for noise caused by physiology and/or motion. All four time series (GE-EPI, SE-EPI, GE-EPI-PR, and the estimated macrovascular timeseries) were analyzed using the FSL *film_gls* tool. The output was converted to % BOLD signal change through normalization to the mean intensity of the timeseries. CNR was calculated by dividing the amplitude of the fit signal by the standard deviation of the residuals [55].

Structural Image Analysis

The MP2RAGE image was run through the Freesurfer high resolution *recon-all* pipeline to create cortical surfaces with two modifications (6.0.0 [56,57]). First, the Talairach registration was turned off as the structural image was limited to the posterior part of the brain (-*notalariach*, due to coil construction). Second, the corpus collosum and pons were manually seeded to ensure proper initialization. The cortical segmentations were manually inspected for agreement with the borders in the region of interest and brain mask corrections were performed, if necessary. The white matter surfaces were equidistantly expanded to allow for depth analysis using Freesurfer's *mris_expand* tool [25]. All results were calculated at 10% cortical depth intervals from 0 (pial surface) to 100% (white matter surface). This does not represent the expected anatomical distribution of the cortical layers but allows for investigation across surfaces and depths. All results were presented across the flattened surfaces by sampling voxel results onto the vertices that make up the surface at each depth.

To restrict analysis to a reasonable area an occipital patch was cut from the rest of the cortex and flattened using Freesurfer's *mris_flatten* tool. A patch over the calcarine sulcus was selected by manual delineation from the white matter curvature and the field of view of all acquisitions projected onto the occipital flat patch (Figure 3.3). This

selected patch is expected to be within primary visual area V1, but more importantly this cortical patch would contain a variety of activation levels and contain vessels required for this investigation. This area was 1000 ± 300 mm^2 per subject leading to on average 1600 voxels analyzed for each hemisphere's surface patch.
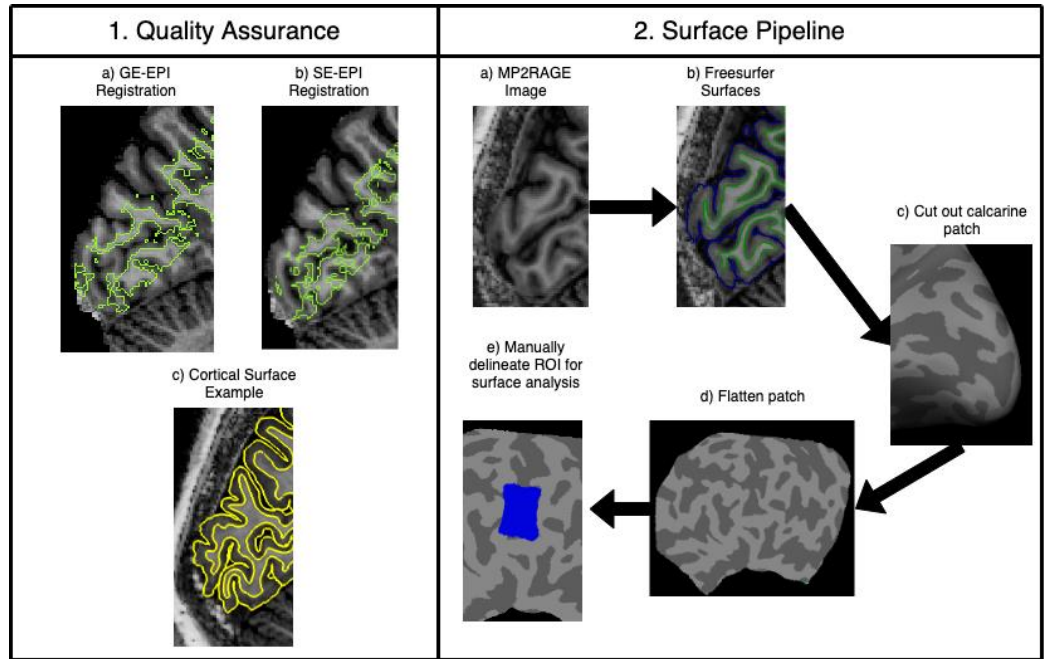
Figure 3.3: Visual demonstration of the surface pipeline. 1: Quality assurance figures for registration and segmentation. FSL Fast segmentation of a) GE-EPI and b) SE-EPI overlaid on the T1weighted MP2RAGE image, c) Freesurfer surfaces overlaid on the T1weighted MP2RAGE image. 2: Surface processing pipeline. First the MP2RAGE is used to generate surfaces (a). From the generated surfaces (b) a calcarine patch is extracted (c) and flattened (d). The ROI (blue area) for analysis is then manually delineated using *tksurfer* and the curvature map as well as slice coverage from the functional scans (e).

Venous Maps

As a simple, robust method for identifying venous vasculature, the product of R_2^* and the initial magnetization (M_0) from multi-echo susceptibility weighted imaging was used. This was done because R_2^* is a physical value and is therefore expected to be consistent across subjects except for the presence of a low frequency background field [58]. In addition, M_0 can be calculated from the same fit and does not require free parameters. In order to calculate these parameters, the multi-echo GRE data was run

through the *qsm_sstv* pipeline (https://github.com/AlanKuurstra/qsm_sstv/releases, 1.0.0). Briefly, this BIDS app extracted the brain from the multi-echo data and performed complex fitting to calculate R_2^*, frequency, and M_0. These maps were then registered to the T_1 image using the same methods as the EPIs (described below) to transfer them to surface space for functional analysis.

Registration to Structural Data

Registration of the functional maps to structural space was completed using ANTs (2.2.0 [59]). After initialization using the center of mass, a rigid transform was completed followed by two affine transformations, one general and one targeted at the region of interest. Mutual information was used as the target metric and all interpolation was completed using order 3 splines. In most laminar studies it is common to bring the anatomic surfaces into functional space. This was not done in this study due to the different fields of view of the GE-EPI and SE-EPI. As an alternative all transformations prior to the GLM were kept to a minimum (one spatial transform per volume) and then performed one single transform of each result to T_1 space. These results were then transferred onto the cortical surface ROI using *mri_vol2surf* and allowed for surface comparison between both pulse sequences. The T_1 transform and sampling to surface space will result in some effective blurring of the data, however these effects are minimized by performing phase regression and GLMs prior to transformation.

3.2.3 Analysis Methods

Surface Visualization

Surface activation maps become distorted during flattening resulting in uneven vertex placement across flat space. The vertices for each layer were converted to a three-dimensional mesh and the laminar surface activation maps were plotted as a triangular mesh in order to reduce this effect. By doing so, it becomes easier to view as it does not involve varying amounts of dead space. The effect this has on visualization is displayed in Figure 3.4. All laminar profiles and signal distributions were calculated across vertices and did not use an interpolation.
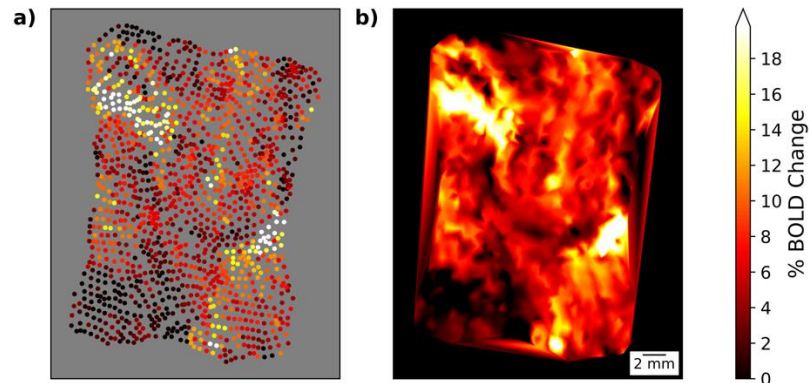
Figure 3.4: Surface visualization demonstration. a) The vertices for a cortical patch plotted over a grey background (used to calculate all laminar profiles and distributions). b) A triangular mesh to make the data more contiguous and easier to visualize when examining surface activation maps qualitatively.

Vessel Segmentation

Manual segmentation was performed in order to delineate visible vessels from tissue. The product of the R_2^* and M_0 surface maps was selected for manual segmentation as it showed reduced noise compared to the R_2^* surface map. Each laminar surface map was manually segmented for every subject and every cortical depth. Hyperintensities were outlined as polygons on top of the mesh using matplotlib. All vertices in these hyperintense region polygons were then labelled as vessels. To control for bias, no indication of cortical depth or subject was given when each map was presented, each map was presented with an identical colour bar, and the maps were presented in randomized order. After manual segmentation was completed, two forms of continuity clustering were used. First, vertices which were labelled as a vessel across two adjacent depths were included in the final vessel map to include penetrating vessels. Second, marked vertices greater than 0.3 mm away from another marked vertex were excluded, this provides for the possibility of a vessel running along the surface of a single layer. These thresholds were both applied to improve vessel continuity and reduce the presence of single noisy vertices causing mislabeling. An overview of this process can be seen in Figure 3.5.
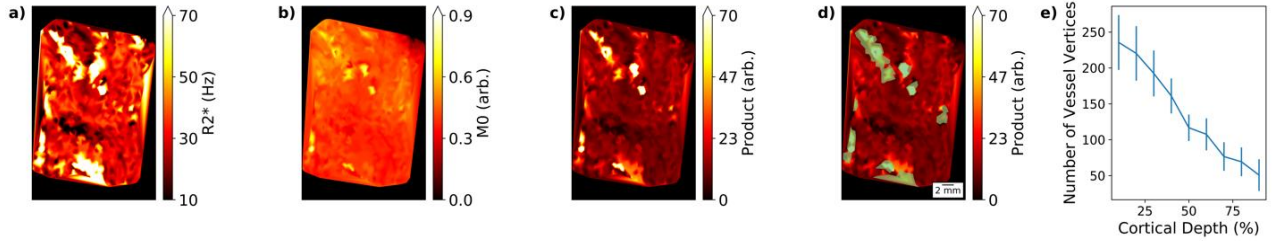
Figure 3.5: Vessel segmentation overview. All patches are presented at 10% cortical depth. a) R_2^* map, b) M_0 map, c) the product of the R_2^* and M_0 maps from an example subject. d) Areas identified as vessels after both manual segmentation and continuity correction are shown in green over the product map. e) Average count of vessel vertices across subjects as a function of cortical depth. Error bars represent the standard error of the mean.

Laminar Profile Generation

Laminar profiles were plotted by averaging across all vertices in the calcarine patch of interest for each of the nine depths from 10% to 90%. Vertices were also classified as proximal to or distal from a vessel based on their minimum Euclidean distance to a vessel vertex thresholded at 2.4 mm. At this distance, an activation based frequency shift of 24Hz is expected, compared to 220Hz at the surface of a 0.8 mm vessel (calculated from [38]). This was considered sufficiently out of the influence of large veins for this study.

3.3   Results

The temporal SNR in the field of view of interest is uniform (Figure 3.6). A poor B_1^+ shim in one subject's hemisphere was observed and verified on the actual flip angle map. This hemisphere was excluded from the group metrics reported below and from all further analysis. Temporal SNR across the cortical ribbon of all subjects was 10.2 ± 1.2 (mean $\pm$ standard deviation) for the GE-EPI and 8.36 ± 0.83 for the SE-EPI data. The tSNR of the GE-EPI and SE-EPI was significantly different in a Welch's t-test (p=0.015) and this is an important note for later surface activation map comparison. Finally, the phase standard deviation of the timeseries was 0.21 ± 0.12 radians across all subjects.
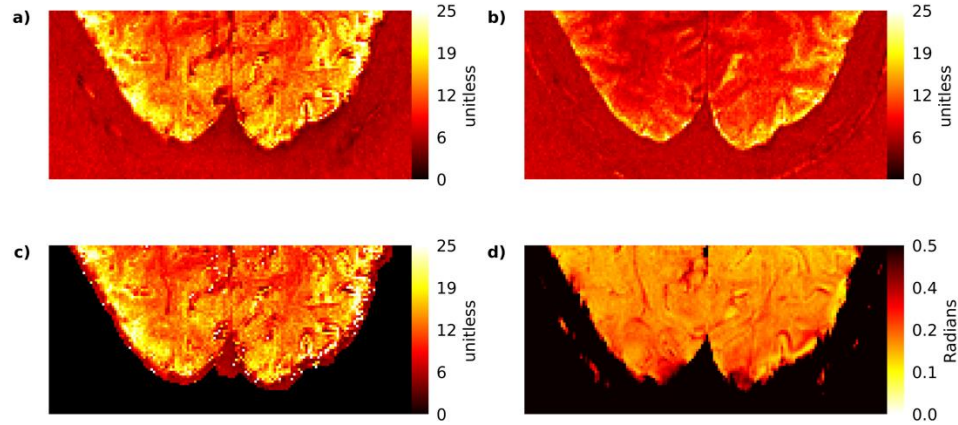
Figure 3.6: Volumetric Data Quality Example. Temporal signal-to-noise ratio maps for an example subject. a) GE-EPI, b) SE-EPI, c) GE-EPI-PR, d) Phase temporal standard deviation for the same subject.

To investigate the changes in the laminar surface activation maps due to phase regression the BOLD % signal change was projected onto surfaces at various cortical depths (an example subject is shown in Figure 3.7). The equidistantly projected data shows surface veins that are clearly visible in the higher layers of cortex (towards the pial surface). This is to be expected, even in the SE-EPI case as the purely T_2 weighting only applies for the central measurement of k-space. The lower tSNR in the SE-EPI does affect the laminar surface activation maps as they appear noisier, but it is still clearly less sensitive to large vessels. The hyperintense venous regions in the GE-EPI data exhibit the largest signal suppression after phase regression compared to surrounding areas. The spatial distribution of GE-EPI-PR appears to match the SE-EPI case more closely. To validate the areas of high activation in the GE-EPI are truly large vessels the data was examined in conjunction with the structurally derived, vessel sensitive R_2^* and M_0 data (Figure 3.8).
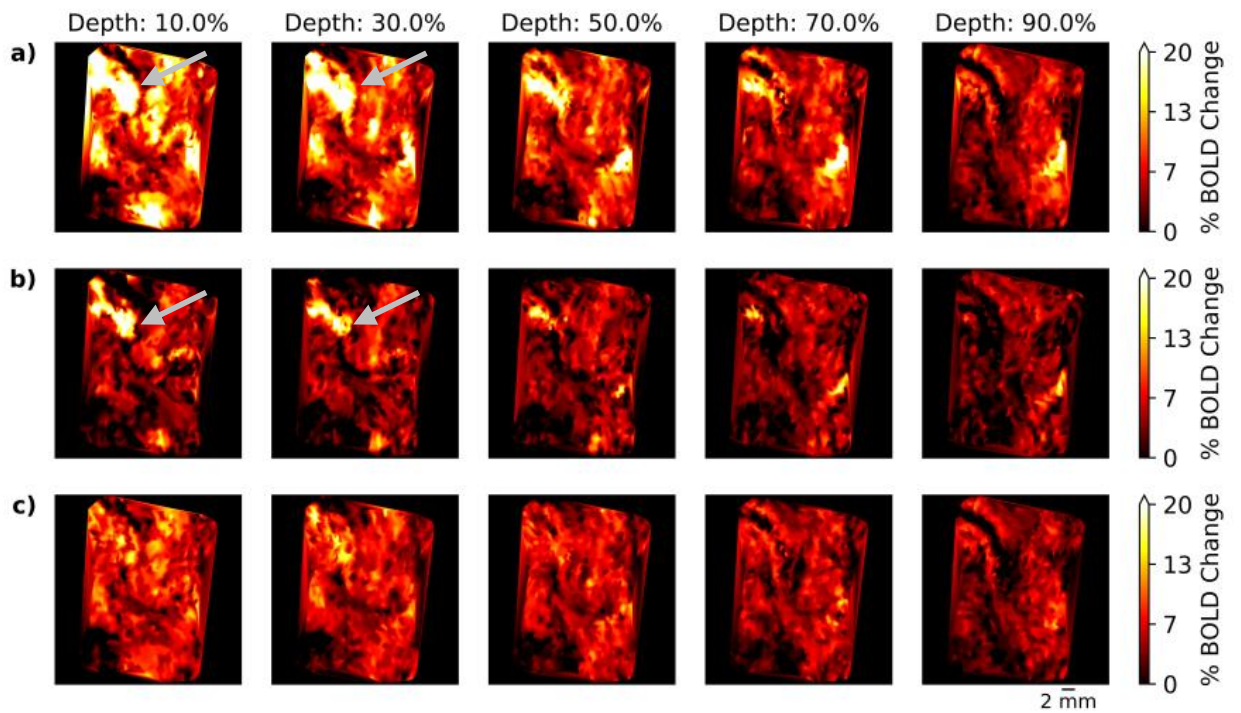
Figure 3.7: Laminar surface activation maps over a calcarine mask. Data is presented across equidistant cortical depths where 0% is the pial surface and 100% is the white matter boundary. a) GE-EPI % signal change, b) SE-EPI % signal change, c) GE-EPI-PR % signal change. Grey arrows indicate a region with a pial vein.

Figure 3.8 shows the R_2^* and M_0 product maps projected onto the cortical surfaces indicating the vessel locations from independent anatomy without the functional data. Also shown are the two metrics that illustrate the performance of the phase regression. These are the correlation between the fitted phase and magnitude (R^2), and the activation resulting from the fitted phase time series (estimated macrovascular activation). The R_2^* and M_0 map shows vessel like structures where the largest reduction in GE-EPI-PR % signal change occurred. The estimated macrovascular activation also shows areas of hyperintensity at these locations indicating that phase regression is suppressing venous signal. This can be further quantitatively investigated through examining the distributions of the different functional imaging methods.
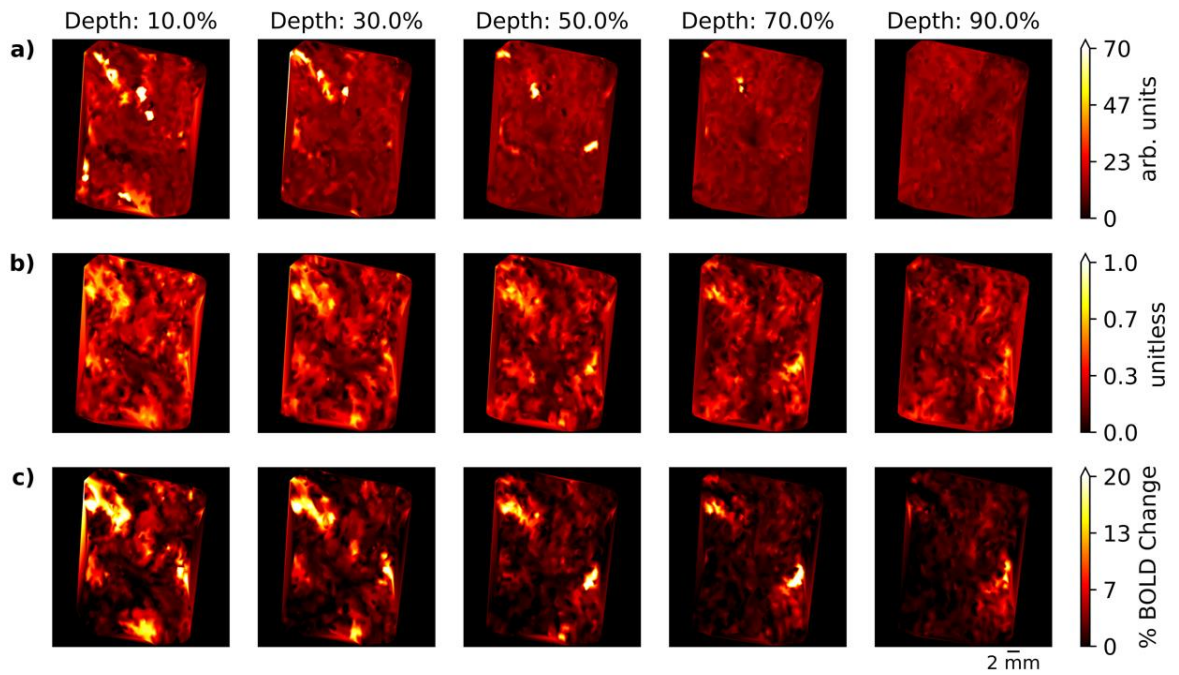
Figure 3.8: Vessel localization using R_2^* and M₀. a) Product of R_2^* and M_0 projected onto the cortical surface, b) Correlation between fitted phase and magnitude (R^2 of the phase regression fit), c) Activation resulting from the fitted phase timeseries (estimated macrovascular activation)

SE-EPI exhibits specificity to the microvasculature making it an appealing method for BOLD imaging of cortical substructures like columns [17]. By comparing the GE-EPI and GE-EPI-PR distributions to SE-EPI, a direct comparison to a microvascular control can be evaluated (Figure 3.9). A group of Kolmogorov–Smirnov tests with Bonferroni multiple comparisons correction were used in order to investigate similarities between distributions of the imaging methods. These tests show the distributions are all significantly different (p<0.05) except the distributions of GE-EPI-PR and SE-EPI from depths of 10 to 60% demonstrating that the distribution of GE-EPI-PR is more characteristic of SE-EPI than GE-EPI in the higher layers of cortex. This supports the hypothesis that GE-EPI-PR is suppressing pial vessel signal and producing a SE-EPI-like activation map.
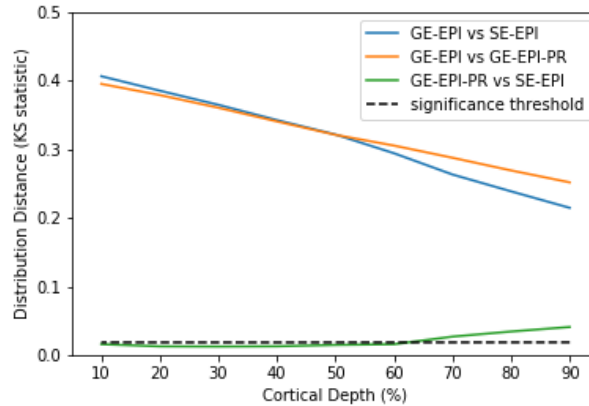
Figure 3.9: Test statistic of the two-sided Kolmogorov-Smirnov test between distributions as a function of depth. The dashed line represents the significance threshold (p<0.05) after Bonferroni comparisons correction across all depths.

One concern in using phase regression in fMRI processing is the reduced contrast-to-noise ratio. GE-EPI-PR shows signal suppression relative to GE-EPI (Figure 3.10). CNR was calculated by dividing the amplitude of the activation by the standard deviation of the residuals. This was done to investigate whether phase regression is introducing any noise through the fit subtraction process which could potentially reduce the method's efficacy. The average CNR across layers of the GE-EPI data is 0.9 ± 0.3 (mean $\pm$ std dev. across layers), for GE-EPI-PR the CNR is 0.5 ± 0.2 and finally SE-EPI has a CNR of 0.27 ± 0.07. This means the CNR of the SE-EPI data is only 30% of the GE-EPI data compared to the CNR of GE-EPI-PR which is 60% of the GE-EPI data. This shows that the phase regression method reduces GE-EPI CNR as expected, however it has higher CNR than SE-EPI. These findings suggest that although some noise may be introduced GE-EPI-PR is still an advantageous method to use over SE-EPI as it has more statistical power.
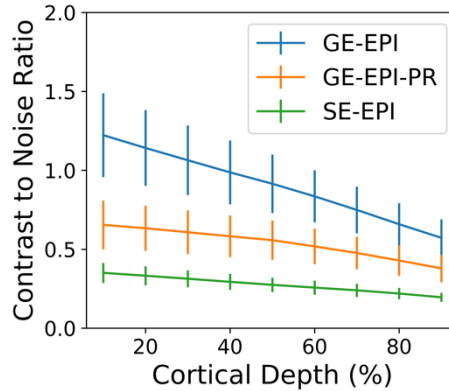
Figure 3.10: Laminar CNR profiles across subjects. Error bars represent the standard error of the mean across subjects. All vertices were used for this calculation.

Large venous vessels exhibit both an intra- and extra-vascular BOLD response. Removal of the extravascular bloom is an important component in reducing the signal bias from these large draining veins. The laminar profiles distal from all vessel vertices were examined in order to determine if this extravascular bloom was being successfully reduced. Two bins of vertices were created, one proximal to and one distal from a vessel vertex. Figure 3.11 shows laminar profiles over all vertices as well as for vertices proximal (<2.4mm) and distal to a vein (>2.4mm). The GE-EPI-PR data shows activation similar in profile to the GE-EPI data but with a lower percent signal change when distal from vasculature. The difference between the GE-EPI-PR and GE-EPI is most prominent in the higher depth vertices proximal to veins where the GE-EPI-PR laminar profiles have a lower slope than GE-EPI. This would indicate that the phase regression is reducing contribution from pial veins to a higher degree than tissue as we expect.
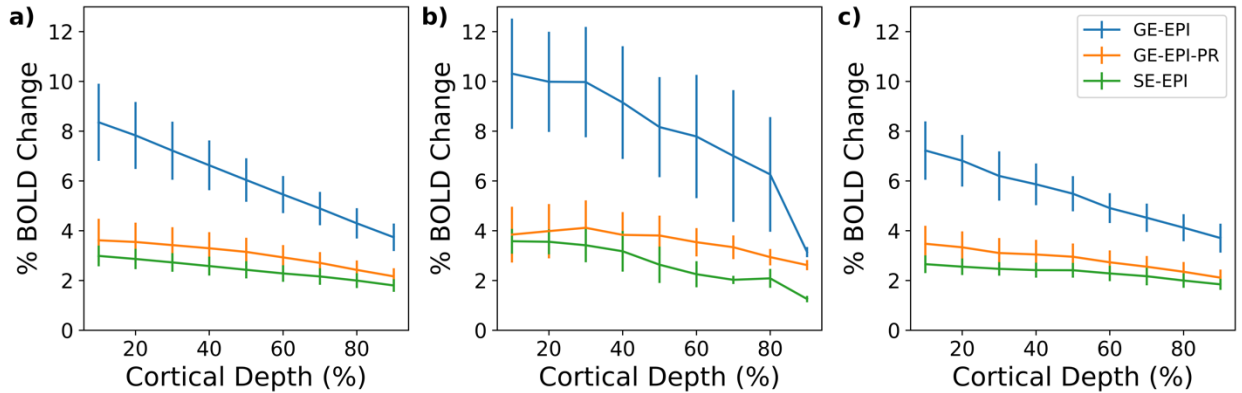
Figure 3.11: Laminar activation profiles across subjects. Error bars represent the standard error of the mean across subjects. a) Profile across all vertices, b) Profile across vertices proximal to a vein (thresholded at a Euclidean distance of 2.4 mm to a vessel vertex) and c) Profile across vertices distal to all veins.

3.4   Discussion

In this study, we investigated the use of phase regression on high-resolution GE-EPI data to assess the feasibility of the technique for use in intracortical BOLD fMRI at the laminar and/or columnar level. GE-EPI is an attractive sequence for use in high-resolution fMRI as it has an inherently higher contrast-to-noise ratio per unit time (sensitivity) compared to other popular intracortical fMRI approaches (i.e., SE-EPI, VASO, GRASE, or bSSFP), as well as lower SAR requirements and higher spatial coverage making it easier to achieve high temporal resolutions and shorter imaging times [15,60]. Unfortunately, GE-EPI suffers from macrovascular contamination leading to low specificity to the capillary bed microvasculature [16]. Phase regression of the GE-EPI images was investigated to determine if the specificity could be improved without sacrificing microvascular sensitivity, improving GE-EPI utility in high resolution studies. GE-EPI and GE-EPI-PR were compared to SE-EPI, a sequence that has been well studied and provides functional signal with specificity to the microvasculature [17]. We demonstrated the utility of phase regression for intracortical fMRI by showing GE-EPI-PR (1) has specificity across cortical surfaces comparable to SE-EPI, (2) has higher sensitivity than SE-EPI across all cortical layers, and (3) reduces the extravascular and intravascular functional contributions from pial veins compared to GE-EPI. With these

advantages in mind, GE-EPI-PR is a useful addition to a laminar imaging toolkit as it improves specificity of GE-EPI with only a minor reduction in sensitivity.

3.4.1   GE-EPI: Specificity and Sensitivity

GE-EPI is the workhorse sequence for fMRI studies and has advantages over T_2 based methods such as SE-EPI as it requires less RF power (lower SAR) and has higher SNR efficiency. As a result of the high SNR efficiency, GE-EPI has higher contrast-to-noise per unit time than SE-EPI, from 2 to 2.9 experimentally [18,28,61] and this has beneficial effects when voxels are evaluated for activation models such as tuning or encoding as the fits are more robust [28,62]. However, GE-EPI profiles as a function of cortical depth have a positive slope towards the cortical surface, indicative of large BOLD changes due to large pial vessels [14]. The tradeoff of sensitivity for specificity between GE and SE is further complicated by the high SAR requirements of SE-EPI which lengthen acquisition time and limit coverage [63]. Alternative sequences such as GRASE and VASO have been developed that have improved specificity compared to GE-EPI but also have reduced CNR, spatial coverage limitations and SAR restrictions [63,64]. Thus GE-EPI remains the most popular fMRI sequence to date and is widely used in the high-resolution fMRI field.

3.4.2   GE-EPI-PR: Specificity and Sensitivity

Large venous vessel BOLD signal reduction through phase regression produces activation maps (Figure 3.7) and laminar profiles (Figure 3.11) comparable to SE-EPI. Activation map similarity was quantified through two-sided Kolmogorov-Smirnov tests which show GE-EPI-PR and SE-EPI activation map distributions are not significantly different on the upper laminar surfaces of cortex (10-60% cortical depth). This demonstrates that phase regression produces a SE-EPI-like signal which will have higher specificity to microvasculature without incurring the conventional penalties for that specificity such as higher SAR and longer imaging times. Using GE-EPI-PR also offsets one of the major problems with SE-EPI, namely reduced sensitivity.

The low BOLD sensitivity of SE-EPI [15,19] produces data with low contrast-to-noise efficiency and often requires repeated acquisitions to increase the statistical power. Consistent with prior studies, we found SE-EPI has 30% of the CNR of GE-EPI data averaged across layers. Our approach demonstrates GE-EPI-PR doubles the CNR compared to SE-EPI across all layers which will make imaging using this technique more statistically powerful (Figure 3.10). This technique also shows GE-EPI-PR has 60% of the CNR of GE-EPI, which is the same as the CNR of VASO [64]. Utilizing GE-EPI-PR will therefore create a more microvasculature-weighted signal with increased sensitivity and some practical acquisition advantages over alternative fMRI sequences.

3.4.3   GE-EPI-PR: Venous signal suppression

Our hypothesis that phase regression decreases macrovascular signal in GE-EPI-PR activation maps predicts a lower activation in the areas that correspond to veins. Indeed, in this study, the GE-EPI-PR activation maps (Figure 3.7) show spatially varying suppression compared to GE-EPI with the largest suppression in the 'vessel' regions as identified from the multi-echo GRE scan (Figure 3.8). This observation is further supported in Figure 3.11 showing that the GE-EPI-PR laminar profiles in vertices proximal to vessels show increased signal suppression compared to vertices distal to vessels. These results are a promising indication that at high resolution, phase regression has the ability to also suppress extravascular signal [38], which was not observed in previous studies at low spatial resolution [34,65]. Extravascular signal is the dominant BOLD producer at 7T [66] and the specificity improvements from extravascular signal removal is particularly significant for pial veins as they have been shown to impact the signal distribution across the entire cortical ribbon of the visual cortex [67]. In addition to the extravascular suppression, this study observed intravascular suppression as expected by phase regression [34]. This has a similar effect to applying a diffusion gradient to a GE sequence to suppress intravascular BOLD effects [66,68]. Both extra- and intra-vascular signal suppression was greatest at the pial surface supporting the theory that phase regression exhibits the highest suppression effects near large vessels. All of the tangential and penetrating vasculature in cortex combines to confound BOLD signal distant from the capillary bed but for GE-EPI the effects from pial veins are dominant

[69] as proximity to a vessel affects the amplitude of the BOLD response to a greater degree than cortical depth. Phase regression results in functional maps with higher microvascular specificity to the capillary bed. This is important as previous studies have shown that performing venous removal on GE-EPI BOLD data results in laminar profiles more closely matched to the expected laminar profiles from histology [9,64].

3.4.4   Venous signal removal from GE-EPI in literature

Removing GE-EPI signal contributions from large venous vessels to increase the specificity to the microvasculature remains one of the open problems in high resolution GE-EPI fMRI research today. Several studies have demonstrated reducing large vessel signal contributions from GE-EPI BOLD data using masking, profile correction, experiment setups or selective analysis. One such approach, masking, can be performed using additional acquisitions such as multi-echo GREs to identify and mask venous vessels [24,28] but suffers from poor localization of the venous voxels after registration of the multi-echo scan to the distorted EPI space [70]. Phase regression is performed in native EPI space so will not suffer from these potential registration errors. Alternatively, it is possible to mask vessels by determining cutoff thresholds of EPI intensity or percent BOLD change in order to separate venous voxels from non-venous voxels in native EPI space [9,25] but hard cutoffs may not be able to separate venous and non-venous signal completely and may require manual segmentation (as was done in this study) or additional filtering [9]. Additionally, hard cutoffs fail to account for the gradual distance dependent reduction in extravascular effects. Fortunately, phase regression requires no cutoffs and GE-EPI-PR also is useful at removing extravascular effects from pial veins proximal to vessels. Laminar profile correction can be completed spatially through PSF estimation and deconvolution to remove bias from penetrating vessels [26] but it does not consider pial vein effects [15] unlike the phase regression technique. It is also possible to correct the profiles temporally by estimating an early and late response across an area with temporal decomposition through manifold fitting [30]. This technique, like phase regression is agnostic to venous size or orientation but does require finite impulse response modelling as an initial step which can be challenging in resting state or naturalistic paradigms. Using phase and magnitude data separately could add additional

power to the manifold fitting approach. Phase regression uses the correlation between magnitude and phase and therefore works across functional paradigms. Some experiments can reduce vessel bias using their experimental design, such as ocular dominance columns, where contrast subtraction removes most of the large venous effects [10,28] but this assumes linearity in the BOLD response and still shows some venous contamination [17]. It also eliminates the desirability of using single-condition maps. Other forms of selective analysis can be performed, such as focusing analysis on the initial dip of the BOLD signal as it is more spatially specific to the active microvascular blood pool, unfortunately it is smaller and requires additional modelling in order to determine the HRF voxel by voxel [27]. Alternatively, one can deliberately remove upper layers from further analysis [29] which limits the utility of intracortical fMRI to neuroscience problems fully described in the lower cortical depths. These experimental restrictions are not required by phase regression. Phase regression is an additional viable tool for this venous reduction literature as phase data is already available for many gradient echo sequences and only requires a robust phase sensitive method of coil combination.

3.4.5   Study Limitations

It is important to note, for studies requiring voxel sizes of less than a millimeter, appropriate echo times may only be achievable by using acceleration such as GRAPPA [71] or SENSE [72] possibly in combination with partial Fourier acquisition [73] which is ubiquitous in high-resolution EPI fMRI acquisitions in order to obtain short echo train lengths. The phase regression technique works regardless of partial Fourier as long as more than half of the k-space is collected. Although we expect the phase to be affected by the partial Fourier we do not expect, nor do we observe, its complete destruction. Our data did not exhibit artifacts such as Gibbs ringing in the phase data which we could expect from the use of zero-filled partial Fourier. This may be due to the relatively low SNR this data was collected with obscuring the expected ringing. This evaluation demonstrates that partial Fourier will produce data with a lower effective resolution but without contributing significant additional artifact in the images and/or resultant functional maps. Future work on phase regression will have to perform similar quality

assurance in order to determine that the GE sequence and acceleration parameters used are appropriate for phase data.

To examine the effects of sequence parameters on resolution, the magnitude of the complex PSF was reported for both GE-EPI and SE-EPI. The PSF provides additional acquisition information to the commonly reported nominal resolution and allows for an improved understanding of the effect acceleration has on our data. Several existing studies have attempted to compare PSFs this way in order to better explain the effects that different sequences and acceleration parameters have on their data [11,63]. This method calculating the magnitude of the complex PSF will not represent the physiological PSF [15,26,74] and will not provide results targeted at resolving a specific pattern such as ODCs [49]. However, our reported PSFs still provide a direct comparator between sequence parameters. This magnitude of the complex PSF represents the level of influence neighboring voxels have on each other in the phase-encode direction, the worst blurring case in our sequences [49]. Despite the blurring due to acceleration limitations these voxel sizes were sufficient to study reductions in macrovascular signal and still showed the phase regression effect at high resolution for the first time.

3.4.6   Future Work

Future work is needed to explore the properties of phase regression at high resolution. This study was conducted with limited spatial coverage, 22 mm in the slice direction limiting the ability to assess other aspects such as the relationship between phase regression and cortical orientation [75]. This was a deliberate choice due to the nature of the visual stimulation used. More study is needed to assess whether the phase regression effects reduce the orientation dependence of GE-EPI which is driven by pial vessels [76]. One additional area of interest would be the inclusion of phase regression into laminar modelling [26,77] as these methods focus on removal of penetrating vasculature and not correction for vessels on the pial surface. Finally, extension of phase regression to other GE sequences such as 3D-EPI could allow for wider adoption of this technique [78]. These proposed studies would help to expand the utility of phase regression beyond the investigation performed in this study.

3.5   Conclusions

This study has demonstrated that phase regression can be applied to reduce large vessel bias in high resolution functional acquisitions with complex data. Applying phase regression to GE-EPI data results in a similar activation map to SE-EPI while maintaining a higher contrast-to-noise ratio. Phase regression may be a useful tool in the laminar fMRI toolkit. This valuable technique can be used without additional acquisitions or equipment and requires only a method to combine phase data. Phase regressed GE-EPI is a powerful technique to reduce venous bias considered to be an important confounding factor at ultra-high fields and thus allowing GE-EPI imaging to have increased utility in laminar fMRI studies.

3.6   References

1.   Douglas RJ, Martin KAC. Neuronal Circuits of the Neocortex. Annu Rev Neurosci. 2004;27: 419–451. doi:10.1146/annurev.neuro.27.070203.144152

2.   Godlove DC, Maier A, Woodman GF, Schall JD. Microcircuitry of Agranular Frontal Cortex: Testing the Generality of the Canonical Cortical Microcircuit. J Neurosci. 2014;34: 5355–5369. doi:10.1523/JNEUROSCI.5127-13.2014

3.   Lund JS. Anatomical organization of macaque monkey striate visual cortex. Annu Rev Neurosci. 1988;11: 253–288. doi:10.1146/annurev.ne.11.030188.001345

4.   Self MW, van Kerkoerle T, Goebel R, Roelfsema PR. Benchmarking laminar fMRI: Neuronal spiking and synaptic activity during top-down and bottom-up processing in the different layers of cortex. NeuroImage. 2019;197: 806–817. doi:10.1016/j.neuroimage.2017.06.045

5.   Huber L, Handwerker DA, Jangraw DC, Chen G, Hall A, Stüber C, et al. High-Resolution CBV-fMRI Allows Mapping of Laminar Activity and Connectivity of Cortical Input and Output in Human M1. Neuron. 2017;96: 1253-1263.e7. doi:10.1016/j.neuron.2017.11.005

6.   Lawrence SJ, Norris DG, de Lange FP. Dissociable laminar profiles of concurrent bottom-up and top-down modulation in the human visual cortex. Büchel C, Frank MJ, Büchel C, editors. eLife. 2019;8: e44422. doi:10.7554/eLife.44422

7.   Olman CA, Harel N, Feinberg DA, He S, Zhang P, Ugurbil K, et al. Layer-Specific fMRI Reflects Different Neuronal Computations at Different Depths in Human V1. PLOS ONE. 2012;7: e32536. doi:10.1371/journal.pone.0032536

8. Ress D, Glover GH, Liu J, Wandell B. Laminar profiles of functional activity in the human brain. NeuroImage. 2007;34: 74–84. doi:10.1016/j.neuroimage.2006.08.020

9. Koopmans PJ, Barth M, Norris DG. Layer-specific BOLD activation in human V1. Hum Brain Mapp. 2010;31: 1297–1304. doi:10.1002/hbm.20936

10. Cheng K, Waggoner RA, Tanaka K. Human Ocular Dominance Columns as Revealed by High-Field Functional Magnetic Resonance Imaging. Neuron. 2001;32: 359–374. doi:10.1016/S0896-6273(01)00477-9

11. Feinberg DA, Vu AT, Beckett A. Pushing the limits of ultra-high resolution human brain imaging with SMS-EPI demonstrated for columnar level fMRI. NeuroImage. 2018;164: 155–163. doi:10.1016/j.neuroimage.2017.02.020

12. Menon RS, Ogawa S, Strupp JP, Uğurbil K. Ocular dominance in human V1 demonstrated by functional magnetic resonance imaging. J Neurophysiol. 1997;77: 2780–2787. doi:10.1152/jn.1997.77.5.2780

13. Moerel M, Martino FD, Uğurbil K, Formisano E, Yacoub E. Evaluating the Columnar Stability of Acoustic Processing in the Human Auditory Cortex. J Neurosci. 2018;38: 7822–7832. doi:10.1523/JNEUROSCI.3576-17.2018

14. Budde J, Shajan G, Zaitsev M, Scheffler K, Pohmann R. Functional MRI in human subjects with gradient-echo and spin-echo EPI at 9.4 T. Magn Reson Med. 2014;71: 209–218. doi:10.1002/mrm.24656

15. Koopmans PJ, Yacoub E. Strategies and prospects for cortical depth dependent T2 and T2* weighted BOLD fMRI studies. NeuroImage. 2019;197: 668–676. doi:10.1016/j.neuroimage.2019.03.024

16. Menon RS. The great brain versus vein debate. NeuroImage. 2012;62: 970–974. doi:10.1016/j.neuroimage.2011.09.005

17. Yacoub E, Shmuel A, Logothetis N, Uğurbil K. Robust detection of ocular dominance columns in humans using Hahn Spin Echo BOLD functional MRI at 7 Tesla. NeuroImage. 2007;37: 1161–1177. doi:10.1016/j.neuroimage.2007.05.020

18. Rua C, Costagli M, Symms MR, Biagi L, Donatelli G, Cosottini M, et al. Characterization of high-resolution Gradient Echo and Spin Echo EPI for fMRI in the human visual cortex at 7T. Magn Reson Imaging. 2017;40: 98–108. doi:10.1016/j.mri.2017.04.008

19. Yacoub E, Van De Moortele P-F, Shmuel A, Uğurbil K. Signal and noise characteristics of Hahn SE and GE BOLD fMRI at 7 T in humans. NeuroImage. 2005;24: 738–750. doi:10.1016/j.neuroimage.2004.09.002

20. Huber L, Ivanov D, Handwerker DA, Marrett S, Guidi M, Uludağ K, et al. Techniques for blood volume fMRI with VASO: From low-resolution mapping

towards sub-millimeter layer-dependent applications. NeuroImage. 2018;164: 131–143. doi:10.1016/j.neuroimage.2016.11.039

21. Lu H, Hua J, van Zijl PCM. Noninvasive functional imaging of cerebral blood volume with vascular-space-occupancy (VASO) MRI. NMR Biomed. 2013;26: 932–948. doi:10.1002/nbm.2905

22. Báez-Yánez MG, Ehses P, Mirkes C, Tsai PS, Kleinfeld D, Scheffler K. The impact of vessel size, orientation and intravascular contribution on the neurovascular fingerprint of BOLD bSSFP fMRI. NeuroImage. 2017;163: 13–23. doi:10.1016/j.neuroimage.2017.09.015

23. De Martino F, Zimmermann J, Muckli L, Ugurbil K, Yacoub E, Goebel R. Cortical depth dependent functional responses in humans at 7T: improved specificity with 3D GRASE. PloS One. 2013;8: e60514. doi:10.1371/journal.pone.0060514

24. Chen G, Wang F, Gore JC, Roe AW. Layer-specific BOLD activation in awake monkey V1 revealed by ultra-high spatial resolution functional magnetic resonance imaging. NeuroImage. 2013;64: 147–155. doi:10.1016/j.neuroimage.2012.08.060

25. Kay K, Jamison KW, Vizioli L, Zhang R, Margalit E, Ugurbil K. A critical assessment of data quality and venous effects in sub-millimeter fMRI. NeuroImage. 2019 [cited 7 Feb 2019]. doi:10.1016/j.neuroimage.2019.02.006

26. Markuerkiaga I, Barth M, Norris DG. A cortical vascular model for examining the specificity of the laminar BOLD signal. NeuroImage. 2016;132: 491–498. doi:10.1016/j.neuroimage.2016.02.073

27. Siero JCW, Ramsey NF, Hoogduin H, Klomp DWJ, Luijten PR, Petridou N. BOLD specificity and dynamics evaluated in humans at 7 T: comparing gradient-echo and spin-echo hemodynamic responses. PloS One. 2013;8: e54560. doi:10.1371/journal.pone.0054560

28. Moerel M, De Martino F, Kemper VG, Schmitter S, Vu AT, Uğurbil K, et al. Sensitivity and specificity considerations for fMRI encoding, decoding, and mapping of auditory cortex at ultra-high field. NeuroImage. 2018;164: 18–31. doi:10.1016/j.neuroimage.2017.03.063

29. Polimeni JR, Fischl B, Greve DN, Wald LL. Laminar analysis of 7T BOLD using an imposed spatial activation pattern in human V1. NeuroImage. 2010;52: 1334–1346. doi:10.1016/j.neuroimage.2010.05.005

30. Kay K, Jamison KW, Zhang R-Y, Uğurbil K. A temporal decomposition method for identifying venous effects in task-based fMRI. Nat Methods. 2020; 1–7. doi:10.1038/s41592-020-0941-6

31. Caballero-Gaudes C, Reynolds RC. Methods for cleaning the BOLD fMRI signal. NeuroImage. 2017;154: 128–149. doi:10.1016/j.neuroimage.2016.12.018

32. Curtis AT, Hutchison RM, Menon RS. Phase based venous suppression in resting-state BOLD GE-fMRI. NeuroImage. 2014;100: 51–59. doi:10.1016/j.neuroimage.2014.05.079

33. Curtis AT, Menon RS. Highcor: a novel data-driven regressor identification method for BOLD fMRI. NeuroImage. 2014;98: 184–194. doi:10.1016/j.neuroimage.2014.05.013

34. Menon RS. Postacquisition suppression of large-vessel BOLD signals in high-resolution fMRI. Magn Reson Med. 2002;47: 1–9. doi:10.1002/mrm.10041

35. Duvernoy HM, Delon S, Vannson JL. Cortical blood vessels of the human brain. Brain Res Bull. 1981;7: 519–579. doi:10.1016/0361-9230(81)90007-1

36. Klassen L, Menon RS. BOLD signal phase and magnitude dependence on vessel geometry. Proceedings of the 13th International Society for Magnetic Resonance in Medicine Annual Meeting. Miami, FL; 2005.

37. Ogawa S, Menon RS, Tank DW, Kim SG, Merkle H, Ellermann JM, et al. Functional brain mapping by blood oxygenation level-dependent contrast magnetic resonance imaging. A comparison of signal characteristics with a biophysical model. Biophys J. 1993;64: 803–812. doi:10.1016/S0006-3495(93)81441-3

38. Vu AT, Gallant JL. Using a novel source-localized phase regressor technique for evaluation of the vascular contribution to semantic category area localization in BOLD fMRI. Front Neurosci. 2015;9. doi:10.3389/fnins.2015.00411

39. Gilbert KM, Gati JS, Menon RS. Occipital-Parietal Coil with variable-density element distribution for 7T functional imaging. Proceedings of the 25th International Society for Magnetic Resonance in Medicine Annual Meeting. Honolulu, USA; 2017.

40. Yarnykh VL. Actual flip-angle imaging in the pulsed steady state: a method for rapid three-dimensional mapping of the transmitted radiofrequency field. Magn Reson Med. 2007;57: 192–200. doi:10.1002/mrm.21120

41. Nehrke K. On the steady-state properties of actual flip angle imaging (AFI). Magn Reson Med. 2009;61: 84–92. doi:10.1002/mrm.21592

42. Curtis AT, Gilbert KM, Klassen LM, Gati JS, Menon RS. Slice-by-slice B1+ shimming at 7 T. Magn Reson Med. 2012;68: 1109–1116. doi:10.1002/mrm.23319

43. Stanley OW, Menon RS, Klassen LM. Phase sensitive receiver combination using prescan singular value decomposition derived receiver sensitivities. Proceedings of the 27th International Society for Magnetic Resonance in Medicine Annual Meeting. Paris, France; 2018.

44. Bollmann S, Robinson SD, O'Brien K, Vegh V, Janke A, Marstaller L, et al. The challenge of bias-free coil combination for quantitative susceptibility mapping at ultra-high field. Magn Reson Med. 2018;79: 97–107. doi:10.1002/mrm.26644

45. Robinson SD, Dymerska B, Bogner W, Barth M, Zaric O, Goluch S, et al. Combining phase images from array coils using a short echo time reference scan (COMPOSER). Magn Reson Med. 2017;77: 318–327. doi:10.1002/mrm.26093

46. Parker DL, Payne A, Todd N, Hadley JR. Phase reconstruction from multiple coil data using a virtual reference coil. Magn Reson Med. 2014;72: 563–569. doi:10.1002/mrm.24932

47. Walsh DO, Gmitro AF, Marcellin MW. Adaptive reconstruction of phased array MR imagery. Magn Reson Med. 2000;43: 682–690. doi:10.1002/(SICI)1522-2594(200005)43:5<682::AID-MRM10>3.0.CO;2-G

48. Hansen MS, Sørensen TS. Gadgetron: an open source framework for medical image reconstruction. Magn Reson Med. 2013;69: 1768–1776. doi:10.1002/mrm.24389

49. Chaimow D, Shmuel A. A more accurate account of the effect of k-space sampling and signal decay on the effective spatial resolution in functional MRI. bioRxiv. 2017; 097154. doi:10.1101/097154

50. Gorgolewski KJ, Esteban O, Ellis DG, Notter MP, Ziegler E, Johnson H, et al. Nipype: a flexible, lightweight and extensible neuroimaging data processing framework in Python. 0.13.1. Zenodo; 2017. doi:10.5281/zenodo.581704

51. Cox RW. AFNI: Software for Analysis and Visualization of Functional Magnetic Resonance Neuroimages. Comput Biomed Res. 1996;29: 162–173.

52. Jenkinson M, Beckmann CF, Behrens TEJ, Woolrich MW, Smith SM. FSL. NeuroImage. 2012;62: 782–790. doi:10.1016/j.neuroimage.2011.09.015

53. Jorge J, Figueiredo P, Gruetter R, van der Zwaag W. Mapping and characterization of positive and negative BOLD responses to visual stimulation in multiple brain regions at 7T. Hum Brain Mapp. 2018;39: 2426–2441. doi:10.1002/hbm.24012

54. Behzadi Y, Restom K, Liau J, Liu TT. A Component Based Noise Correction Method (CompCor) for BOLD and Perfusion Based fMRI. NeuroImage. 2007;37: 90–101. doi:10.1016/j.neuroimage.2007.04.042

55. Welvaert M, Rosseel Y. On the Definition of Signal-To-Noise Ratio and Contrast-To-Noise Ratio for fMRI Data. PLOS ONE. 2013;8: e77089. doi:10.1371/journal.pone.0077089

56. Dale AM, Fischl B, Sereno MI. Cortical surface-based analysis. I. Segmentation and surface reconstruction. NeuroImage. 1999;9: 179–194. doi:10.1006/nimg.1998.0395

57. Fischl B, Sereno MI, Dale AM. Cortical surface-based analysis. II: Inflation, flattening, and a surface-based coordinate system. NeuroImage. 1999;9: 195–207. doi:10.1006/nimg.1998.0396

58. Fernández-Seara MA, Wehrli FW. Postprocessing technique to correct for background gradients in image-based R*(2) measurements. Magn Reson Med. 2000;44: 358–366. doi:10.1002/1522-2594(200009)44:3<358::aid-mrm3>3.0.co;2-i

59. Avants BB, Tustison NJ, Song G, Cook PA, Klein A, Gee JC. A reproducible evaluation of ANTs similarity metric performance in brain image registration. NeuroImage. 2011;54: 2033–2044. doi:10.1016/j.neuroimage.2010.09.025

60. Beckett AJS, Dadakova T, Townsend J, Huber L, Park S, Feinberg DA. Comparison of BOLD and CBV using 3D EPI and 3D GRASE for cortical layer functional MRI at 7 T. Magn Reson Med. 2020;84: 3128–3145. doi:10.1002/mrm.28347

61. Schumacher JF, Thompson SK, Olman C. Contrast Response Functions for Single Gabor Patches: ROI-Based Analysis Over-Represents Low-Contrast Patches for GE BOLD. Front Syst Neurosci. 2011;5. doi:10.3389/fnsys.2011.00019

62. Olman CA, Van de Moortele P-F, Schumacher JF, Guy J, Uğurbil K, Yacoub E. Retinotopic mapping with Spin Echo BOLD at 7 Tesla. Magn Reson Imaging. 2010;28: 1258–1269. doi:10.1016/j.mri.2010.06.001

63. Kemper VG, De Martino F, Vu AT, Poser BA, Feinberg DA, Goebel R, et al. Sub-millimeter T2 weighted fMRI at 7 T: comparison of 3D-GRASE and 2D SE-EPI. Front Neurosci. 2015;9. doi:10.3389/fnins.2015.00163

64. Huber L, Goense J, Kennerley AJ, Trampel R, Guidi M, Reimer E, et al. Cortical lamina-dependent blood volume changes in human brain at 7T. NeuroImage. 2015;107: 23–33. doi:10.1016/j.neuroimage.2014.11.046

65. Barry RL, Gore JC. Enhanced phase regression with savitzky-golay filtering for high-resolution BOLD fMRI. Hum Brain Mapp. 2014;35: 3832–3840. doi:10.1002/hbm.22440

66. Duong TQ, Yacoub E, Adriany G, Hu X, Ugurbil K, Kim S-G. Microvascular BOLD contribution at 4 and 7 T in the human brain: gradient-echo and spin-echo fMRI with suppression of blood effects. Magn Reson Med. 2003;49: 1019–1027. doi:10.1002/mrm.10472

67. Fracasso A, Luijten PR, Dumoulin SO, Petridou N. Laminar imaging of positive and negative BOLD in human visual cortex at 7T. NeuroImage. 2018;164: 100–111. doi:10.1016/j.neuroimage.2017.02.038

68. Boxerman JL, Bandettini PA, Kwong KK, Baker JR, Davis TL, Rosen BR, et al. The intravascular contribution to fMRI signal change: Monte Carlo modeling and

diffusion-weighted studies in vivo. Magn Reson Med. 1995;34: 4–10. doi:10.1002/mrm.1910340103

69. Bause J, Polimeni JR, Stelzer J, In M-H, Ehses P, Kraemer-Fernandez P, et al. Impact of prospective motion correction, distortion correction methods and large vein bias on the spatial accuracy of cortical laminar fMRI at 9.4 Tesla. NeuroImage. 2020;208: 116434. doi:10.1016/j.neuroimage.2019.116434

70. Polimeni JR, Renvall V, Zaretskaya N, Fischl B. Analysis strategies for high-resolution UHF-fMRI data. NeuroImage. 2018;168: 296–320. doi:10.1016/j.neuroimage.2017.04.053

71. Griswold MA, Jakob PM, Heidemann RM, Nittka M, Jellus V, Wang J, et al. Generalized autocalibrating partially parallel acquisitions (GRAPPA). Magn Reson Med. 2002;47: 1202–1210. doi:10.1002/mrm.10171

72. Pruessmann KP, Weiger M, Scheidegger MB, Boesiger P. SENSE: sensitivity encoding for fast MRI. Magn Reson Med. 1999;42: 952–962. doi:https://doi.org/10.1002/(SICI)1522-2594(199911)42:5<952::AID-MRM16>3.0.CO;2-S

73. Feinberg DA, Hale JD, Watts JC, Kaufman L, Mark A. Halving MR imaging time by conjugation: demonstration at 3.5 kG. Radiology. 1986;161: 527–531. doi:10.1148/radiology.161.2.3763926

74. Menon RS, Goodyear BG. Submillimeter functional localization in human striate cortex using BOLD contrast at 4 Tesla: implications for the vascular point-spread function. Magn Reson Med. 1999;41: 230–235. doi:10.1002/(sici)1522-2594(199902)41:2<230::aid-mrm3>3.0.co;2-o

75. Stanley OW, Kuurstra AB, Menon RS. Phase-based macrovascular filtering from gradient echo bold fMRI reduces orientation dependence. Proceedings of Neuroscience 2019. Chicago IL; 2019. Available: https://www.abstractsonline.com/pp8/#!/7883/presentation/69549

76. Viessmann O, Scheffler K, Bianciardi M, Wald LL, Polimeni JR. Dependence of resting-state fMRI fluctuation amplitudes on cerebral cortical orientation relative to the direction of B0 and anatomical axes. NeuroImage. 2019;196: 337–350. doi:10.1016/j.neuroimage.2019.04.036

77. Havlicek M, Uludag K. A dynamical model of the laminar BOLD response. bioRxiv. 2019; 609099. doi:10.1101/609099

78. Hendriks AD, D'Agata F, Raimondo L, Schakel T, Geerts L, Luijten PR, et al. Pushing functional MRI spatial and temporal resolution further: High-density receive arrays combined with shot-selective 2D CAIPIRINHA for 3D echo-planar imaging at 7 T. NMR Biomed. 2020;33: e4281. doi:10.1002/nbm.4281

4 Phase Regression in Macaques: An investigation of physiological confounds

Olivia W Stanley, Geoffrey N Ngo, Ravi S Menon

This article is in preparation.

Macaques are a useful model for laminar imaging as functional imaging can be performed alongside electrophysiology for the investigation of questions into the BOLD mechanism. Implementing phase regression in a macaque model would allow for such studies to be completed with increased microvascular specificity as previous work has shown that pial vessel bias, observed in humans in Chapter 3, also exists in macaques. This pilot study examined the efficacy of phase regression in a macaque model as a method of improving specificity for macaque laminar fMRI studies. Resting state magnitude and phase data was collected to assess the effect that phase regression had on macaque functional data. The resting state data was processed under two different physiological cleaning strategies: applying cleaning before and after phase regression. Neither strategy allowed phase regression to perform optimally as a macrovascular filter due to respiration artifacts. Future work should investigate on-system physiological correction to remove these large artifacts from the data.

4.1   Introduction

Functional MRI is a non-invasive technique using endogenous contrast [1] that has proven to be a transformative tool in the study of cognition in both human and animal models [2]. Macaques are a common model for functional MRI, bridging the gap between human and small animal research due to their similar brain topology and ability to perform higher cognitive order tasks [3]. Additionally, macaques are used to study laminar activity and the BOLD response as it is possible to perform electrophysiology and fMRI simultaneously in the same animal [4]. The gold standard method for

performing fMRI is using blood oxygenation level dependent (BOLD) contrast [5] collected with gradient-echo echo planar imaging (GE-EPI). BOLD fMRI measures signal changes from blood oxygenation to determine neural activation in an area [4]. Unfortunately, BOLD contrast is an indirect vascular measure of neural activity, and this can present a challenge to spatially localize BOLD signal to the correct area of the cortex [6].

Macrovascular contamination is one cause of uncertainty in spatial localization, whereby large pial veins on the cortical surface pool oxygenated blood flowing from BOLD responses occurring within the cortex resulting in ambiguous localization of activation [6]. Phase regression (PR) takes advantage of the often-under-utilized phase signal from fMRI to identify and reduce draining vein contributions. To do this, PR models each voxel as a mix of two signal populations: a macrovascular, and a microvascular BOLD signal. Fortunately, due to signal dependence on vessel size and vessel orientations, the phase signal of fMRI is most sensitive to large vessels and any signal correlated with both magnitude and phase time courses can be assumed to be macrovascular in origin. This correlated signal is estimated through a linear regression and then subtracted from the magnitude signal to lower the magnitude signal's macrovascular weighting and produce a signal with higher microvascular specificity (GE-EPI-PR). PR has previously been used to reduce the macrovascular contamination in human subjects in both task [7–10] and resting-state fMRI experiments [11].

Implementing PR in a macaque model could reduce macrovascular signal from pial vessels creating more microvasculature specific fMRI results. Pial vessel contamination is an established issue in macaque fMRI and correcting it in the past has used optical methods of vein detection [12], using both BOLD and cerebral blood volume (CBV) functional imaging in combination [13], or spin echo imaging which is more specific to microvascular signal [14]. PR requires no additional equipment like the optical case, does not require twice the functional imaging as was done in the BOLD and CBV study, and was shown to have better contrast to noise than spin echo in the human study performed in Chapter 3. PR operating as a macrovascular filter in macaques could also provide an ideal model for investigating the size of vessels that are affected by PR [15].

BOLD signal shows a cortical orientation dependence that can be used to determine the orientation of the vessels dominating the BOLD response. At 7T, pial vasculature has been found to dominate resting state signal in humans [16]. A similar cortical orientation study could be used to determine the size of vasculature affected by PR. A reduction in cortical orientation dependence would indicate suppression of the pial vasculature. A sedated macaque model is a good candidate for this experiment as sedated macaques exhibit resting state activity [17], can undergo long experiments, and have minimal head motion. This pilot study seeks to determine the efficacy of PR in a macaque model to begin the pursuit of this cortical orientation study.

One challenge of performing PR is that the phase signal shows more artifacts and noise than the magnitude signal. It has shown increased sensitivity to breathing and other physiological effects [18], scanner noise [19], and non-BOLD susceptibility effects [20], in addition to lost signal near the air-tissue interfaces such as the sinus region [21]. As PR is performed on the relative phase time courses, only artifacts that affect the phase through time will create issues with this technique. These potential artifacts are mass motion field shifts because of breathing [18], increased physiological noise from the cardiac or respiratory cycle [19], and higher sensitivity to scanner noise [19]. Previous work has shown that these artifacts can be mitigated in humans using either a global frequency correction for physiological phase changes (DORK [22]) or post-imaging regression of physiological traces (RETROICOR [23]). The degree to which these artifact sources affect the phase signal as well as how effectively they can be corrected has not been examined in macaques to date.

Mass motion field shifts are a major contributor to phase artifacts and occur when motion outside the imaging region creates inhomogeneities in the magnetic field [24]. These field shifts have been observed in human studies during swallowing [25] and reaching and grasping tasks [26]. Mass motion artifacts can also be caused by respiration as the chest moves and have been shown to affect the phase more than the magnitude images [18]. These artifacts result in shifts in the global frequency which change image intensity but are not due to BOLD contrast. Previous work has corrected mass motion artifacts in humans where PR [27] in combination with navigator echoes can reduce the

artifacts [26]. In these studies, PR was employed not as a macrovascular filter but to reduce the mass motion artifact.

To date, PR efficacy for macrovascular suppression in a macaque model has not been assessed. Performing PR in a macaque will have different challenges such as imaging in the sphinx position, where the macaque lays prone in the magnet with their gaze facing forward through the bore. Macaques are usually scanned in sphinx position and have differing body geometry which could result in more respiratory signal contamination due to the proximity of the lungs to the imaging region. Additionally, macaques are routinely imaged under sedation which can cause attenuated resting state signal [17] and could reduce PR performance as there is less BOLD signal change overall. These confounds require investigating and quantifying prior to further PR studies in macaques. The PR method could provide improvement in spatial specificity of BOLD contrast which would directly benefit laminar macaque studies.

This study seeks to investigate the efficacy of PR in a macaque animal model during resting-state fMRI. This would allow for greater spatial specificity in laminar macaque studies as it would reduce pial vessel bias. Factors such as sedation, body geometry, and scanner noise can all affect the efficacy of the PR technique to fit and remove signal and must be considered when migrating this technique to animals. This study attempts to quantify these artifact sources in both the magnitude and phase data as well as investigate whether there is a suitable fMRI denoising workflow that can improve PR results. First, the quantification of confounds is composed of two parts: examining the phase and magnitude spectra for artifacts and quantifying their relative signal power. Second, resting-state connectivity is calculated using two methods of physiological cleaning to examine connectivity in PR timeseries. This study aims to investigate PR to determine if it is an effective fMRI preprocessing strategy for future applications of fMRI in macaque studies.

4.2   Methods

4.2.1   Animal Preparation

All imaging described below was performed in accordance with the guidelines of the Canadian Council on Animal Care policy on the care and use of experimental animals and an ethics protocol approved by the Animal Care Committee of the University of Western Ontario. Animals were under close supervision by the university veterinarians. Two female macaques (*Macaca fascicularis*) were anesthetized with ketamine (10 mg/kg) and propofol (1.3 mg/kg) and sedation was maintained with isoflurane for the imaging duration. Isoflurane was kept to 1-1.25% when functional images were acquired.

4.2.2   Imaging

Imaging was performed using a 680 mm neuro-optimized 7 T MRI (Siemens Magnetom Step 2.3, Erlangen, Germany) equipped with an AC84 Mark II head gradient coil. The animals were scanned in sphinx position in a custom built 8 channel transmit, 24 channel receive RF array intended for use with animals [28]. Structural MP2RAGE images were collected with 500 um isotropic resolution, TE/TR = 3.9/6500 ms, TI=800/2700 ms, BW = 150 Hz/Px and FA = 4°/5°. Additionally to better delineate the pial surface, a T_2-weighted turbo spin echo scan was collected with resolution 0.3x0.3x1.1 mm, TE/TR = 85/7500 ms, BW = 220 Hz/Px, and FA = 120°.

Functional imaging was collected in 10-minute runs with a GE-EPI sequence with 1.0 mm isotropic resolution (10% slice gap), TE/TR = 22/1000 ms, BW = 1860 Hz/Px, FA = 40°, multiband factor 2, GRAPPA of 2, and partial fourier of 7/8 (zero-filled) [29]. Subject R had 10 runs collected (100 minutes) and Subject O had 6 runs collected (60 minutes). To collect phase data, the fitted SVD method (Chapter 2) was used for coil combination [30]. Briefly, this method uses a voxelwise singular value decomposition of the B_1^+ shimming prescan to calculate relative coil sensitivities which are fit to a polynomial basis allowing for their application to later imaging runs [30].

4.2.3   Structural Image Registration to Standard Space

For this project the pipelining software *macapype* was used to create a segmentation and register the structural image to the D99 atlas in NMT space [31]. This software uses a combination of the T1-weighted and T2-weighted scans to perform denoising using AFNI [32], brain extraction using atlasbrex [33], NMT registration followed by Atropos segmentation [34]. Registration of the structural scan was completed using *macapype* which used linear and non-linear AFNI based registration [32] to register the structural image to the NMT template version 1.2 [31].

4.2.4   Functional Image Preprocessing

Functional data was preprocessed using the phaseprep toolbox (https://github.com/ostanley/phaseprep), constructed in nipype [35]. This toolbox first processed the magnitude data through *3dVolReg* motion correction [32], alignment to the first functional run using *3dAllineate* [32], linear detrending, and masking of the magnitude data using FSL's *BET* [36]. Phase data does not have similar image characteristics to magnitude data, and it is not well suited to motion correction or registration with established neuroimaging software. Phase data therefore undergoes processing using parameters from the magnitude data. The phaseprep toolbox was used to convert the phase of the timeseries to radians and motion correct the functional data in real and imaginary space using the transforms from the magnitude data preprocessing. Motion correction is done in real and imaginary space as it does not contain phase wraps. The motion corrected real and imaginary images are transformed back into phase data which is temporally unwrapped and linearly detrended as final preprocessing steps.

Temporal signal to noise was calculated after preprocessing was complete. The detrended magnitude timeseries was used to create a voxelwise map of the mean signal over the standard deviation. The temporal standard deviation of the phase data was similarly calculated over the preprocessed phase timeseries.

4.2.5   Phase Regression

PR was performed using orthogonal distance regression (ODR) with the following linear model:

$$M = A\varphi + B$$

where M is the magnitude signal (GE-EPI), φ is the phase signal, and A and B are the fit coefficients. The resulting microvascular weighted signal, M_{micro}, (GE-EPI-PR) is then calculated as follows:

$$M_{micro} = M - (A\varphi + B)$$

ODR was used as it allows for random errors in both magnitude and phase [37] which is representative of the situation when estimating a fit between two MRI signals. ODR requires estimation of the noise in both magnitude and phase to perform optimally. Given a single magnitude measurement of $M_i = M_i^* + \varepsilon_i$ and a phase measurement of $\varphi_i = \varphi_i^* + \eta_i$, where i is an individual timepoint, M_i and φ_i are the measured magnitude and phase data at that point, M_i^* and φ_i^* are the true magnitude and phase values that lie on the regression line and ε_i and η_i are the noise in the respective measurements. ODR minimizes the following sum of the squared residuals (SSR) as follows:

$$SSR = \frac{1}{\sigma_\varepsilon^2} \sum_{i=1}^{n} \left((M_i - B - AM_i^*)^2 + \frac{\sigma_\varepsilon^2}{\sigma_\eta^2} (\varphi_i - \varphi_i^*)^2 \right)$$

Where n is the number of image volumes, σ_ε and σ_η were the standard deviation of the two signals and were estimated by applying a 0.15 Hz high-pass threshold and taking the standard deviation of the remaining signal as the noise estimate.

4.2.6   Physiological Signal Cleaning

Denoising of physiological time series was performed with CompCor [38]. RETROICOR [39] was not implemented due to unreliable signal recording from the respiratory belt and pulse oximeter synchronized with the scanner. This poor recording

performance was a result of animal skin pigment and small animal size. As such, CompCor post-processing was selected as the main physiological signal correction, which has been found to provide identical correction to RETROICOR in human subjects [38]. Physiological signal cleaning was performed with *3dTproject* [32] and the nipype *TCompCor* interface [35] to filter out 12 confound regressors (6 from TCompCor and the 6 motion parameters from preprocessing) as well as temporally filter the data with a bandpass filter of 0.01 to 0.1 Hz. This physiological signal denoising was applied in the following two cases, (1) post-PR and (2) pre-PR where physiological cleaning was applied after and prior-to phase regression, respectively. The post-PR cleaning case is equivalent to previous PR studies in human tasks (Chapter 3) and the pre-PR cleaning case is equivalent to the previous study on PR in resting state in human subjects [11]. One note, in the pre-PR cleaning case the signals input to the PR fit were temporally band pass filtered as part of the physiological cleaning and therefore cannot be used to estimate noise above 0.15Hz. For this case, the noise estimates used timeseries that had undergone all physiological cleaning except the band pass filtering step.

4.2.7   Functional to Structural Registration

EPI registration was completed using the mean functional image averaged across all runs after motion correction and first run alignment. This mean was calculated using *fslmaths* and was used to improve SNR. Coarse unrestricted registration was then completed using *FLIRT* to provide initial alignment. This registration was then passed to *ANTS* to perform the main registration. *ANTS* registration is performed in three stages: a rigid, 6 degrees of freedom linear registration; an affine, 12 degrees of freedom linear registration; and then a non-linear Symmetric Normalization registration bounded to the in-plane directions. This was done to help compensate for the EPI distortion in the phase encode direction [40]. Registration was evaluated using manual observation. The labels of the D99 atlas were then transformed to each subject's EPI space for all resting state analysis.

4.2.8   Power Spectra Analysis

The power spectra from each run were calculated over all voxels in the D99 atlas using SciPy's *periodogram* function and then averaged together. Integrals of band power were calculated using the composite Simpsons rule and divided by the integral of the whole signal as measures of relative power. This allows for direct comparison across frequency bands. Power spectra for individual voxels were identically calculated without any spatial averaging of the signal. Two frequency bands of interest were defined: the signal band from 0.01 to 0.1 Hz is expected to contain the resting-state activity, and the noise band at 0.15 Hz and above is expected to only contain noise from thermal and physiological contributions. These bands are defined identically to previous work on PR in resting-state [11].

4.2.9   Connectivity Mapping

Connectivity mapping was completed with the nilearn toolbox [41]. Prior to the resting state analysis timeseries were normalized to z-scores. Additionally, the physiological cleaning of the post-PR case was applied at this point in processing. This case was bandpass filtered to the signal band (0.01-0.1 Hz) prior to fitting and confound regression was performed as part of the general linear model and correlation steps. In this way both physiological cleaning cases compared data with the same cleaning applied, the only difference is where the cleaning was applied relative to the phase regression step.

Seed based analysis was then performed using the D99 atlas in native EPI space to extract signals from three seeds: PGm, a parietal area implicated in the macaque DMN [3]; F1, the primary motor area [31]; and MT, a visual area involved in motion perception [31]. These seeds were selected as they are in relatively high signal areas in both subjects and have well understood expected connectivity in a macaque model [3]. These seed voxel timeseries were fit to the data using a general linear model. These first level fits across runs were then combined in a one-sided t-test and displayed with a false positive rate of 0.1-5% and a cluster size of 10. To perform a whole brain connectivity analysis all 194 D99 areas were correlated to each other to create whole brain connectivity matrices.

4.3 Results

4.3.1 Image Quality

Image quality was assessed through magnitude temporal signal-to-noise ratio and phase temporal standard deviation. The images for both monkeys can be seen in Figure 4.1. Briefly, the temporal SNR shows decreases near the ventral surface of the brain distant from the coil as well as in the occipital lobe. This SNR decrease is mirrored in the temporal phase noise where the noise level in the visual cortex matches the background at the posterior of the brain. This decrease in SNR is due to animal placement in the sphinx position. This position results in the brain being further from the coil near the occipital region as well as partially covered by the neck fat. Additionally, due to prior placement of electrodes, Subject O had signal dropout in the frontal lobe of their brain.
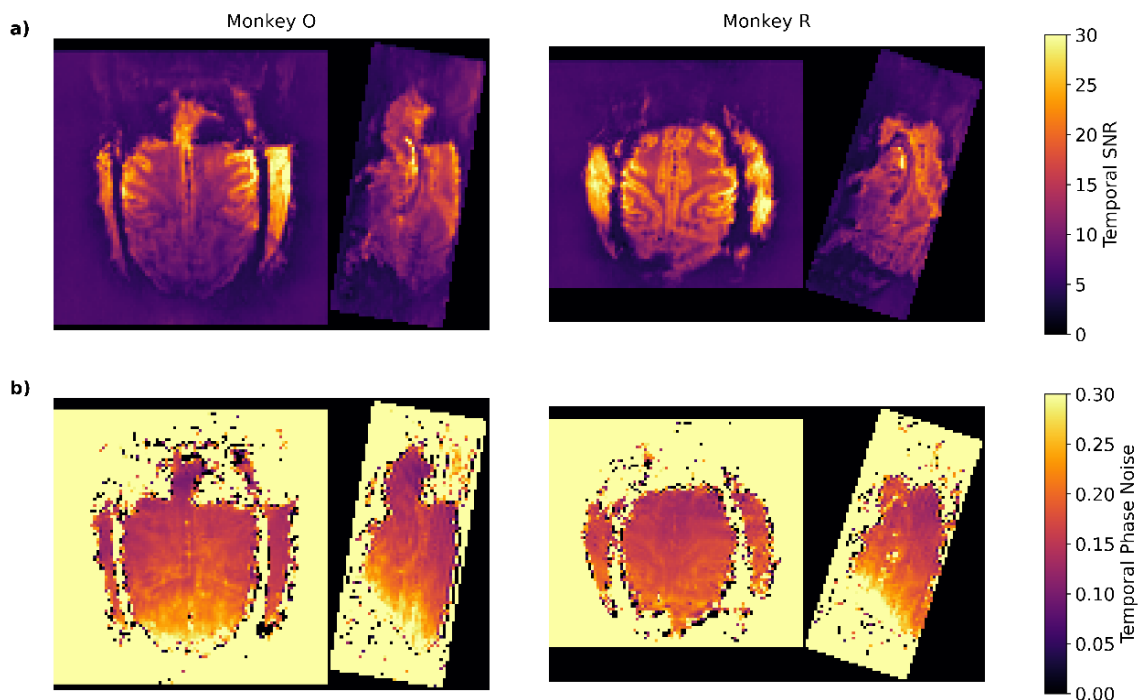
Figure 4.12: Magnitude and Phase Quality in Native EPI Space. Average **a)** magnitude temporal SNR and **b)** phase temporal standard deviation across all runs for

each animal. Subject O had previous surgery near the frontal eye fields causing anterior dropout.

To determine if the images and experimental setup was sufficient for resting state analysis the magnitude images were seeded at PGm, F1 and MT seeds and then visually compared against known connectivity areas for those seeds (Figure 4.2). All seeds showed expected connectivity and therefore it was concluded that the magnitude data was of sufficient quality for resting state analysis. Subject O has less statistically significant connectivity as expected because less resting state data was collected.
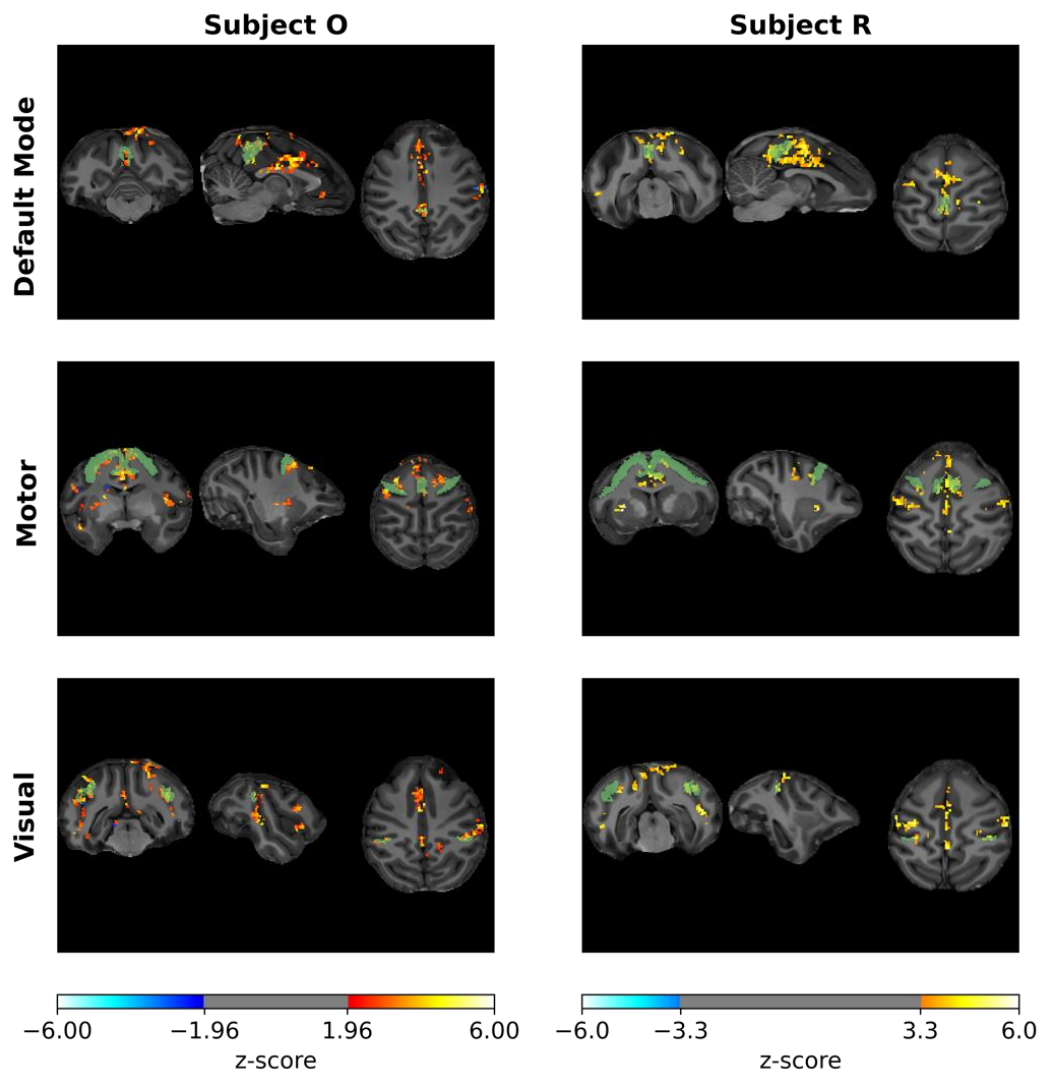
Figure 4.13: Seed analysis: Both subjects, GE-EPI only. Connectivity shown after one sided t-test with a false positive rate specific to that subject's signal strength and clustering of 10. Seed regions are shown in green. Top Row: Default mode seed (PGm),

Middle Row: Motor Seed (F1), Bottom Row: Visual Seed (MT). Subject O (alpha=0.05), Subject R (alpha=0.001). Connectivity maps are projected in anatomical space using nearest-neighbour interpolation.

4.3.2   Power Spectrum Analysis

To examine temporal properties of the magnitude and phase data, the power spectra for each run were plotted after preprocessing. These are the input signals in the post-PR cleaning case. The preprocessed magnitude power spectra (Figure 4.3a) and phase power spectra (Figure 4.3b) show physiological signal contamination in several ways. First, a physiological peak can be seen around 0.35-0.45 Hz in the phase spectra for both subjects and is also present, though less pronounced, in the magnitude data. Second, a peak at 0.2 Hz can be seen in the phase and magnitude data, likely system noise due to it its sharp definition and identical presentation in both subjects. Previous studies have observed such a peak caused by the cold heads of the magnet system [20]. Finally, in the phase spectra (Figure 4.3b), physiological aliasing can be observed for subject R between 0.1 and 0.2 Hz. Assessing these spectra quantitatively (Figure 4.3c) enables comparison of the average power in each band for the magnitude and phase data. The magnitude data have an average power of 1.90 ± 0.09 (mean $\pm$ standard dev.) in the signal band (0.1-0.01 Hz) and 1.99 ± 0.02 in the noise band (> 0.15 Hz). In contrast, the phase data have an average power of 0.7 ± 0.2 in the signal band and 2.24 ± 0.03 in the noise band. These averages mean that in the post-PR cleaning case the phase data has over three times more power in the noise band than the signal band, showing that the phase data is heavily noise-dominated, and identification and correction of these noise sources will be necessary for PR to work properly as a macrovascular filter. This is especially an issue in the post-PR cleaning case as the data is not bandpass filtered prior to fitting.

The power spectra were also plotted for magnitude (Figure 4.3d) and phase (Figure 4.3e) after nuisance regression which allows for exploration of the power in the signal and noise bands of the pre-PR case. The artifactual signal peaks observed above are not completely suppressed in either magnitude or phase, although they are reduced

across both subjects. When comparing these signals quantitatively (Figure 4.3f), the magnitude data have an average power of 2.02 ± 0.03 (mean ± standard dev.) in the signal band and 1.96 ± 0.01 in the noise band. In contrast the phase data have an average power of 1.6 ± 0.2 in the signal band and 2.05 ± 0.03 in the noise band. The pre-PR cleaning reduces the noise power of the phase to 1.28 times the power in the signal band but shows that even the pre-PR case is not completely removing physiological confounds in the noise band of the phase (Figure 4.3e). This incomplete signal cleaning can be expected to affect the PR fit as this noise band is used for estimation of the uncertainty of magnitude and phase.
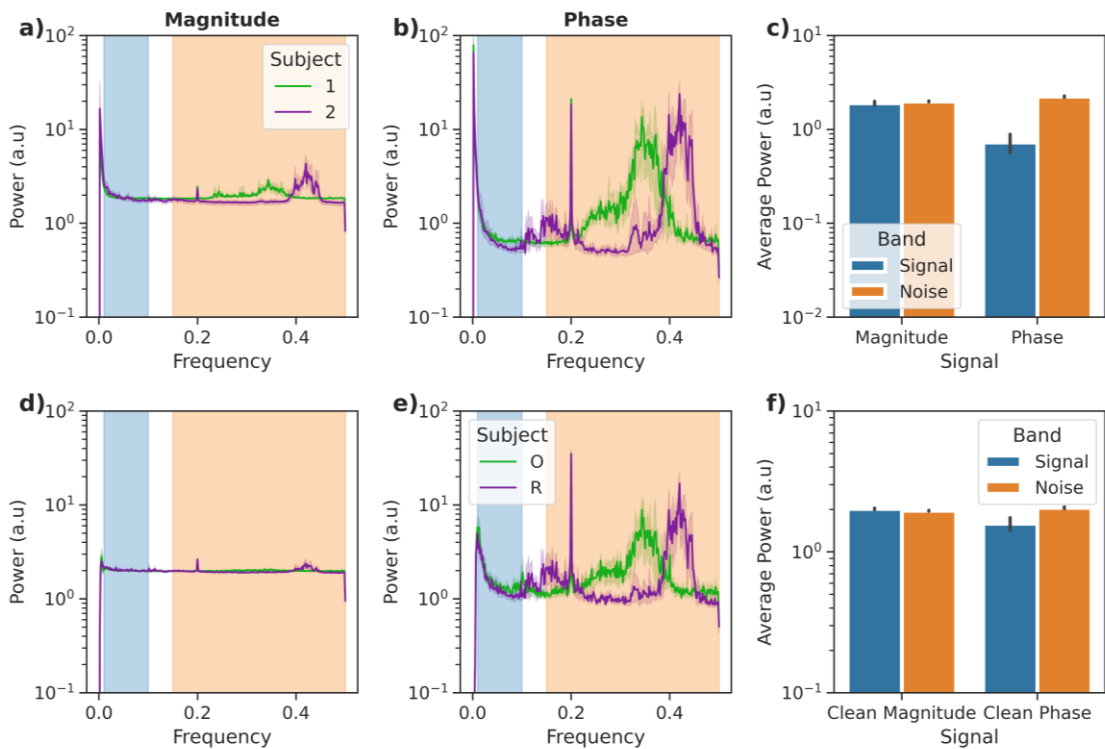
Figure 4.14: Power spectrum analysis. Blue shading represents the signal band (0.01-0.1 Hz) and orange, the noise band (> 0.15 Hz). Top Row: Post-PR cleaned data. The full power spectrum is used to perform PR and the noise is estimated from the orange noise band. Bottom Row: Pre-PR data (d-f), only the signal band frequencies are used for PR and noise is estimated from the orange noise band. a) Magnitude power spectra and b) phase power spectra across all voxels in the D99 atlas for the post-PR case. Coloured lines represent different subjects and shaded error is the 90% confidence interval of the mean across runs. c) Comparison of average power in the signal band and noise bands averaged across runs and subjects for the post-PR case. d) Magnitude power spectra and e) phase power spectra across all voxels in the D99 atlas for the pre-PR case. f)

Comparison of average power in the signal band and noise bands averaged across runs and subjects for the pre-PR case. Error bar is the standard deviation across runs and subjects.

Further investigation of the different noise sources was completed in Subject R through manual identification of the different noise bands (Figure 4.4a and b) and plotting the relative power in those signal bands across space. The data used was not physiologically cleaned prior to this analysis. First, the signal band (0.01-0.1 Hz) shows uniform power across the magnitude data (Figure 4.4c) but not the phase data (Figure 4.4d). Second, the peak at 0.2 Hz seen in the phase data shows some slice dependence towards the anterior of the brain, as would be expected if the peak were a system artifact (Figure 4.4f). The 0.2 Hz peak does not show any spatial pattern in the magnitude data (Figure 4.4e). The smaller amplitude physiology band from 0.3-0.38 Hz is most likely pulsation-based cardiac signal as it is most present in voxels around the brain and in ventricles in the phase data (Figure 4.4h) [42] and shows no specific pattern in the magnitude data (Figure 4.4g). The largest noise source in the magnitude (Figure 4.4i) and phase data (Figure 4.4j) appears to be coming from mass motion field shifts due to respiration (0.38 – 0.45 Hz). This artifact was identified as a mass motion artifact because of the increased relative power in the posterior of the brain, closer to the lungs, in the phase signal as well as by the frequency of the noise source. The uniformity of the signal leads to the conclusion it is caused by mass motion and not by respiratory induced changes in blood oxygenation which would have similar spatial behaviour to the smaller physiological signal (Figure 4.4i).
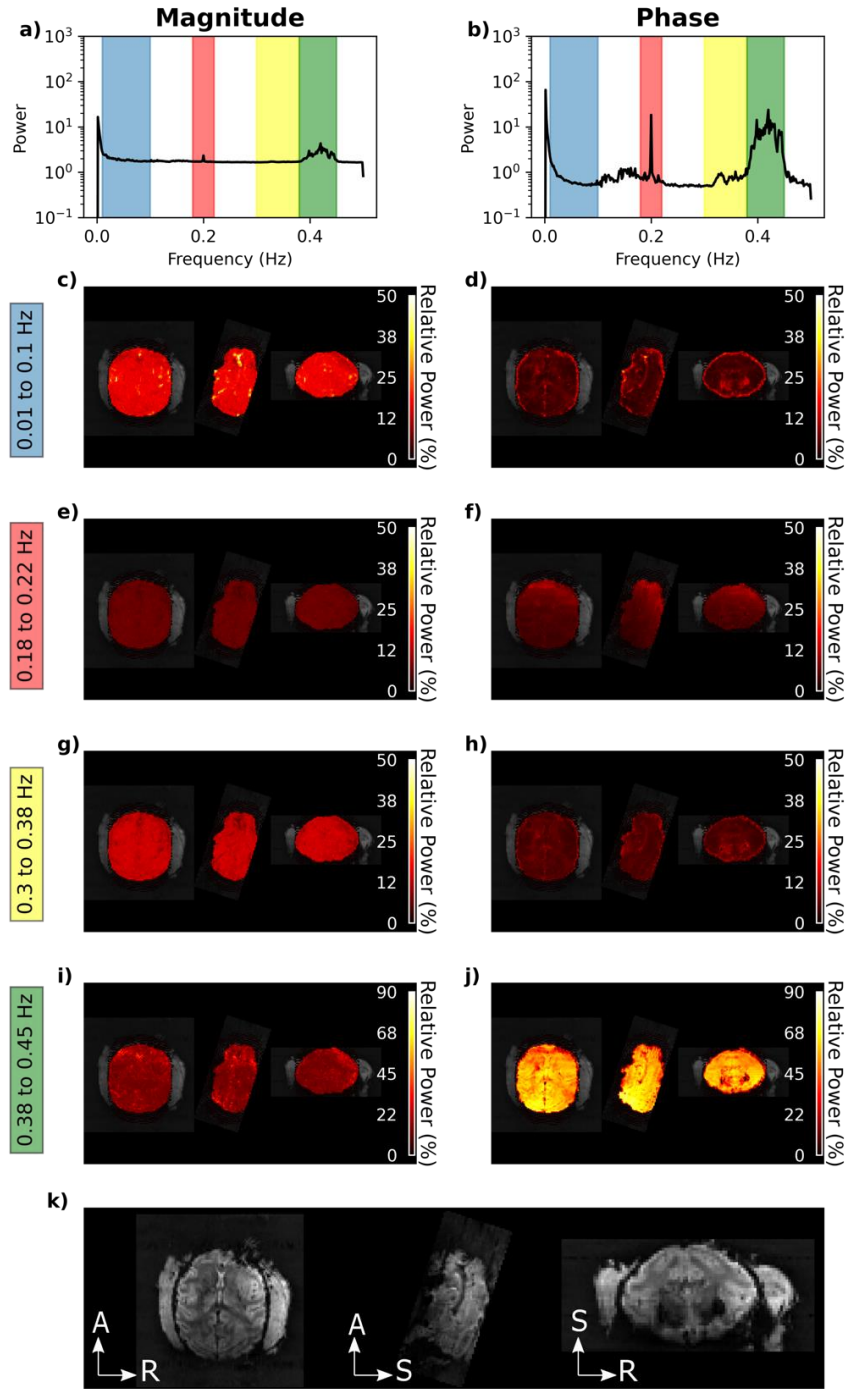
Figure 4.15: Noise Band Identification for Subject R. Average power spectra and noise bands for a) magnitude and b) phase time series. Relative power in the signal band (0.01 to 0.1 Hz) in c) magnitude and d) phase time series. Relative power from 0.18 to 0.22 Hz, cold head artifact, in e) magnitude and f) phase time series. Relative power from 0.3 to 0.38, cardiac signal, in g) magnitude and h) phase time series. Relative power from 0.38 to 0.45 Hz, mass motion field shifts from respiration, in i) magnitude and j) phase time series. k) EPI image for reference.

4.3.3   Resting State Activity in PR Timeseries

Seed analysis reveals the connectivity before and after the PR fit, as well as the connectivity in the estimated macrovascular time course that is removed. Three seeds were selected: one parietal (PGm), one in the primary motor area (F1), and one in a visual area (MT). General linear models were used to conduct seed-analyses, and connected areas were tested by using a one-sample t-test. In the post-PR cleaning case (Figure 4.5), seed analysis shows that the PR is not suppressing signal in veins alone. In fact, GE-EPI (Figure 4.5a) vs GE-EPI-PR (Figure 4.5b) show only minor differences in the resultant connectivity maps across all three seeds. Examining the image without the statistical threshold reveals the only visible change was a general increase in noise in the GE-EPI-PR case (Figure 4.6). This increase is expected as PR reduces contrast-to-noise ratio during application due to the inclusion of the noisier phase data in the resultant timeseries [8]. If PR were correctly removing macrovasculature as intended the estimated macrovasculature seeds should be activated near veins but this is not the case (Figure 4.5c). The negligible difference between GE-EPI and GE-EPI-PR paired with the unexpected pattern in the estimated macrovasculature in the post-PR cleaning case appears to suggest PR fitting is dominated by the artifacts in the data (Figure 4.3a and b) and not the resting state BOLD signal.
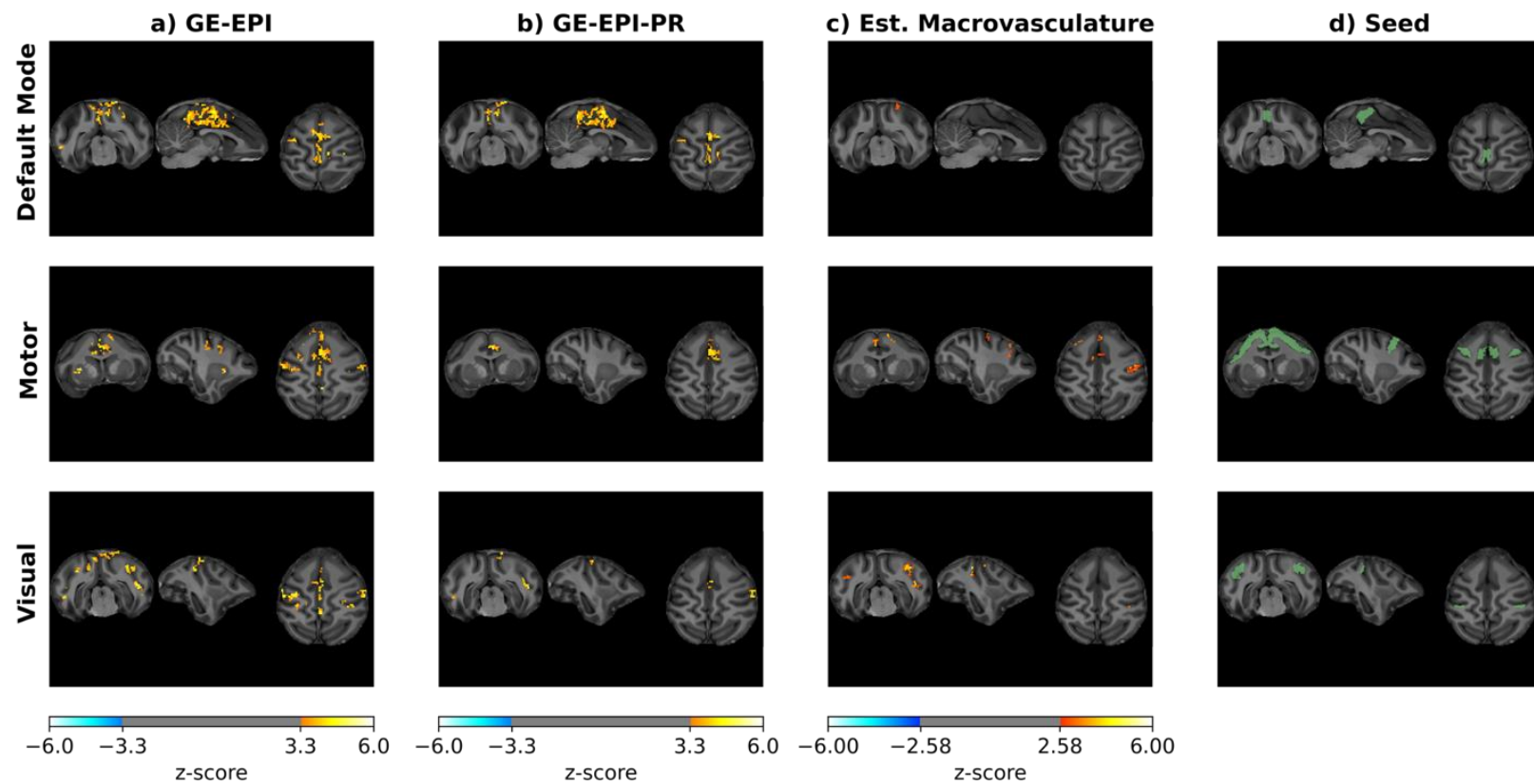
Figure 4.16: Seed analysis: Post-PR Physiological Cleaning Case. Top Row: Default mode seed (PGm), Middle Row: Motor Seed (F1), Bottom Row: Visual Seed (MT). a) GE-EPI connectivity maps, b) GE-EPI-PR connectivity maps, c) estimated macrovasculature signal connectivity maps, d) seed regions are shown in green. Connectivity maps are projected in anatomical space using nearest-neighbour interpolation. In columns a and b, connectivity is shown after a one-sided t-test with a 0.1% false positive rate for a cluster size of 10. Due to low connectivity in the macrovascular images, they are thresholded with a false positive rate of 1% and a cluster size of 10.
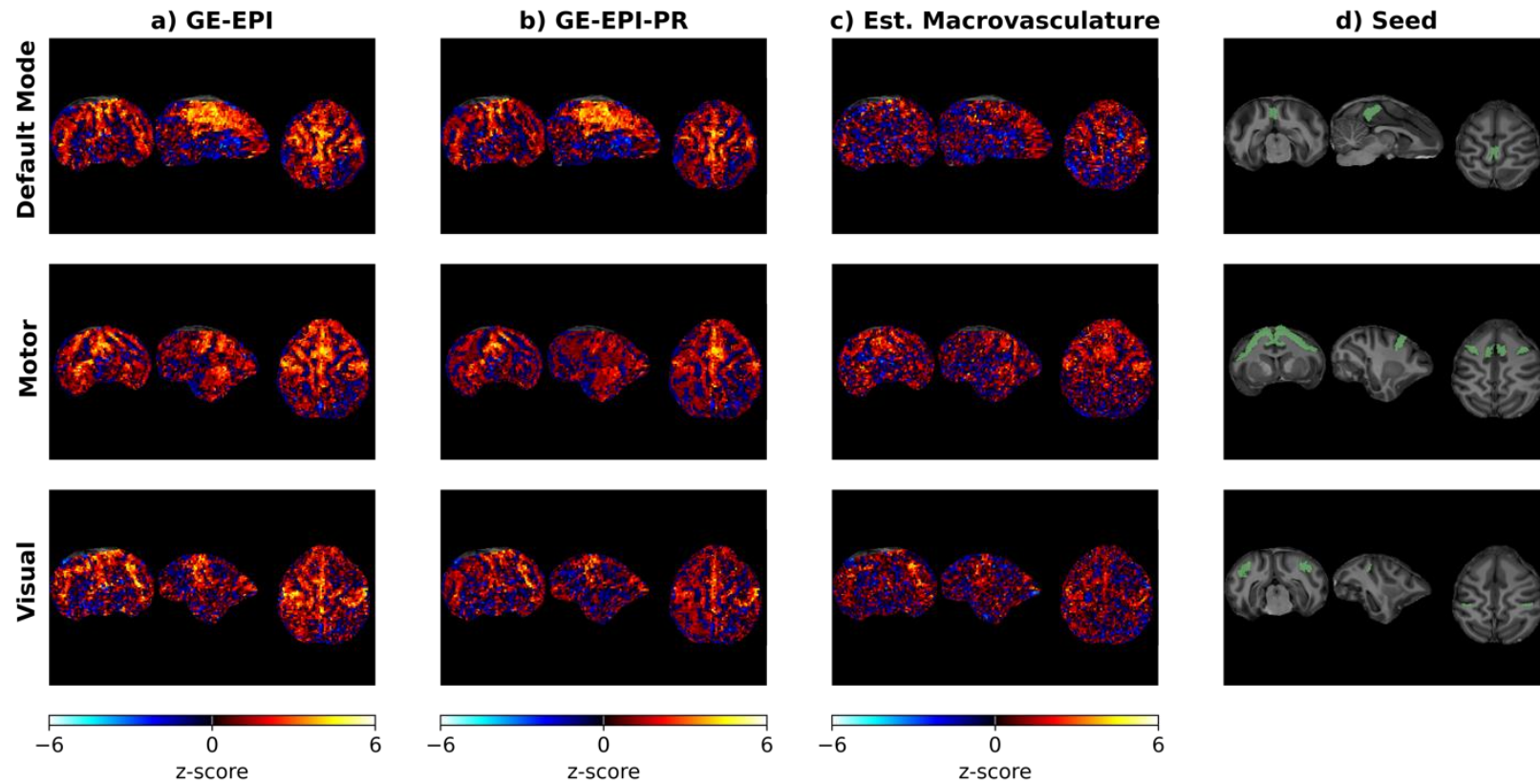
Figure 4.17: Seed analysis: Post-PR Physiological Cleaning Case, no thresholding. Top Row: Default mode seed (PGm), Middle Row: Motor Seed (F1), Bottom Row: Visual Seed (MT). a) GE-EPI connectivity maps, b) GE-EPI-PR connectivity maps, c) estimated macrovasculature signal connectivity maps, d) seed regions are shown in green. Connectivity maps are projected in anatomical space using nearest-neighbour interpolation. Connectivity shown after one sided t-test.

Figure 4.7 shows the same seed analysis performed in the case of pre-PR physiological cleaning. In the pre-PR cleaning case, functional connectivity from each of the respective seeds in the GE-EPI-PR case is extremely suppressed (all seeds, Figure 4.7b). In accordance with this observation, the estimated macrovascular connectivity (Figure 4.7c) matches functional connectivity in the GE-EPI case (Figure 4.7a). Together, these two observations suggest that the noise estimates for PR are inaccurate due to the remaining presence of physiological noise. In ODR as the ratio of the signal variances, $\frac{\sigma_{\varepsilon}^2}{\sigma_{\eta}^2}$, approaches 0 the regression becomes an ordinary least squares regression with the dependent and independent variables switched and this may be what is occurring here. This suppression demonstrates a limitation of PR as it relies on robust physiological denoising to reliably remove the artifacts for improved fitting. Taken together these two cleaning cases present two extremes of physiological correction and show that in either case PR does not perform optimally.
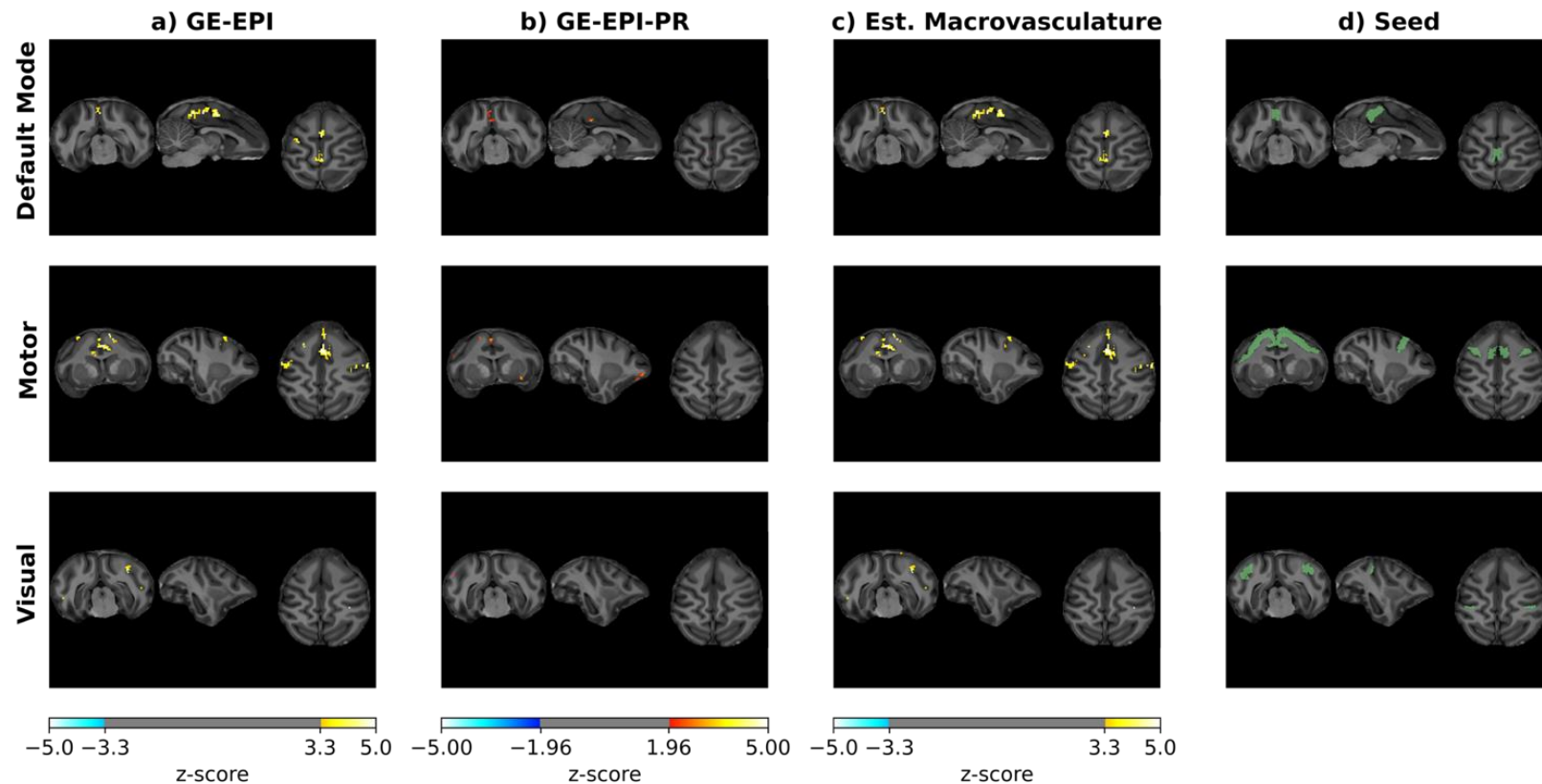
Figure 4.18: Seed analysis: Pre-PR Physiological Cleaning Case. Top Row: Default mode seed (PGm), Middle Row: Motor Seed (F1), Bottom Row: Visual Seed (MT). a) GE-EPI connectivity maps, b) GE-EPI-PR connectivity maps, c) estimated macrovasculature signal connectivity maps, d) seed regions are shown in green. Connectivity maps are projected in anatomical space using nearest-neighbour interpolation. In columns a and c, connectivity is shown after a one-sided t-test with a 0.1% false positive rate for a cluster size of 10. Due to low connectivity in the GE-EPI-PR images they are thresholded with a false positive rate of 5% and a cluster size of 1

Next, we investigated the effects of PR on whole brain functional connectivity matrices generated from the D99 macaque atlas (Figure 4.8). These results show an identical pattern to the seed analysis where cleaning after PR added noise to the resultant series and cleaning before PR caused complete suppression of the resting state signal in the microvascular image. In the post-PR cleaning case, there was no overall significant change in connectivity (aka the mean of the connectivity matrix did not change between GE-EPI and GE-EPI-PR) and there were no individual significantly different connections across runs (pairwise t-test with 5% false discovery rate correction). In the pre-PR cleaning case, there was an overall decrease in connectivity of -0.04 ± 0.03 when comparing GE-EPI-PR to GE-EPI and 2267 of the 18721 individual connections were found to be significant (pairwise t-test across runs with 5% false discovery rate correction). Significant connections are shown in Figure 4.9. This shows that whether physiological cleaning is applied before or after PR can greatly alter performance of the technique across the whole brain. When it is applied after PR the method has no significant effect on the resting state data and when it is applied before it is completely suppressing the data similarly to what was seen in the seeds in Figure 4.5.
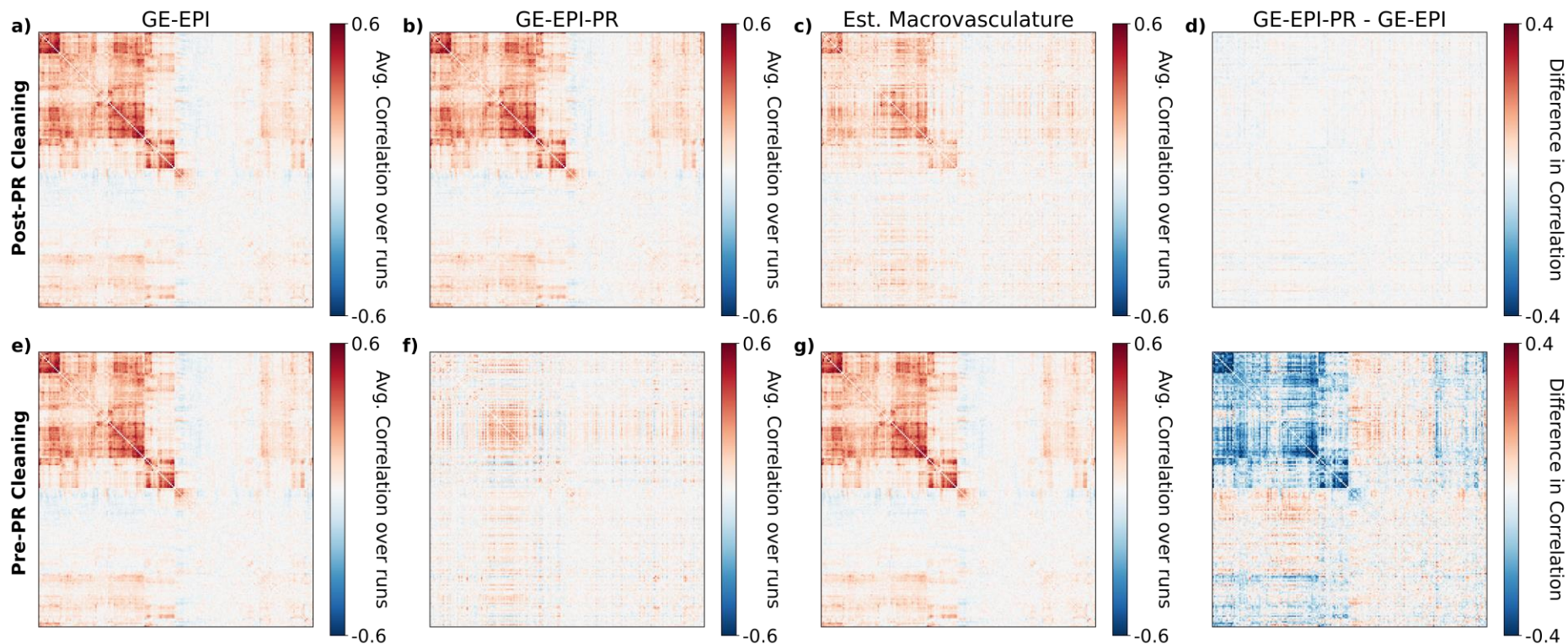
Figure 4.19: Whole brain connectivity analysis. Top Row: Post-PR Cleaning, Bottom Row: Pre-PR Cleaning. All connectivity matrices are ordered by clustering the GE-EPI timeseries with post-PR cleaning. a) GE-EPI connectivity matrix, b) GE-EPI-PR connectivity matrix ($M - (A\varphi + B)$), c) estimated macrovasculature ($A\varphi + B$) and d) connectivity difference between GE-EPI-PR and GE-EPI.
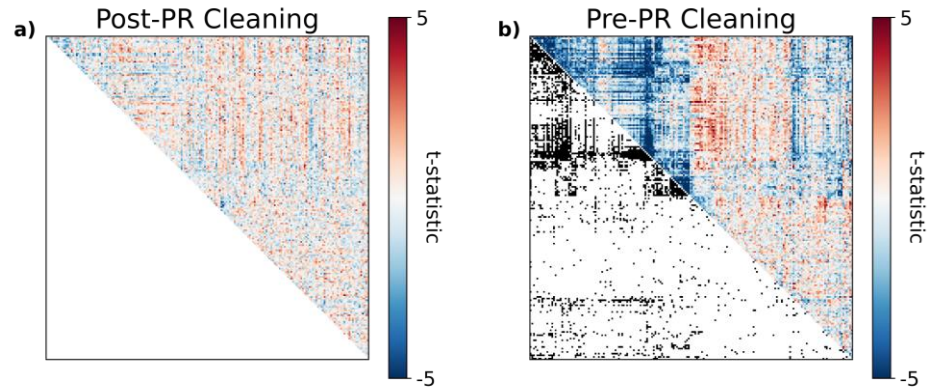
Figure 4.20: Resting-state functional connectivity analysis of different denoising strategies with PR. The upper triangle is the t-statistic from the pairwise t-test for differences between GE-EPI-PR and GE-EPI across runs and subjects and the lower triangle is whether that connectivity is significantly different between GE-EPI and GE-EPI-PR (5% false discovery rate correction). a) post-PR cleaning had no significant correlations and b) pre-PR cleaning had 2267 significant correlations and showed a large reduction in connectivity.

4.4   Discussion

4.4.1   Summary

This study investigated the use of PR in a macaque model for the first time. Macaques are a common target for laminar fMRI experiments [12–14,43] and thus it was our interest to see if the PR technique could be expanded to macaques to increase spatial specificity in that model. We collected resting state data from two female macaques over 60 and 100 minutes respectively. This data was examined to determine power spectra features and signal properties. Two main sources of noise were found, respiratory mass motion field shifts, and a system oscillation related to the cold heads. PR was performed under two different physiology cleaning strategies: with physiological cleaning after and prior-to PR. The efficacy of PR under the two methods were assessed two ways, by looking at seeds in the motor, visual and parietal areas and by examining primate connectivity using the D99 atlas. Both seed connectivity and whole brain connectivity analyses provided supporting evidence to show that the PR technique could not tease

apart resting state activity into micro- and macro-vascular components in this data. Specifically, these cleaning methods resulted in over-filtering of resting state signal when the data was cleaned prior to PR, whereas cleaning the data after PR only decreased contrast to noise ratio. This study shows that two important considerations must be accounted for when performing PR for macaque resting-state fMRI experiments. First, care must be taken to ensure the phase data collected has a low amount of phase noise in it. This noise can drive the PR fit in an undesirable way and may not be easily removable post-acquisition. Second, PR in a macaque model must consider the proximity of the lungs which are a major source of non-neurovascular phase noise due to mass motion field shifts from respiration. Future work will have to incorporate corrections for these breathing effects [22].

4.4.2   Phase noise can interfere with phase regression performance

Phase noise is a considerable confound in PR and care must be taken to reduce its affects. Figure 4.3 shows that there is more high frequency noise in the phase data than the magnitude data in both subjects. The main source of noise is structured with power concentrated at 0.3-0.45 Hz meaning it is physiological in origin [38]. Additionally, the phase noise has a single peak at 0.2 Hz which is believed to be related to the MRI system and has previously been associated with cold heads [20]. Together, these sources of noise present issues in both the post- and pre-PR cleaning cases (Figures 4.5 and 4.7). In the post-PR cleaning case, the noise power is approximately three times the signal power and is the principal driver of the PR regression. In the ideal case the macrovascular BOLD signal would drive the regression by causing phase changes in large vessels (Figure 4.3c). Alternatively, the pre-PR case uses noise with physiological signal in it (Figure 4.3e) for signal error estimation resulting in a fit that completely suppresses the GE-EPI-PR signal (Figure 4.7). This means that mitigating noise at the time of experimentation is key to performing PR in the macaque model successfully.

4.4.3   PR in macaques must consider the effects of respiration

The main noise peak is respiratory in origin (Figure 4.4) and occurs due to mass motion field shifts from respiration [18] (Figure 4.4i). This is mostly due to animal geometry, as being in the sphinx position puts the macaque's lungs at greater proximity to the imaging region than in previous PR studies where a human was imaged in the head-first supine position [28]. This is an issue as phase data is susceptible to respiratory contamination in two ways, of which, only one maintains the phase signal's specificity to neurovascular signal changes in large vessels. Firstly, respiration artifacts could lead to effects in BOLD contrast as the oxygen levels in the blood change. PR would correct this and still cause macrovascular suppression as these respiratory BOLD effects would correlate in magnitude and phase in large vessels. The second effect respiration could cause is respiration induced mass motion field shifts which result in global intensity changes across the whole brain. These were observed in this experiment and are most dominant in phase data but are present in magnitude as well (Figure 4.4i and j). As these respiratory artifacts are global across the brain and are not neurovascular in origin, they prevent any macrovascular reduction until they are removed from both timeseries. In this data they could not be completely removed with CompCor and as a result PR did not work as expected. In this case the method is performing similarly to the studies that use PR for correction of mass motion [26,27]. Possible avenues to correct this could include DORK, an on-system correction for the physiological drift of the central k-space [22] or removal of the respiratory timeseries through RETROICOR [39].

4.4.4   Implication for the application of phase regression

This work highlights several important considerations about PR that must be considered when using it to reduce signal from draining veins. First, signal to noise ratio and phase variance over time are not adequate measures of signal integrity to check across a volume to ensure quality phase signal (Figure 4.1). Power spectrum analysis should be used to examine for temporal confounds and ensure signal integrity after physiological cleaning (Figure 4.3). It is important to obtain a signal with low phase noise from the initial pilot experiment as it is not always possible to recover this signal with

post processing methods (Figures 4.5 and 4.7). These three points have implications for all future studies of macaques but also provide helpful tools for future studies of phase regression in humans. Power spectra should be an important part of future PR quality assurance regardless of the species imaged.

Additionally, this study illustrates several points related to the implementation of PR in macaques. To this author's knowledge this is the first study to attempt PR in a sedated macaque model. Sedation is an important consideration as it can cause heavier breathing and deeper breaths in the macaques which can increase the chance of mass motion field shift artifacts from respiratory motion. This occurred in our data (Figure 4.4j) and is most likely due to the proximity of the macaque lungs to the imaging region compared to a human. This will be a potential issue for any animal imaged in sphinx position and on-system correction for these artifacts will be needed for these studies moving forward [22].

4.4.5 Study limitations

As this is a primate study, animal numbers are kept as low as possible. This work examined two macaques, and this limits the ability to create group statistics and all effects are measured across runs. This number was appropriate for a pilot study to investigate the effectiveness of PR at macrovascular suppression in a macaque model. One limitation of this pilot is that reliable collection of physiological data was not possible with the physiological recorder synced to the MRI system as it was not optimized for primate skin pigment. This meant it was not possible to examine the effects of RETROICOR on phase cleaning [23,39] as the approach has previously been successful in humans. Finally, this study was also performed using a resting state paradigm. This paradigm has no specific activation pattern to study and is more variable in its interpretation than a task-based paradigm. Previous work completed in humans on PR for the correction of mass motion artifacts has used tasks as it is possible to directly map the amount of spurious activation corrected [27] or the increase in t-statistics [26]. Using a task-based approach would allow for greater optimization of PR for macaques.

Due to the increasing reliability of task-based research in awake macaques [12,44,45], this research should be continued with an awake paradigm and a reliable task.

4.4.6   Future Work

Three possible ways to improve this work in future would be to first, perform the work again with physiological traces to allow for direct determination of heart rate and breathing effects. Second, this experiment could examine different PR fit methods that have been published over the past 20 years to examine their efficacy in the high noise regime. PR with Savitsky-Golay filtering has demonstrated a per voxel data-driven cleaning that has reduced physiological effects in humans with a task-based experiment [10]. Third, given the size of the mass motion artifact, an on-system physiological correction such as DORK would be advised. More investigation is required to implement phase regression as a macrovascular filter in a macaque model.

In the introduction, it was proposed, that the macaque would be a good candidate for studying PR effects on the cortical orientation dependence of the BOLD signal. Given the current challenges observed with macaques and PR, a cortical orientation study would be better performed in humans at a future date [16]. Compared to the results shown here, human phase data exhibits less noise as respiration effects are smaller due to the differing position and geometry of the subject in the magnet [8,11].

4.5   Conclusions

PR has shown promise in cleaning of BOLD signal in humans in both task and resting state. Given the utility of macaques in laminar studies, this study attempted to extend PR to the macaque animal model. Unfortunately, excess phase noise from non-neurovascular sources such as breathing and system noise in the phase timeseries means PR was not effective at performing macrovascular suppression in this experiment. Future work should investigate correction for these noise sources using DORK or RETROICOR.

4.6   References

1. Ogawa S, Menon RS, Tank DW, Kim SG, Merkle H, Ellermann JM, et al. Functional brain mapping by blood oxygenation level-dependent contrast magnetic resonance imaging. A comparison of signal characteristics with a biophysical model. Biophys J. 1993;64: 803–812. doi:10.1016/S0006-3495(93)81441-3

2. Poldrack RA. The future of fMRI in cognitive neuroscience. NeuroImage. 2012;62: 1216–1220. doi:10.1016/j.neuroimage.2011.08.007

3. Hutchison RM, Everling S. Monkey in the middle: why non-human primates are needed to bridge the gap in resting-state investigations. Front Neuroanat. 2012;6. doi:10.3389/fnana.2012.00029

4. Logothetis NK, Pauls J, Augath M, Trinath T, Oeltermann A. Neurophysiological investigation of the basis of the fMRI signal. Nature. 2001;412: 150–157. doi:10.1038/35084005

5. Ogawa S, Lee TM, Kay AR, Tank DW. Brain magnetic resonance imaging with contrast dependent on blood oxygenation. Proc Natl Acad Sci U S A. 1990;87: 9868–9872. doi:10.1073/pnas.87.24.9868

6. Menon RS. The great brain versus vein debate. NeuroImage. 2012;62: 970–974. doi:10.1016/j.neuroimage.2011.09.005

7. Menon RS. Postacquisition suppression of large-vessel BOLD signals in high-resolution fMRI. Magn Reson Med. 2002;47: 1–9. doi:10.1002/mrm.10041

8. Stanley OW, Kuurstra AB, Klassen LM, Menon RS, Gati JS. Effects of phase regression on high-resolution functional MRI of the primary visual cortex. NeuroImage. 2021;227: 117631. doi:10.1016/j.neuroimage.2020.117631

9. Vu AT, Gallant JL. Using a novel source-localized phase regressor technique for evaluation of the vascular contribution to semantic category area localization in BOLD fMRI. Front Neurosci. 2015;9. doi:10.3389/fnins.2015.00411

10. Barry RL, Gore JC. Enhanced phase regression with savitzky-golay filtering for high-resolution BOLD fMRI. Hum Brain Mapp. 2014;35: 3832–3840. doi:10.1002/hbm.22440

11. Curtis AT, Hutchison RM, Menon RS. Phase based venous suppression in resting-state BOLD GE-fMRI. NeuroImage. 2014;100: 51–59. doi:10.1016/j.neuroimage.2014.05.079

12. Chen G, Wang F, Gore JC, Roe AW. Layer-specific BOLD activation in awake monkey V1 revealed by ultra-high spatial resolution functional magnetic resonance imaging. NeuroImage. 2013;64: 147–155. doi:10.1016/j.neuroimage.2012.08.060

13. Goense J, Merkle H, Logothetis NK. High-Resolution fMRI Reveals Laminar Differences in Neurovascular Coupling between Positive and Negative BOLD Responses. Neuron. 2012;76: 629–639. doi:10.1016/j.neuron.2012.09.019

14. Goense JBM, Logothetis NK. Laminar specificity in monkey V1 using high-resolution SE-fMRI. Magn Reson Imaging. 2006;24: 381–392. doi:10.1016/j.mri.2005.12.032

15. Klassen L, Menon RS. BOLD signal phase and magnitude dependence on vessel geometry. Proceedings of the 13th International Society for Magnetic Resonance in Medicine Annual Meeting. Miami, FL; 2005.

16. Viessmann O, Scheffler K, Bianciardi M, Wald LL, Polimeni JR. Dependence of resting-state fMRI fluctuation amplitudes on cerebral cortical orientation relative to the direction of B0 and anatomical axes. NeuroImage. 2019;196: 337–350. doi:10.1016/j.neuroimage.2019.04.036

17. Hutchison RM, Hutchison M, Manning KY, Menon RS, Everling S. Isoflurane induces dose-dependent alterations in the cortical connectivity profiles and dynamic properties of the brain's functional architecture. Hum Brain Mapp. 2014;35: 5754–5775. doi:10.1002/hbm.22583

18. Brosch JR, Talavage TM, Ulmer JL, Nyenhuis JA. Simulation of human respiration in fMRI with a mechanical model. IEEE Trans Biomed Eng. 2002;49: 700–707. doi:10.1109/TBME.2002.1010854

19. Hagberg GE, Bianciardi M, Brainovich V, Cassarà AM, Maraviglia B. The effect of physiological noise in phase functional magnetic resonance imaging: from blood oxygen level-dependent effects to direct detection of neuronal currents. Magn Reson Imaging. 2008;26: 1026–1040. doi:10.1016/j.mri.2008.01.010

20. Hagberg GE, Bianciardi M, Brainovich V, Cassara AM, Maraviglia B. Phase stability in fMRI time series: effect of noise regression, off-resonance correction and spatial filtering techniques. NeuroImage. 2012;59: 3748–3761. doi:10.1016/j.neuroimage.2011.10.095

21. Rauscher A, Sedlacik J, Barth M, Mentzel H-J, Reichenbach JR. Magnetic susceptibility-weighted MR phase imaging of the human brain. AJNR Am J Neuroradiol. 2005;26: 736–742.

22. Pfeuffer J, Van de Moortele P-F, Ugurbil K, Hu X, Glover GH. Correction of physiologically induced global off-resonance effects in dynamic echo-planar and spiral functional imaging. Magn Reson Med. 2002;47: 344–353. doi:10.1002/mrm.10065

23. Petridou N, Schäfer A, Gowland P, Bowtell R. Phase vs. magnitude information in functional magnetic resonance imaging time series: toward understanding the noise. Magn Reson Imaging. 2009;27: 1046–1057. doi:10.1016/j.mri.2009.02.006

24. Yetkin FZ, Haughton VM, Cox RW, Hyde J, Birn RM, Wong EC, et al. Effect of motion outside the field of view on functional MR. AJNR Am J Neuroradiol. 1996;17: 1005–1009.

25. Birn RM, Bandettini PA, Cox RW, Jesmanowicz A, Shaker R. Magnetic field changes in the human brain due to swallowing or speaking. Magn Reson Med. 1998;40: 55–60. doi:10.1002/mrm.1910400108

26. Barry RL, Williams JM, Klassen LM, Gallivan JP, Culham JC, Menon RS. Evaluation of preprocessing steps to compensate for magnetic field distortions due to body movements in BOLD fMRI. Magn Reson Imaging. 2010;28: 235–244. doi:10.1016/j.mri.2009.07.005

27. Martin RE, MacIntosh BJ, Smith RC, Barr AM, Stevens TK, Gati JS, et al. Cerebral areas processing swallowing and tongue movement are overlapping but distinct: a functional magnetic resonance imaging study. J Neurophysiol. 2004;92: 2428–2443. doi:10.1152/jn.01144.2003

28. Gilbert KM, Gati JS, Barker K, Everling S, Menon RS. Optimized parallel transmit and receive radiofrequency coil for ultrahigh-field MRI of monkeys. NeuroImage. 2016;125: 153–161. doi:10.1016/j.neuroimage.2015.10.048

29. Moeller S, Yacoub E, Olman CA, Auerbach E, Strupp J, Harel N, et al. Multiband multislice GE-EPI at 7 tesla, with 16-fold acceleration using partial parallel imaging with application to high spatial and temporal whole-brain fMRI. Magn Reson Med. 2010;63: 1144–1153. doi:10.1002/mrm.22361

30. Stanley OW, Menon RS, Klassen LM. Phase sensitive receiver combination using prescan singular value decomposition derived receiver sensitivities. Proceedings of the 27th International Society for Magnetic Resonance in Medicine Annual Meeting. Paris, France; 2018.

31. Reveley C, Gruslys A, Ye FQ, Glen D, Samaha J, E. Russ B, et al. Three-Dimensional Digital Template Atlas of the Macaque Brain. Cereb Cortex N Y NY. 2017;27: 4463–4477. doi:10.1093/cercor/bhw248

32. Cox RW. AFNI: software for analysis and visualization of functional magnetic resonance neuroimages. Comput Biomed Res Int J. 1996;29: 162–173. doi:10.1006/cbmr.1996.0014

33. Lohmeier J, Kaneko T, Hamm B, Makowski MR, Okano H. atlasBREX: Automated template-derived brain extraction in animal MRI. Sci Rep. 2019;9: 12219. doi:10.1038/s41598-019-48489-3

34. Avants BB, Tustison NJ, Wu J, Cook PA, Gee JC. An open source multivariate framework for n-tissue segmentation with evaluation on public data. Neuroinformatics. 2011;9: 381–400. doi:10.1007/s12021-011-9109-y

35. Gorgolewski KJ, Esteban O, Ellis DG, Notter MP, Ziegler E, Johnson H, et al. Nipype: a flexible, lightweight and extensible neuroimaging data processing framework in Python. 0.13.1. Zenodo; 2017. doi:10.5281/zenodo.581704

36. Jenkinson M, Beckmann CF, Behrens TEJ, Woolrich MW, Smith SM. FSL. NeuroImage. 2012;62: 782–790. doi:10.1016/j.neuroimage.2011.09.015

37. Boggs PT, Spiegelman CH, Donaldson JR, Schnabel RB. A computational examination of orthogonal distance regression. J Econom. 1988;38: 169–201. doi:10.1016/0304-4076(88)90032-2

38. Behzadi Y, Restom K, Liau J, Liu TT. A Component Based Noise Correction Method (CompCor) for BOLD and Perfusion Based fMRI. NeuroImage. 2007;37: 90–101. doi:10.1016/j.neuroimage.2007.04.042

39. Glover GH, Li TQ, Ress D. Image-based method for retrospective correction of physiological motion effects in fMRI: RETROICOR. Magn Reson Med. 2000;44: 162–167. doi:10.1002/1522-2594(200007)44:1<162::aid-mrm23>3.0.co;2-e

40. Wang S, Peterson DJ, Gatenby JC, Li W, Grabowski TJ, Madhyastha TM. Evaluation of Field Map and Nonlinear Registration Methods for Correction of Susceptibility Artifacts in Diffusion MRI. Front Neuroinformatics. 2017;11. doi:10.3389/fninf.2017.00017

41. Abraham A, Pedregosa F, Eickenberg M, Gervais P, Mueller A, Kossaifi J, et al. Machine learning for neuroimaging with scikit-learn. Front Neuroinformatics. 2014;8. doi:10.3389/fninf.2014.00014

42. Griffanti L, Douaud G, Bijsterbosch J, Evangelisti S, Alfaro-Almagro F, Glasser MF, et al. Hand classification of fMRI ICA noise components. NeuroImage. 2017;154: 188–205. doi:10.1016/j.neuroimage.2016.12.036

43. Self MW, van Kerkoerle T, Goebel R, Roelfsema PR. Benchmarking laminar fMRI: Neuronal spiking and synaptic activity during top-down and bottom-up processing in the different layers of cortex. NeuroImage. 2019;197: 806–817. doi:10.1016/j.neuroimage.2017.06.045

44. Goense JBM, Ku S-P, Merkle H, Tolias AS, Logothetis NK. fMRI of the temporal lobe of the awake monkey at 7 T. NeuroImage. 2008;39: 1081–1093. doi:10.1016/j.neuroimage.2007.09.038

45. Chen G, Wang F, Dillenburger BC, Friedman RM, Chen LM, Gore JC, et al. Functional magnetic resonance imaging of awake monkeys: some approaches for improving imaging quality. Magn Reson Imaging. 2012;30: 36–47.

5   Future Work

5.1   Summary

Phase regression is a method in which the underutilized phase of GE-EPI is used to reduce macrovascular signal to increase the spatial specificity of the BOLD effect. This thesis implemented phase regression at high resolution for the first time. This work outlines several key points that contribute to the growing field of phase regression research, especially when it is completed at high resolution.

First in Chapter 2, a coil combination method was developed that was targeted at combining large phase datasets. Multi-receiver RF arrays require coil sensitivity estimation to combine high quality phase images. This is a challenge at ultra-high fields such as 7T as the conventional technique of using a reference coil is not available due to the lack of body coils because of poor RF homogeneity and specific absorption rate constraints. Our proposed method, the fitted SVD method, used a voxel-wise SVD [1] of a routinely acquired prescan to calculate relative coil sensitivities. These relative sensitivities could then be extended to any imaging geometry using a fit to a polynomial basis. This allowed the fitted SVD method to combine data throughout the entire imaging session after the prescan was collected. We hypothesized that this combination method would provide images of sufficient quality to be useful for combining GE-EPI phase data. The fitted SVD method created a combination with 96% of the SNR when compared to the voxelwise SVD, our reference method. This was further explored in an EPI acquisition which showed that the fitted SVD method resulted in a low amount of phase noise and in a separate experiment showed a high resistance to motion.

This technique was applied in Chapter 3 where high-resolution GE-EPI and SE-EPI data was acquired at 800 µm isotropic resolution. The phase data was used to perform phase regression and create GE-EPI-PR time courses. The GE-EPI, SE-EPI, and GE-EPI-PR data was then compared across varying cortical surface depths as well as in laminar

profiles. When examined on a surface the GE-EPI-PR data showed a reduction in BOLD signal near vessels. The GE-EPI-PR data also showed a statistically similar distribution to SE-EPI in the upper half of the cortical sheet when using a Kolmogorov-Smirnov test. Additionally, this data showed that phase regression resulted in a flatter laminar profile than GE-EPI with a 1.8x higher contrast-to-noise ratio than SE-EPI. This means using phase regression for macrovascular reduction will result in data with a high statistical power. Taken together these results show that phase regression demonstrates valuable improvements to GE-EPI for laminar fMRI.

Chapter 4 piloted the phase regression technique in two sedated macaques undergoing resting state imaging at 1mm isotropic resolution. We hypothesized that phase regression could provide an increase in spatial specificity to resting state connectivity maps and remove any artifacts present in both the magnitude and phase data. This functional data was heavily contaminated by artifacts and so was not of sufficient quality to perform phase regression. These artifacts were identified as mass motion field shifts caused by subject's breathing as well as a system artifact previously tied by other groups to the MRI cold heads [2]. As these artifacts originated from non-neurovascular sources and dominated the fit, they prevented phase regression from operating as a macrovascular filter. Two different physiological cleaning regimes were used to correct this data but neither resulted in phase regression performing as a macrovascular filter. Several methods to prevent this in the future were discussed such as collecting physiological traces synced with the acquisition to attempt RETROICOR to clean the data [3] or implementing a navigator echo to allow for the correction of bulk field shifts at the center of k-space [4]. Further work will have to be undertaken to perform phase regression in a macaque to prevent contamination by breathing noise.

5.2   Thesis Limitations

5.2.1   Phase noise due to coil combination

The method designed in Chapter 2 resulted in combinations that had a 4% reduction in phase SNR. As this was significantly better than our default method at the time, complex sum, this posed great advantages and was used going forwards, but it

could be improved upon for future studies. Fitting of the sensitivities to a polynomial basis could be improved by using the Helmholtz solution, which is the true representation of the receive coil sensitivities [5]. However, this would include the wave number in fitting and would require modelling of the electric properties of the head [6]. Alternatively, combinations such as ASPIRE [7] or COMPOSER [8] with targeted prescans could be added to the imaging protocol. These applications combine the data with no noise increase but would extend scan length due to the need for the prescan. Our method proposed here also used a prescan, but it was integrated into the imaging protocol and so did not require added time.

5.2.2   Unknown effects of partial Fourier

Partial Fourier is always a concern in high resolution fMRI as it leads to signal blurring [9]. This could lead to signal bleeding across sulci or mixing signal from shallow or deep locations in the cortical sheet. Although all partial Fourier should be minimized, it remains crucial in order to obtain echo times at reasonable values [10]. Partial Fourier collects only a fraction of k-space, usually between 5/8 and 7/8, then uses conjugate symmetry to create the magnitude and phase images. This method has the assumption that phase at higher spatial frequencies is zero, an assumption that is known to be untrue generally, but is especially problematic during phase regression experiments. Additionally, there are many methods to perform partial Fourier such as zero-filling or homodyne reconstruction [11] and selecting the appropriate method is an open question. In Chapter 3, we selected zero-filling, so no assumptions were made about the uncollected phase data. The phase data did not show any expected artifacts of partial Fourier such as Gibbs's ringing and so it was considered sufficient for the analysis. However, the use of partial Fourier for phase regression applications is a remaining caveat in this research that requires fuller investigation at a future date.

5.2.3   Effects of physiological noise

Physiological noise is a major contaminant of phase regression and needs to be corrected for the technique to be used as a part of high-resolution fMRI research. The

effects of physiological noise vary depending on the subject type and paradigm used as large differences were observed between Chapters 3 and 4. In Chapter 3, the human phase data did not contain a large amount of physiological noise and so BOLD activity was the dominant signal in the phase time courses. The phase data from Chapter 4 contains noise from non-neurovascular sources, the MRI cold heads and respiration, and this noise dominated phase regression. Possible corrections for physiological noise as observed in Chapter 4 are the use of RETROICOR [3] or DORK to perform on-system correction for mass motion field shifts [4]. These methods would need scanner implementation to be useful in the macaques as they both require adaption of system equipment or implementation of navigators. Additionally, a threshold for phase data quality has not been well defined in the phase regression literature and would provide a benchmark for pilot studies attempting phase regression.

5.3   Future Applications of Phase Regression

5.3.1   Phase regression at high resolution

Using phase regression as a tool to reduce macrovasculature in high resolution fMRI shows great advantages in flattening the laminar profile. This can be directly applied to the study of layers and columns. Chapter 3 showed this effect flattened the laminar profile without the CNR reduction present in SE-EPI. The reduction in macrovascular signal across a surface was largest within and near pial vessels on the cortical surface. This means phase regression could be combined with existing correction for penetrating vessel effects to create a signal localized to the vascular bed [12]. These signals with increased specificity could then be used to perform cutting-edge laminar fMRI experiments, such as examining feedback and feedforward information discrimination in the visual cortex. Feedback and feedforward processes are defined by their differing inputs to the upper and deep layers of cortex [13]. These layers are expected to experience different amounts of contamination from the extravascular BOLD signal of the pial vessels thus, reduction of this signal would allow for these processes to be more easily separated and studied.

High resolution fMRI can be performed with many sequences, but one popular sequence is vascular space occupancy (VASO). This technique uses an inversion pulse to null the blood and creates an image proportional to 1-CBV [14]. In this way the neurovascular response can be measured through changes in CBV opposed to the BOLD effect. VASO has been successfully used for laminar fMRI in the motor cortex [15], the visual cortex [16], and studying higher order memory effects [17]. Chapter 3 showed GE-EPI-PR has a CNR of 60% of the GE-EPI signal, similar to VASO [18]. However, due to the required inversion pulse, VASO will be temporally slower than GE-EPI-PR and therefore have less statistical power overall. Additionally, VASO is constrained to a small slab, although this is improving over time [19]. A future direction of this work would be to examine these two techniques side by side to compare their specificity to a layer application and directly compare signal power. VASO may be more suited to high precision task based laminar studies where the temporal constraints can be accommodated while GE-EPI-PR benefits from the higher statistical power to study high resolution dynamic processes such as resting state and movie viewing [20] as well as offering whole-brain coverage.

5.3.2 Phase regression in macaques

Applications of phase regression in macaques will require more research to resolve the issues observed in Chapter 4. In Chapter 4, noise from sources other than the neurovascular response dominated fitting and prevented the use of phase regression as a macrovasculature reduction tool. Future work would benefit from use of an awake animal model performing a task as this would allow for a single brain area to be examined and would provide a strong statistically powerful response to optimize phase regression with. Using a sedated macaque to perform a task experiment has been done in the past [21] but is not as powerful or reliable as an awake animal model [22]. Therefore, most sedated macaque papers examine resting state connectivity which is known to be reduced but not erased by sedation [23]. As stated in Chapter 4, it is harder to interpret changes in resting state connectivity and this is simplified by using a task paradigm. In addition, to prevent non-neurovascular noise from dominating the phase data such animal experiments should

use both physiological tracing and navigator correction to try and obtain the cleanest phase data possible [3,4].

5.3.3   What vessels is phase regression affecting?

An open question in phase regression research is the size of vessels the technique is affecting. The larger a vessel is, the more phase signal it will produce and therefore the more that signal will be reduced. Comparatively, the minimum size threshold for phase regression is less defined as it will be dependent on both SNR and vessel orientations. The organization of the cortical vasculature makes this an exciting research question. For example, the penetrating veins, small vessels that run perpendicular to the cortical surface, are all oriented the same direction and could potentially sum to create a phase response. Additionally, pial vessels have been observed to dominate GE-EPI at ultra-high field through extravascular signal [24] and it is unclear if phase regression fully reduces this extravascular effect. One experiment that could tease these factors apart is using cortical orientation to examine whether these penetrating veins are being affected or if the extravascular BOLD response is fully removed.

The orientation of the cortical sheet allows for interrogation of signal origin due to the regularity of its structure. The cortex is made up of three venous populations, pial vessels which run along the surface of cortex perpendicular to the cortical surface normal, penetrating vessels which dive into the cortical sheet and run parallel to the cortical surface normal and capillaries and venules inside the cortical sheet which run at arbitrary orientations to form the microvascular support structures for the neurons of the cortex [25]. Previous investigations of GE-EPI have shown that the GE-EPI BOLD signal has a cortical orientation dependence maximum at 0° to B_0, and a minimum at 90° [26]. This is equivalent to a large extravascular signal running perpendicular to the cortical sheet, such as the pial vessels. Expanding on this work, cortical orientation has been used to measure pial vessel signal dominance in various cases with different sequence types and sequence parameters [27]. Such a cortical orientation investigation could be paired with phase regression to determine what effect this method has on pial vessel signal reduction and if phase regression effects the penetrating vessels. First, if phase regression will reduce signal from pial vasculature but, due to their size, does not affect the penetrating vessels

the orientation curve will reverse and have a maximum at 90°, as these penetrating vessels run parallel to the cortical surface normal. If the opposite is observed and the orientation curve is flat, this would indicate that the signal is now driven by capillaries and not any of the draining microvasculature. Finally, if the orientation dependence is reduced but remains the same direction then the pial vessel extravascular signal is not being fully reduced. In this way orientation dependence could be a powerful tool to determine the vascular origin of the GE-EPI-PR BOLD signal.

As a preliminary analysis, data from Chapter 3 was used. Each vertex on the cortical surface was assigned an orientation using the surface normal and the Freesurfer tool, *mris_convert* [28]. The BOLD response was then plotted against the cortical orientation and is shown in Figure 5.1. GE-EPI shows the expected orientation dependence at all three depths. SE-EPI shows a reduced orientation dependence compared to GE-EPI but still shows the expected maximum at 0° and reduction towards 90°. This is because SE-EPI reduces some venous bias but is still sensitive to large vessels, depending on pulse sequence parameters [29]. GE-EPI-PR shows no orientation dependence at the higher cortical depths, an increase in the middle of cortex, and a decrease near the white matter boundary. These results are preliminary but the reduced orientation dependence at the pial surface supports the hypothesis that phase regression is reducing signal from pial vessels. In a future experiment this could be fit to the expected responses to determine the vascular origin of the measured BOLD signal. This would help to understand the vessel size floor for phase regression to perform macrovascular signal reduction.
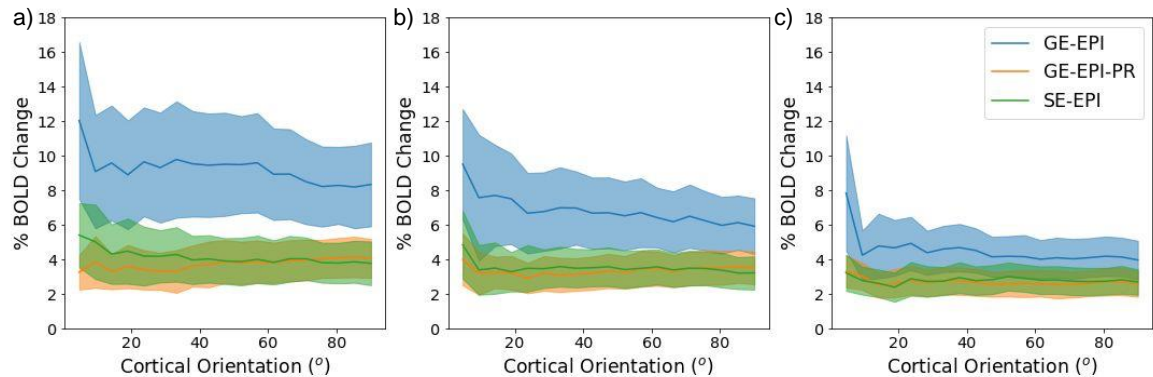
Figure 5.1: Percent BOLD change as a function of cortical orientation. Data from Chapter 3, humans with a visual checkerboard task. a) 10% cortical depth, b) 50% cortical depth, and c) 90% cortical depth.

5.4   Conclusions

This work expands on the existing research into phase regression with the goal of implementing and investigating the technique at high resolution. This was done three ways: 1) by creating a combination method targeted at combining high resolution phase data, 2) investigating phase regression using human subjects and a visual task at high resolution, and 3) continuing this investigation by piloting phase regression in macaques during resting state. This thesis concludes that phase regression may require additional cleaning and finessing, to remove non-neurovascular sources of phase noise. Once clean phase data is achieved, the phase regression method does lead to a flatter laminar profile with a higher contrast-to-noise ratio than SE-EPI and this poses immediate advantages to its inclusion as part of laminar and columnar fMRI in humans.

5.5   References

1. Walsh DO, Gmitro AF, Marcellin MW. Adaptive reconstruction of phased array MR imagery. Magn Reson Med. 2000;43: 682–690. doi:10.1002/(SICI)1522-2594(200005)43:5<682::AID-MRM10>3.0.CO;2-G

2. Hagberg GE, Bianciardi M, Brainovich V, Cassara AM, Maraviglia B. Phase stability in fMRI time series: effect of noise regression, off-resonance correction and spatial filtering techniques. NeuroImage. 2012;59: 3748–3761. doi:10.1016/j.neuroimage.2011.10.095

3. Glover GH, Li TQ, Ress D. Image-based method for retrospective correction of physiological motion effects in fMRI: RETROICOR. Magn Reson Med. 2000;44: 162–167. doi:10.1002/1522-2594(200007)44:1<162::aid-mrm23>3.0.co;2-e

4. Pfeuffer J, Van de Moortele P-F, Ugurbil K, Hu X, Glover GH. Correction of physiologically induced global off-resonance effects in dynamic echo-planar and spiral functional imaging. Magn Reson Med. 2002;47: 344–353. doi:10.1002/mrm.10065

5. Sbrizzi A, Hoogduin H, Lagendijk JJ, Luijten P, van den Berg CAT. Robust reconstruction of B1 (+) maps by projection into a spherical functions space. Magn Reson Med. 2014;71: 394–401. doi:10.1002/mrm.24640

6. Katscher U, Berg CAT van den. Electric properties tomography: Biochemical, physical and technical background, evaluation and clinical applications. NMR Biomed. 2017;30: e3729. doi:10.1002/nbm.3729

7. Eckstein K, Dymerska B, Bachrata B, Bogner W, Poljanc K, Trattnig S, et al. Computationally Efficient Combination of Multi-channel Phase Data From Multi-echo Acquisitions (ASPIRE). Magn Reson Med. 2018;79: 2996–3006. doi:10.1002/mrm.26963

8. Robinson SD, Dymerska B, Bogner W, Barth M, Zaric O, Goluch S, et al. Combining phase images from array coils using a short echo time reference scan (COMPOSER). Magn Reson Med. 2017;77: 318–327. doi:10.1002/mrm.26093

9. Poser BA, Setsompop K. Pulse sequences and parallel imaging for high spatiotemporal resolution MRI at ultra-high field. NeuroImage. 2018;168: 101–118. doi:10.1016/j.neuroimage.2017.04.006

10. Feinberg DA, Hale JD, Watts JC, Kaufman L, Mark A. Halving MR imaging time by conjugation: demonstration at 3.5 kG. Radiology. 1986;161: 527–531. doi:10.1148/radiology.161.2.3763926

11. Noll DC, Nishimura DG, Macovski A. Homodyne detection in magnetic resonance imaging. IEEE Trans Med Imaging. 1991;10: 154–163. doi:10.1109/42.79473

12. Markuerkiaga I, Barth M, Norris DG. A cortical vascular model for examining the specificity of the laminar BOLD signal. NeuroImage. 2016;132: 491–498. doi:10.1016/j.neuroimage.2016.02.073

13. Self MW, van Kerkoerle T, Goebel R, Roelfsema PR. Benchmarking laminar fMRI: Neuronal spiking and synaptic activity during top-down and bottom-up processing in the different layers of cortex. NeuroImage. 2019;197: 806–817. doi:10.1016/j.neuroimage.2017.06.045

14. Lu H, van Zijl P. A review of the development of Vascular-Space-Occupancy (VASO) fMRI. Neuroimage. 2012;62: 736–742. doi:10.1016/j.neuroimage.2012.01.013

15. Huber L, Handwerker DA, Jangraw DC, Chen G, Hall A, Stüber C, et al. High-Resolution CBV-fMRI Allows Mapping of Laminar Activity and Connectivity of Cortical Input and Output in Human M1. Neuron. 2017;96: 1253-1263.e7. doi:10.1016/j.neuron.2017.11.005

16. Akbari A, Bollmann S, Ali TS, Barth M. Modelling the depth-dependent VASO and BOLD responses in human primary visual cortex. bioRxiv. 2021; 2021.05.07.443052. doi:10.1101/2021.05.07.443052

17. Finn ES, Huber L, Bandettini PA. Higher and deeper: Bringing layer fMRI to association cortex. Prog Neurobiol. 2020; 101930. doi:10.1016/j.pneurobio.2020.101930

18. Huber L, Goense J, Kennerley AJ, Trampel R, Guidi M, Reimer E, et al. Cortical lamina-dependent blood volume changes in human brain at 7T. NeuroImage. 2015;107: 23–33. doi:10.1016/j.neuroimage.2014.11.046

19. Laurentius Huber, Yuhui Chai, Rüdiger Stirnberg, Sriranga Kashyap, Deni Kurban, Arman Khojandi, et al. Beyond the limits of layer-dependent CBV fMRI in humans: strategies towards whole brain coverage, sub-second TR, and very high 0.5mm resolutions. Proceedings of the 29th International Society for Magnetic Resonance in Medicine Annual Meeting. 2020.

20. Meer JN van der, Breakspear M, Chang LJ, Sonkusare S, Cocchi L. Movie viewing elicits rich and reliable brain state dynamics. Nat Commun. 2020;11: 5004. doi:10.1038/s41467-020-18717-w

21. Rainer G, Augath M, Trinath T, Logothetis NK. The effect of image scrambling on visual cortical BOLD activity in the anesthetized monkey. NeuroImage. 2002;16: 607–616. doi:10.1006/nimg.2002.1086

22. Goense JBM, Ku S-P, Merkle H, Tolias AS, Logothetis NK. fMRI of the temporal lobe of the awake monkey at 7 T. NeuroImage. 2008;39: 1081–1093. doi:10.1016/j.neuroimage.2007.09.038

23. Hutchison RM, Hutchison M, Manning KY, Menon RS, Everling S. Isoflurane induces dose-dependent alterations in the cortical connectivity profiles and dynamic properties of the brain's functional architecture. Hum Brain Mapp. 2014;35: 5754–5775. doi:10.1002/hbm.22583

24. Bause J, Polimeni JR, Stelzer J, In M-H, Ehses P, Kraemer-Fernandez P, et al. Impact of prospective motion correction, distortion correction methods and large vein bias on the spatial accuracy of cortical laminar fMRI at 9.4 Tesla. NeuroImage. 2020;208: 116434. doi:10.1016/j.neuroimage.2019.116434

25. Duvernoy HM, Delon S, Vannson JL. Cortical blood vessels of the human brain. Brain Res Bull. 1981;7: 519–579. doi:10.1016/0361-9230(81)90007-1

26. Viessmann O, Scheffler K, Bianciardi M, Wald LL, Polimeni JR. Dependence of resting-state fMRI fluctuation amplitudes on cerebral cortical orientation relative to the direction of B0 and anatomical axes. NeuroImage. 2019;196: 337–350. doi:10.1016/j.neuroimage.2019.04.036

27. Báez-Yánez MG, Ehses P, Mirkes C, Tsai PS, Kleinfeld D, Scheffler K. The impact of vessel size, orientation and intravascular contribution on the neurovascular fingerprint of BOLD bSSFP fMRI. NeuroImage. 2017;163: 13–23. doi:10.1016/j.neuroimage.2017.09.015

28. Fischl B, Sereno MI, Dale AM. Cortical surface-based analysis. II: Inflation, flattening, and a surface-based coordinate system. NeuroImage. 1999;9: 195–207. doi:10.1006/nimg.1998.0396

29. Goense JBM, Logothetis NK. Laminar specificity in monkey V1 using high-resolution SE-fMRI. Magn Reson Imaging. 2006;24: 381–392. doi:10.1016/j.mri.2005.12.032

Appendices

Appendix 1: Human Ethics Approval - Chapters 2 and 3

Western Research

Date: 26 February 2021

To: Ravi Menon

Project ID: 108810

Study Title: High Resolution Functional Magnetic Resonance Imaging of Columnar and Laminar Structures in the Human Cortex

Application Type: Continuing Ethics Review (CER) Form

Review Type: Delegated

REB Meeting Date: 09/March/2021

Date Approval Issued: 26/Feb/2021

REB Approval Expiry Date: 01/Mar/2022

Dear Ravi Menon,

The Western University Research Ethics Board has reviewed the application. This study, including all currently approved documents, has been re-approved until the expiry date noted above.

REB members involved in the research project do not participate in the review, discussion or decision.

Western University REB operates in compliance with, and is constituted in accordance with, the requirements of the Tri-Council Policy Statement: Ethical Conduct for Research Involving Humans (TCPS 2); the International Conference on Harmonisation Good Clinical Practice Consolidated Guideline (ICH GCP); Part C, Division 5 of the Food and Drug Regulations; Part 4 of the Natural Health Products Regulations; Part 3 of the Medical Devices Regulations and the provisions of the Ontario Personal Health Information Protection Act (PHIPA 2004) and its applicable regulations. The REB is registered with the U.S. Department of Health & Human Services under the IRB registration number IRB 00000940.

Please do not hesitate to contact us if you have any questions.

Sincerely,

The Office of Human Research Ethics

Note: This correspondence includes an electronic signature (validation and approval via an online system that is compliant with all regulations).

Western

2015-084:7:

AUP Number: 2015-084
AUP Title: Shedding the Light on BOLD: understanding the how of "working" brain maps in NHPs
Yearly Renewal Date: 02/01/2020

The YEARLY RENEWAL to Animal Use Protocol (AUP) 2015-084 has been approved by the Animal Care Committee (ACC),
and will be approved through to the above review date.

 Please at this time review your AUP with your research team to ensure full understanding by everyone listed within this AUP.

As per your declaration within this approved AUP, you are obligated to ensure that:

      1) Animals used in this research project will be cared for in alignment with:
                a) Western's Senate MAPPs 7.12, 7.10, and 7.15
                 http://www.uwo.ca/univsec/policies_procedures/research.html
                b) University Council on Animal Care Policies and related Animal Care Committee procedures
                 http://uwo.ca/research/services/animalethics/animal_care_and_ use_policies.html
      2) As per UCAC's Animal Use Protocols Policy,
                a) this AUP accurately represents intended animal use;
                b) external approvals associated with this AUP, including permits and scientific/departmental peer approvals, are complete and accurate;
                c) any divergence from this AUP will not be undertaken until the related Protocol Modification is approved by the ACC; and
                d) AUP form submissions - Annual Protocol Renewals and Full AUP Renewals - will be submitted
                and attended to within timeframes outlined by the
ACC.   http://uwo.ca/research/services/animalethics/animal_use_protocols.html
      3) As per MAPP 7.10 all individuals listed within this AUP as having any hands-on animal contact will
                a) be made familiar with and have direct access to this AUP;
                b) complete all required CCAC mandatory training
([%20%20training@uwo.ca] training@uwo.ca); and
                c) be overseen by me to ensure appropriate care and use of animals.
      4) As per MAPP 7.15,
                a) Practice will align with approved AUP elements;
                b) Unrestricted access to all animal areas will be given to ACVS Veterinarians and ACC Leaders;

Appendix 3: Copyright of Chapter 3

Dear Dr. Stanley,

Yes, please include it as it is an open access.

Kind regards,

Nathiya Sellamuthu
Journal Manager
ELSEVIER | Operations | Research Content Operations

Curriculum Vitae

Name: Olivia Stanley

Post-secondary Education and Degrees:

University of Waterloo
Waterloo, Ontario, Canada
2010-2015 B.Sc.

The University of Western Ontario
London, Ontario, Canada
2015-2021 Ph.D.

Honours and Awards:

NSERC Undergraduate Research Award
2014

Ontario Graduate Scholarship
2016-2017

International Society for Magnetic Resonance in Medicine Travel Award 2017, 2018

Robarts Association of Trainees Collaborative Research Competition
2018

Canadian Open Neuroscience Student Scholar Award
2019-2020

Society for Neuroscience Trainee Professional Development Award
2020

Publications:

Olivia W Stanley, Ravi S Menon, L Martyn Klassen. (2021). Receiver phase alignment using fitted SVD derived sensitivities from routine prescans. PLoS One.

Olivia W Stanley, Alan B Kuurstra, L Martyn Klassen, Ravi S Menon, Joseph S Gati. (2021). Effects of Phase Regression on High-Resolution Functional MRI of the Primary Visual Cortex. NeuroImage.

Jonathan C. Lau, Andrew G. Parrent, John Demarco, Geetika Gupta, Jason Kai, Olivia W Stanley, Tristan Kuehn, Patrick J. Park, Kayla Ferko, Ali R. Khan, Terry M. Peters. (2019). A framework for evaluating correspondence between brain images using anatomical fiducials. Human Brain Mapping.

Marie-Laurence Tremblay, Christa Davis, Chris Bowen, Olivia W Stanley, Cathryn Parsons, Mohan Karkada, Genevieve Weir, Marianne Stanford, and Kimberly Brewer. (2017). Using MRI Cell Tracking to Monitor Immune Cell Recruitment in Re- sponse to a Peptide-Based Cancer Vaccine. magnetic Resonance in Medicine.

Presentations:

Olivia W Stanley, Alan B Kuurstra, Ravi S Menon. (2019). Phase-based macrovascular filtering from gradient-echo BOLD fMRI reduces orientation dependence. Society for Neuroscience, Chicago, Illinois. Poster.

Olivia W Stanley, Ravi S Menon, L Martyn Klassen. (2019) Using Low Resolution Pre- Scans and Singular Value Decomposition Derived Sensitivities to Allow for the Combination of Large Phase Datasets. Imaging Network of Ontario, London, Ontario. Oral Presentation.

Olivia W Stanley, Ravi S Menon, L Martyn Klassen. (2018). Phase sensitive receiver combination using pre-scan singular value decom- position derived receiver sensitivities. Gordon Research Seminar, Proctor Academy, New Hampshire. Oral Presentation.

Olivia W Stanley, Alan B Kuurstra, L Martyn Klassen, Ravi S Menon, Joseph S Gati. (2018). Comparing cortical layer activation using gradient echo with phase regression and spin echo in the human visual cortex. International Society for Magnetic Resonance in Medicine, Paris, France. Poster.

John Baxter, Zahra Hosseini, Olivia W Stanley, Ravi S Menon, Maria Drangova, Terry Peters. (2018). Optimization-Based Simultaneous Combination and Unwrapping for MR Phase Imaging. International Society for Magnetic Resonance in Medicine, Paris, France. Poster.

Sagar Buch, Olivia W Stanley, L Martyn Klassen, Ravi S Menon. (2018). Quantifying Cerebral Activity during a Visual Stimuli using QSM and Multiband-EPI. International Society for Magnetic Resonance in Medicine, Paris, France. Poster.

Olivia W Stanley, Ravi S Menon, L Martyn Klassen. (2017). Absolute B_1^- estimation without a homogeneous receive coil. International Society for Magnetic Resonance in Medicine, Honolulu, Hawaii. Poster.

Olivia W Stanley, Ravi S Menon, L Martyn Klassen. (2017). Whole time-course coil combination using singular value decomposition. Imaging Network of Ontario, London, Ontario. Poster.

Olivia Stanley, Elizabeth DeGuzman, Brian Nieman. (2014). Environmental Enrichment as a Treatment for Radiation-Induced Brain Damage in Mice. The Sick Kids Summer Research Program, Toronto, Ontario. Poster.